FINAL REPORT

Report Submitted to: **National Energy Technology Laboratory**
U.S. Department of Energy

DOE Award Number: **DE-FE0007405**

Project Title: **Embedded Active Fiber Optic Sensing Network for Structural Health Monitoring in Harsh Environments**

Principal Investigator: **Dr. Anbo Wang**
Clayton Ayre Professor of Electrical Engineering
awang@vt.edu
(540) 231-4363

Report Preparer: **Chennan Hu**
chennan@vt.edu
(540) 808-6822

Report Submission Date: **January 07, 2017**

DUNS Number: **003137015**

Recipient Organization: **Virginia Polytechnic Institute & State University**
Office of Sponsored Programs
Research Building XV
1880 Pratt Drive, Suite 2006
Blacksburg, VA 24060

Project Period: **April 1, 2013 – September 30, 2016**

Report Term: **Final**

Signature of Submitter: **Chennan Hu**

CPT
CENTER FOR PHOTONICS TECHNOLOGY

Disclaimer

Abstract

This report summarizes technical progress on the program "Embedded Active Fiber Optic Sensing Network for Structural Health Monitoring in Harsh Environments" funded by the National Energy Technology Laboratory of the U.S. Department of Energy, and performed by the Center for Photonics Technology at Virginia Tech.

The objective of this project is to develop a first-of-a-kind technology for remote fiber optic generation and detection of acoustic waves for structural health monitoring in harsh environments. During the project period, which is from April 1, 2013 to Septemeber 30, 2016, three different acoustic generation mechanisms were studied in detail for their applications in building a fiber optic acoustic generation unit (AGU), including laser induced plasma breakdown (LIP), Erbium-doped fiber laser absorption, and metal laser absorption. By comparing the performance of the AGUs designed based on these three mechanisms and analyzing the experimental results with simulations, the metal laser absorption method was selected to build a complete fiber optic structure health monitoring (FO-SHM) system for the proposed high temperature multi-parameter structure health monitoring application.

Based on the simulation of elastic wave propagation and fiber Bragg grating acoustic pulse detection, an FO-SHM element together with a completed interrogation system were designed and built. This system was first tested on an aluminum piece in the low-temperature range and successfully demonstrated its capability of multi-parameter monitoring and multi-point sensing. In the later stages of the project, the research was focused on improving the surface attachment design and preparing the FO-SHM element for high temperature environment tests. After several upgrades to the surface attachment methods, the FO-SHM element was able to work reliably up to 600^{o}C when attached to P91 pipes, which are the target material of this project. In the final stage of this project, this FO-SHM sensing system was tested in the simulated harsh environment for its multi-parameter monitoring performance and high-temperature survivability.

Table of Contents

List of Figures and Tables

1 Introduction

The interconnected consequences of the national energy strategy compel us to design energy systems to operate at higher temperatures to achieve greater efficiency from fossil fuel systems with lower greenhouse gas emissions. One example is the Ultra Supercritical (USC) steam cycle design, which raises the operating steam temperature to 760ºC for an efficiency target of 45-47% and a 25-30% reduction in CO_2 emissions [1]. Another is the Integrated Gasification Combined Cycle (IGCC) by which coal can be chemically broken down into syngas products at temperatures well above 1000ºC [2]. The gaseous and solid products of the IGCC process exhibit minimal waste of coal while minimizing carbon emission. Such progressive energy systems, which operate at temperatures much higher than traditional fossil fuel power plants, present a new set of extreme physical and chemical conditions such as ultra-high temperatures, high pressure, and severe chemical corrosion. Materials directly exposed to these harsher environments tend to suffer significant physical or chemical degradation. It is thus indispensable to monitor the health condition of key materials and structures involved in these systems in real time to ensure safety and minimize system shutdowns [3].

Currently available means of assessing material or structural health include on-site assessment methods such as X-ray defect detection [4] and ultrasonic tomography [5], and remote techniques which commonly use piezoelectric transducers. The first methods are reliable and accurate but require on-site access which is often prohibited due to the harsh environments involved in the energy systems. The remote techniques have been effective for structural health monitoring and are often applied to civil structures, however, they are generally restricted to applications at temperatures below 500ºC [6, 7]. Although high temperature piezoelectric transducers have been actively investigated for more than a decade, their reliability at high temperatures still remains a major concern [7-9]. In addition, like other electrical sensors, they are susceptible to electromagnetic interference (EMI). Their signal can also be transmitted through wireless modules, but on-site electric power is required which often presents additional maintenance issues. Given this situation, it is therefore imperative to develop new techniques which allow on-site maintenance-free monitoring of the health conditions of the critical materials and structures that are used in high temperature applications and other harsh environments.

In this project, we developed a new Fiber Optics Structure Health Monitoring (FO-SHM) technology for multi-parameter measurement by realizing fiber optic generation and detection of acoustic waves. A single FO-SHM element is constructed with a pair of in-fiber acoustic generation/detection units, which have a low physical profile (less than 300 um in width). The FO-SHM element is surface attached to the material under monitoring, imposing a minimal intrusion on the integrity of the structure. The detected acoustic signature and the returned optical spectrum allow extraction of information about material's condition including temperature, strain, corrosion, and defects, such as cracks and delamination, which can challenge the structure integrity. In addition, the FO-SHM element can be operated at temperatures well above 800ºC if not mounted and up to 600ºC in the current surface attachment scheme. This technology is also able to monitor multiple locations with serially connected FO-SHM elements and a single interrogation system for long span structure monitoring.

2 Research workflow

In the traditional ultrasonic non-destructive evaluation field, generally, each monitoring system is designed differently based on the type of structures it monitors, which guarantees optimized sensitivity of the parameters at interests. In this project, the goal is to replace the PZT based acoustic generation/detection with fiber optics while still utilize similar ultrasonic NDE sensing principles. Although we expect the fiber optics based NDE system to be more versatile than a traditional PZT based system due to the broader bandwidth and small physical size of the components, we still need to determine the target structure types so the design of the sensing element/system can be more efficient. Therefore the first step of the research in this project is to identify the potential application for such a system. After research and discussion with DOE, the target material was set to be P-91 pipes formed by T91, a widely used alloy in the power industry such as the steam channel in the superheater of a modern large capacity boiler. These pipes normally work in high temperature environment (570 °C to 600 °C) [10, 11]and are used to transmit high pressure (290 bars) [10] and corrosive chemicals inside.

Based on the general shape and dimension of the P-91 pipes, a preliminary FO-SHM element design was presented and the single pulse based ultrasonic method was chosen as the primary method for multi-parameter detection. Several simulations of acoustic generation/propagation were conducted on two-dimensional models to validate this preliminary design. To predict the response of the fiber Bragg grating (FBG) to short acoustic pulse, another simulation was also conducted using the transfer matrix method.

After the preliminary design of a multi-parameter FO-SHM sensing schematic was validated through simulations, several optoacoustic generation mechanisms were studied for their usages in the FO-SHM sensing element. Three mechanisms were tested, which are the laser induced plasma (LIP) process, EDF laser absorption + thermal expansion process, laser scattering + thermal expansion process. In these three methods, the LIP method was found to generate the strongest acoustic vibration. However, further tests indicated that in-fiber LIP based acoustic generation structure was not robust. The EDF-based structure was the simplest among the three, and only required one optical fiber instead of two. However, the generated acoustic vibration was weak due to the material properties of the EDF fiber. The laser scattering process was chosen to be used for the FO-SHM element. This process generated sufficiently strong acoustic vibration for a good signal to noise ratio and showed good long-term stability.

A detailed FO-SHM element design was then carried out and several demonstration samples were fabricated. To demonstrate the multi-parameter monitoring capability, aluminum sheets were used as the monitored material in this phase. The sensing system was also designed and built in this phase, which included the high power laser to fiber coupling system, the interrogation system and the controlling software. The capabilities of the system were demonstrated in the low-temperature range, including the multi-parameter monitoring and the system multiplexing.

The next phase was to prepare the FO-SHM element for the final demonstration in high temperature environment, which included the improvement of the surface embedment schematic and designing the final test apparatus. Several preliminary high temperature tests were conducted to verify the performance and survivability of the FO-SHM element in high temperature environment. The surface embedment schematic was modified several times based on these preliminary high temperature test results and simulations, towards increasing the high temperature survivability.

The system final demonstration was then conducted on P-91 samples with the simulated harsh environment in the lab. The tested temperature range was from room temperature to 600ºC. The corrosion was generated by chemical etching. The crack was simulated by cutting a thin slot on the P-91 tube. The strain was applied on the sample by a mechanical vice and monitored by a strain gauge. Three serially connected FO-SHM elements were used in the demonstration to monitor three different P-91 pipes.

3 Identifying the structure health monitoring target material

P91 is the standard name for pipes made from T91 grade steel and it is widely used in the power industry. We believe this is also the reason that DOE requested the final demonstration of this project be performed on this material. According to our market search, the sizes of these pipes used in the power industry are diverse in terms of diameter but the wall thickness is usually around or less than an inch. Because it is difficult to conduct experiment on pipes with very large diameter in our lab, we decided to use small diameter pipes for our experiment and demonstration. To be able to generate more versatile results, pipes with different wall thickness were purchased for their potential usage in this project. The pipes we acquired and stored in our lab is shown in Figure 3-1. The wall thickness range is from 1/4 inch to 1/2 inch.

These pipes were used throughout the research process and in the final demonstration to test and demonstrate the capability of the developed FO-SHM system. However, the usage of the FO-SHM system developed in this project is not necessarily limited to these pipes. It can be directly used on other shapes/materials, or be deployed with modifications if needed.

Figure 3-1 P91 pipes purchased for the FO-SHM system demonstration

4 Simulation of the ultrasonic pulse based multi-parameter monitoring scheme

In the first phase of this project, we conducted simulations to study how the acoustic signature (AE) responds to parameter changes including the appearance of a crack and thickness change. In these simulations, the generated acoustic pulses were assumed to be much shorter than the thickness of the materials under test, which is a reasonable assumption based on the size of the P-91 pipes and the short laser pulse width we intended to use (50ns). When the acoustic wavelength is much smaller than the thickness of the material, the propagation of the acoustic wave inside the material can generally be treated as body wave propagation. This was also what we have observed in this set of simulations. Due to the complexity of the simulated phenomenon, only two-dimensional models were studied to allow a reasonable simulation time (from 2 hours to a day). In these two-dimensional models, a rectangular area was used to represent nearby cross-section where the FO-SHM element is attached to a P-91 pipe. The height of the rectangular represented the wall thickness of the P-91 pipe and the length of the rectangular area was set long enough so that the side reflection doesn't affect the acoustic signatures at interests.

4.1 FEM simulation of pressure wave propagation

The ultrasonic wave propagations in a solid like the T-91 can be accurately described by the elastic wave propagation model, which includes different elastic wave modes such as longitudinal mode, transverse mode, Rayleigh mode, etc. To get sufficient experience and knowledge to build an accurate mode with elastic wave model, a simpler model was built first with the Pressure Acoustic, Transient module in COMSOL. In this mode, only the longitudinal mode will be presented. The governing equation for the pressure wave is[12]:

$$\frac{1}{\rho c^2}\frac{\partial^2 p_t}{\partial t^2}+\nabla\cdot-\frac{1}{\rho}(\nabla p_t-\vec{q})=Q \qquad (1)$$

To simplify the explanation below, the unit of all dimensions is set to mm and it will not be shown. As shown in Figure 4-1, the geometry is a rectangular box centered in (0, 0) and has a dimension of (80, 20). The crack dimension is (2, 0.01), and it is located at different places with different Y values, but the X value is always 0 during the simulation. The acoustic source is located around the point at the upper left of the specimen. The excitation pulse is a cylindrical wave and has a Gaussian shape in time domain, the pulse width is about 100ns which is around the real value we used in experiments. The shape of the pulse is shown in Figure 4-2.

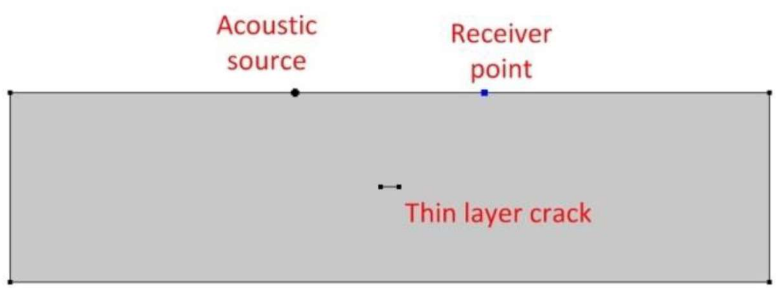

Figure 4-1 Two-dimensional model for crack monitoring

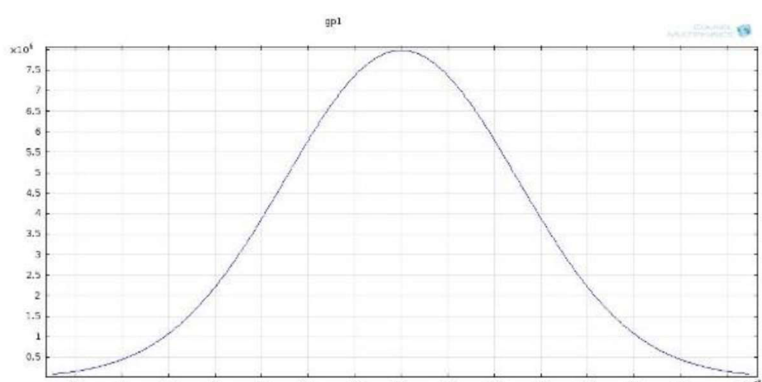

Figure 4-2 Excitation pulse

Because the pulse width is about 100ns, which yields an acoustic wavelength around 0.5mm when the speed of pressure wave is set to 5000m/s, the max mesh size in this model is set to 0.4mm and the time step is set to 10ns. As for boundary conditions in this simulation, there are two kinds of boundary conditions used, cylindrical radiation BC and sound hard BC. First, for better simulating the crack detection in a steel tube, the reflection from the left wall and right wall should be eliminated in this simulation. A cylindrical radiation boundary condition is applied on the left and right walls to achieve this goal. The reflection is significantly reduced but can't be perfectly eliminated because of the multi-reflection from the bottom of the specimen. This reduces the SNR of the final result, but is acceptable for this phase of simulation. For all other boundaries, a sound hard boundary condition is used to generate reflections.

During this simulation, the comparison of received signals at the situations with and without a crack will be performed. And with the crack in the specimen, Y positions of the crack will sweep through (0, -2, -4, -6, -8), and we will use a method we recently discovered to locate the depth of the crack in this situation.

4.1.1 Crack recognition

When there is no crack inside the specimen, the receiver will see the first pulse which comes directly from the source and other multiple reflected pulses between the top wall and bottom wall of the specimen. The result is shown in Figure 4-3.

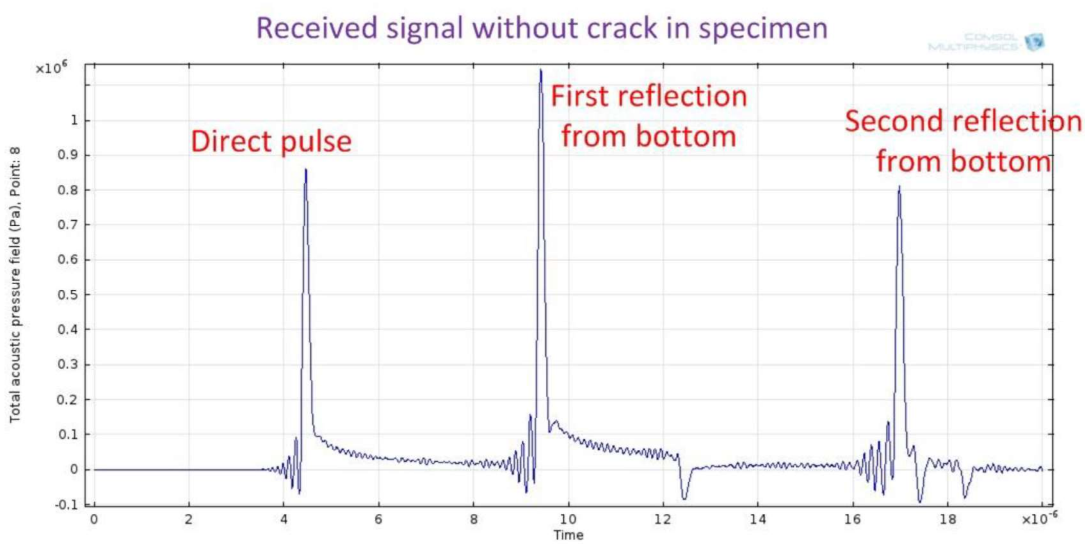

Figure 4-3 Received signal without crack in specimen

When a crack is placed into the specimen, the received signal will also see echoes generated by the crack when the main pulse hit it. Since the main pulse is reflected in the specimen for multiple times, there will be multiple echoes from the crack. However, we will only use the first two echoes since other higher order echoes will be much weaker. The signal with the crack is shown in Figure 4-4.

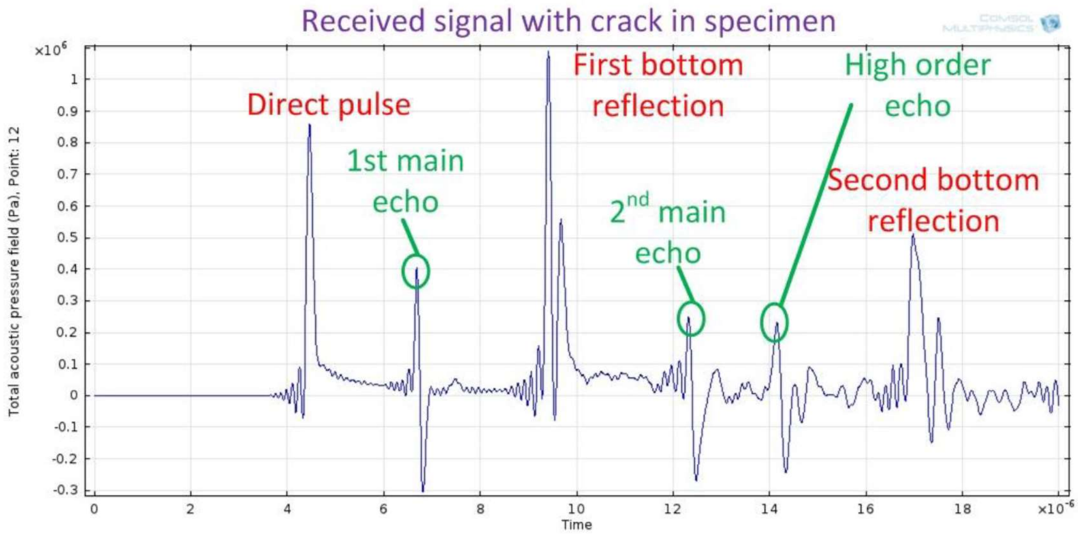

Figure 4-4 Received signal with crack in specimen

The following two figures (Figure 4-5 and Figure 4-6) illustrate the moments when the 1st main echo and the 2nd main echo is generated.

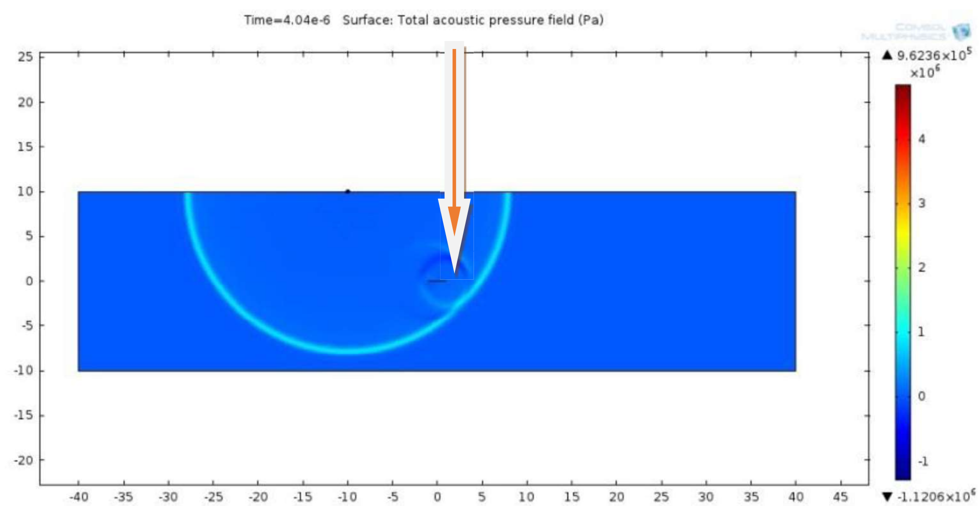

Figure 4-5 First main echo generated

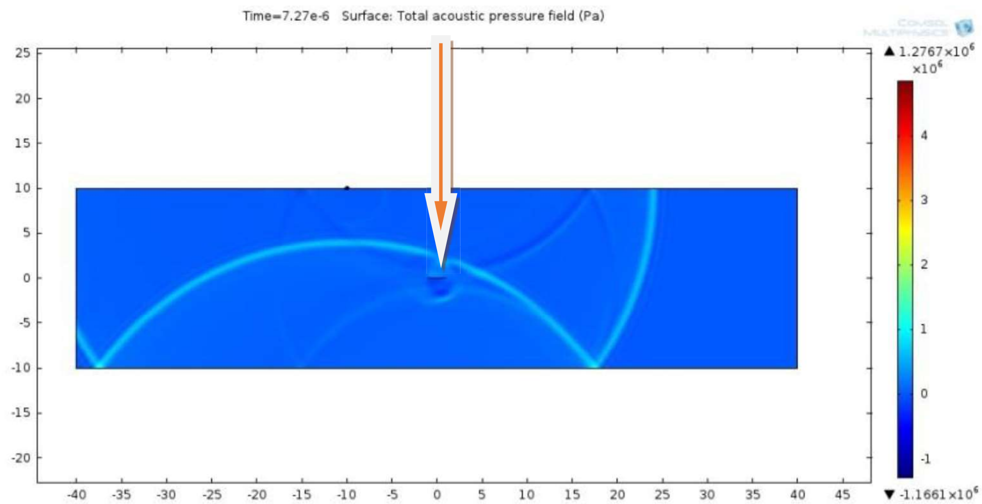

Figure 4-6 Second main echo generated

And here as a conclusion of successful recognition of crack, a combination of all signals for crack at Y= (0, -2, -4, -6, -8) and no crack is shown in Figure 4-7. And the trend for the echo positions moving with crack positions is very clear.

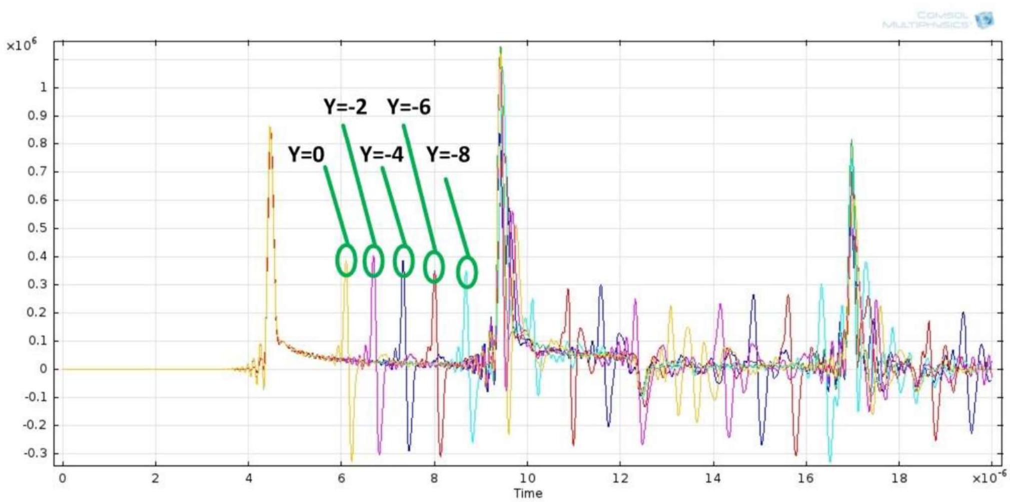

Figure 4-7 without crack, with crack Y=(0, -2, -4, -6, -8)

4.1.2 Corrosion detection (thickness change)

In the traditional ultrasonic NDE applications, the corrosion of a sample is generally monitored by measuring the thickness change of the sample. To predict the thickness change of a sample with this two-dimensional model, a simple situation is studied in this section, where there is no crack formed inside the material yet. In this simulation, the plate is set to 0.5mm thinner than in the previous section, which makes the total thickness 19.5mm. And the comparison between these two conditions is presented in Figure 4-8. Using cross-correlation on the data from 8us~10us (shaded area in Figure 4-8), the lag between these two sets of signal is 0.18us.

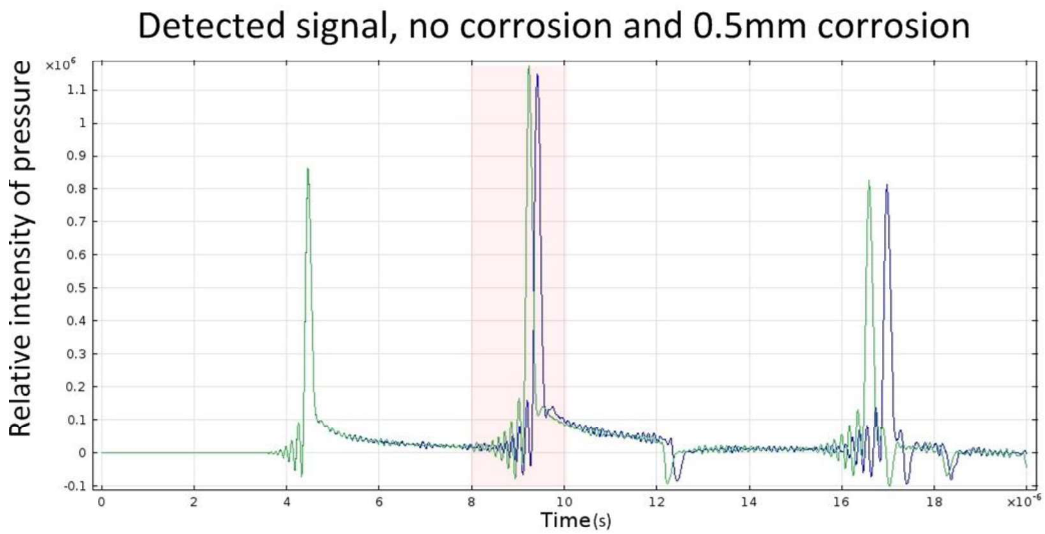

Figure 4-8 Comparison of received signal, no corrosion and 0.5mm corrosion

As shown in Figure 4-9, we know that the angle θ can be calculated by:

$$\theta = \arctan(\frac{a/2}{d}) = 14.04° \qquad (2)$$

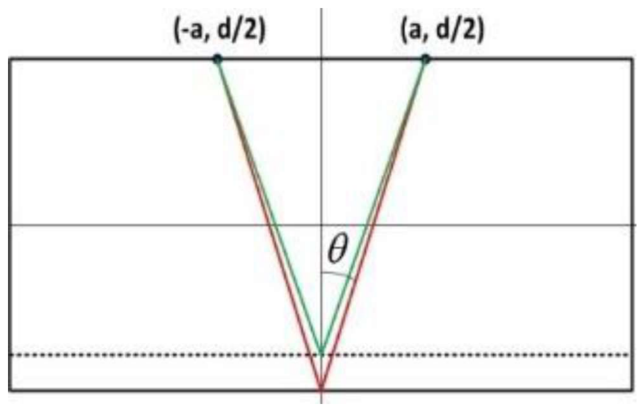

Figure 4-9 Reflection path change when corrosion happens

So the thickness of the corrosion is calculated by:

$$\begin{aligned} t &= \frac{lag \times v \times \cos(\theta)}{2} \\ &= \frac{0.18us \times 5000m/s \times \cos(14.04°)}{2} \\ &= 0.44mm \end{aligned} \qquad (3)$$

According to this simulation, we can see that the quantification of the depth of corrosion could be accurate down to 0.1mm range in an ideal situation, where no crack is presented in the work piece and corrosion cover entire surface uniformly.

4.2 FEM simulation of crack and corrosion detection using the elastic wave model

In the previous section, a simulation of crack and corrosion detection using a pressure wave propagation model was demonstrated. The appearance of a crack and corrosion can be monitored by observing the evolution of the acoustic signature. Although it provides sufficient information for understanding the behavior of the pressure waves, it is not accurate enough to predict and analyze results in the experiments. By using a more complicated elastic wave propagation acoustic model, it is able to acquire more realistic results from simulation, which will be more helpful in the element design optimization and AE analysis. In this section, we present the modelling of crack and corrosion detection based on linear elastodynamic wave propagation in uniform and isotropic material.

4.2.1 Principle of elastic wave propagation in solids

Linear elastodynamic wave theory describes the propagation of elastic waves inside linear solid materials. Among all the parameters associated with an elastic wave, time variant strain is what we could detect experimentally in the crack and corrosion detection. The governing equations are shown as follows (in direct tensor form)[13]:

Equation of motion: $$\nabla\cdot\boldsymbol{\sigma} + \mathbf{F} = \rho\ddot{\mathbf{u}} \tag{4}$$

Strain-displacement equations: $$\boldsymbol{\varepsilon} = \tfrac{1}{2}\left[\nabla\mathbf{u} + (\nabla\mathbf{u})^T\right] \tag{5}$$

Constitutive equations: $$\boldsymbol{\sigma} = \mathsf{C} : \boldsymbol{\varepsilon} \tag{6}$$

Here **σ** is the Cauchy stress tensor, **ε** is the infinitesimal strain tensor, **u** is the displacement vector, C is the fourth-order stiffness tensor, **F** is the body force per unit volume, and ρ is the mass density of the material.

By solving these equations with a finite element method, the time variant strain at any given point in the material can be given as:

$$\varepsilon = \begin{bmatrix} \varepsilon_{xx} & \varepsilon_{xy} & \varepsilon_{xz} \\ \varepsilon_{yx} & \varepsilon_{yy} & \varepsilon_{yz} \\ \varepsilon_{zx} & \varepsilon_{zy} & \varepsilon_{zz} \end{bmatrix} = \begin{bmatrix} \dfrac{\partial u_x}{\partial x} & \dfrac{1}{2}\left(\dfrac{\partial u_x}{\partial y} + \dfrac{\partial u_y}{\partial x}\right) & \dfrac{1}{2}\left(\dfrac{\partial u_x}{\partial z} + \dfrac{\partial u_z}{\partial x}\right) \\ \dfrac{1}{2}\left(\dfrac{\partial u_y}{\partial x} + \dfrac{\partial u_x}{\partial y}\right) & \dfrac{\partial u_y}{\partial y} & \dfrac{1}{2}\left(\dfrac{\partial u_y}{\partial z} + \dfrac{\partial u_z}{\partial y}\right) \\ \dfrac{1}{2}\left(\dfrac{\partial u_z}{\partial x} + \dfrac{\partial u_x}{\partial z}\right) & \dfrac{1}{2}\left(\dfrac{\partial u_z}{\partial y} + \dfrac{\partial u_y}{\partial z}\right) & \dfrac{\partial u_z}{\partial z} \end{bmatrix} \tag{7}$$

In a 2D simulation, if the FBG is placed along the x direction, the parameter of interest will be ε_{xx} since it is the only strain component that can be detected by the FBG.

In the elastic wave model, multiple propagation modes are supported due to the existence of shear stress. The bulk waves which propagate inside the material include both a pressure wave (P-wave) and a shear wave (S-wave). They have different propagation speeds and are non-dispersive in uniform, isotropic media. However, the speed of P-wave and S-wave are both dependents of temperature. This property could be used for temperature compensation in a multi-parameter measurement system.

Besides bulk waves, the surface wave is also important for traditional ultrasonic NDE method. Generally, the surface wave is the superposition of P-wave and S-wave which follows the surface curvature in propagation and decays rapidly with increased depth. The surface wave could propagate over longer distance than bulk wave and has relatively high amplitude, so it is often used to monitor discontinuities on and near the surface.

There are also guided waves which depend specifically on the medium geometry. Take a plate waveguide for example, if the thickness of the plate is less than 3-4 times of the acoustic wavelength, bulk waves will not be supported and guided waves (or Lamb waves) will take place.

Another important concept in the elastic wave propagation model is the mode conversion. When certain modes of elastic wave encounter a medium interface, mode conversion will happen and multiple modes will be generated at different angles with different amplitudes, which could greatly increase the demodulation complexity.

4.2.2 Simulation model building in COMSOL

To build the simulation model, optimization of the parameters, including the minimum size of detectable crack and acoustic pulse duration, has been conducted.

The crack formation and propagation was intensely studied in the research field of mechanical structures. According to former reports, cracks start with a small initial size and then grow into larger critical size [14, 15]. The initial size of cracks is generally described by a lognormal distribution, with the mean value and standard deviation of (0.526mm, 0.504mm) [15]. On the other hand, the size of critical cracks highly depends on the geometry of the structure. For the current simulation, a crack size reasonably larger than the initial crack size was chosen.

As for the acoustic pulse duration, shorter acoustic wavelength will suffer from stronger attenuation in material while longer wavelength has lower sensitivity to small features in the material. It is reported that the attenuation of acoustic waves increases severely above 10MHz for steel structures [16, 17]. As a general rule of thumb in ultrasound NDE, the probe acoustic wavelength should be shorter than 2/3 of the flaw size to have a reasonable chance of successful detection. Besides, in our laser acoustic generation scheme, using shorter laser pulse will allow us to acquire higher optical-acoustic conversion efficiency despite the generation mechanism deployed.

Considering all these factors, the cracks were modeled as 5mm*0.1mm air voids inside iron specimens, and the excited acoustic pulses were simulated as Gaussian pulses with 500ns FWHM (~3mm wavelength for P-wave, ~2mm wavelength for S-wave). Other parameters in the simulation are shown as follows:

Table 1 Simulation model properties

Specimen	300mm*100mm rectangular iron

Acoustic excitation area	125µm*1mm rectangular silica
Corrosion thickness	5mm
Distance between acoustic generator and detector	100mm
Fiber attachment	2mm under surface
Crack position	center of specimen

The geometry of the simulation setup is shown in Figure 4-10.

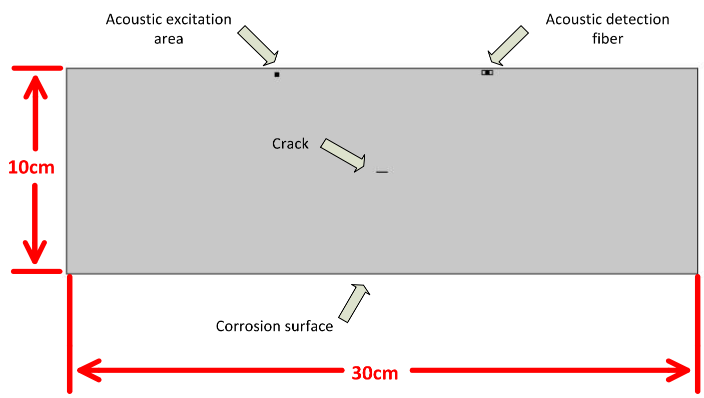

Figure 4-10. Simulation specimen geometry.

4.2.3 Preliminary simulation result

In this preliminary simulation, elastic wave propagation modes are studied and the time variant strain component at the detecting fiber-optic sensor was recorded under different conditions for comparison.

Figure 4-11 shows the elastic wave trace in the specimen. The length of the acoustic pulse is set to be 5mm to suppress multiple reflection near the acoustic source for better visualization. In Figure 4-11(a), P-wave, S-wave, surface wave and crack reflection wave could be clearly observed. The propagation speed of P-wave and S-wave calculated were around 5700m/s and 3100m/s respectively, which agrees well with theoretical values (5770.8m/s and 3138.5m/s). Surface wave speed was calculated to be around 2700m/s, which is slightly slower than S-wave speed as predicted by the elastic wave theory. As the P-wave hits the bottom surface, two reflection waves with different speed were generated from due to mode conversion, which are the faster P-wave and the slower S-wave, as shown in Figure 4-11(b).

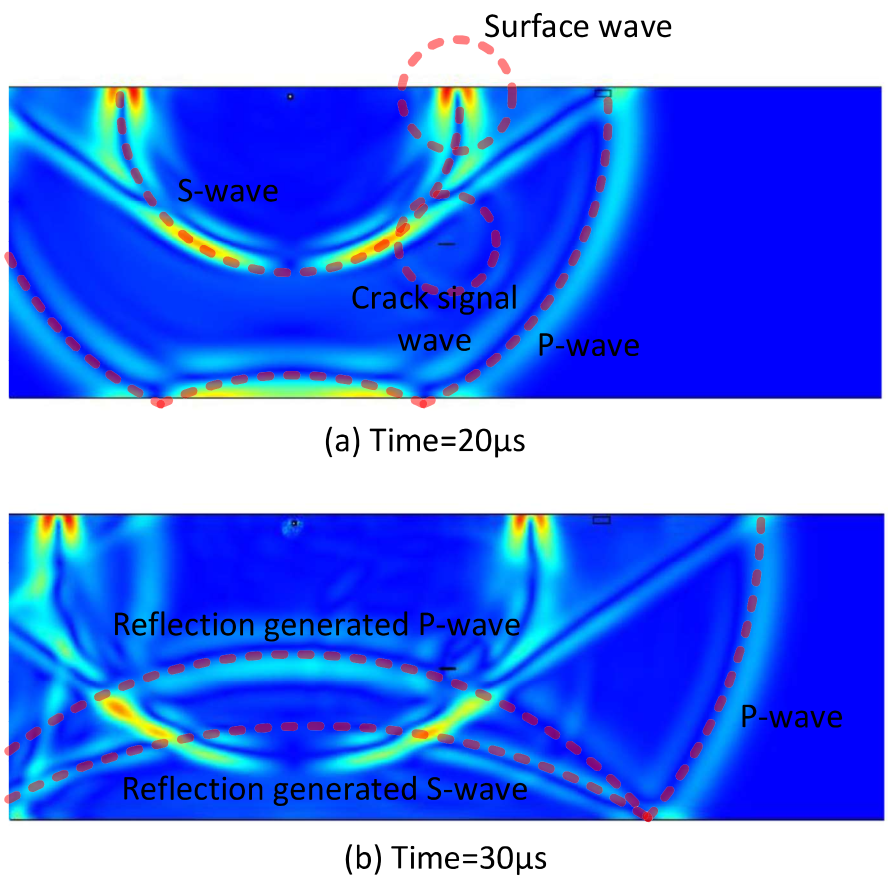

Figure 4-11. Simulation results of elastic wave propagation trace in a specimen with a crack.

The signals induced by the crack were simulated with a 2.5mm acoustic probe pulse, as shown in Figure 4-12. The crack-induced signals were marked in the figures, which could be easily recognized.

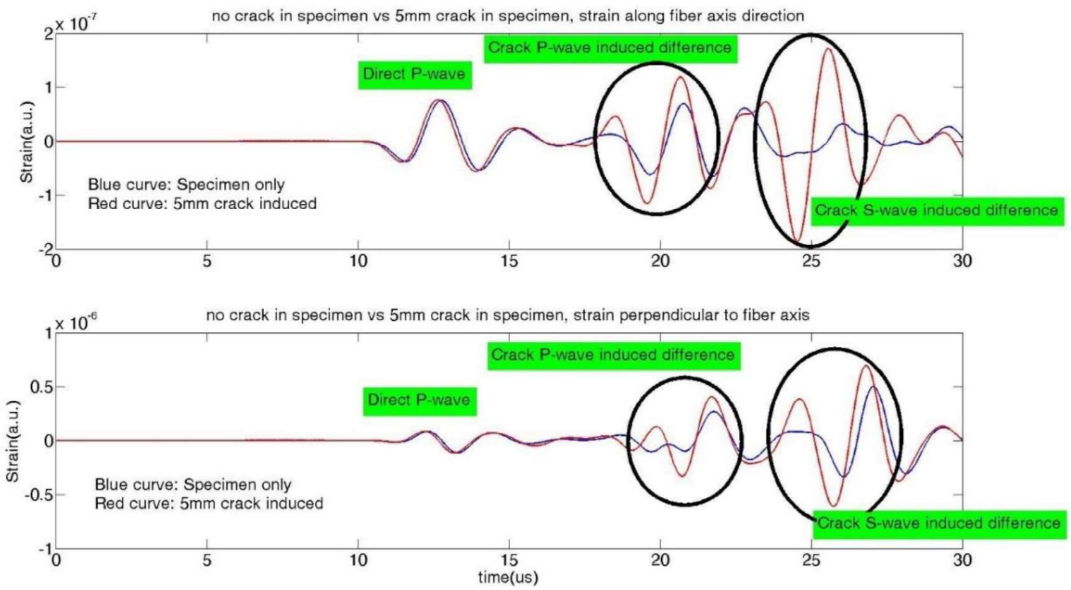

Figure 4-12. Simulation results of crack-induced acoustic signals.

The strain signals in a corroded specimen are also simulated with 2.5mm acoustic pulses. To amplify the signal change induced by the corrosion, a relatively big corrosion depth of 5mm was simulated on the bottom surface. The comparison data is presented in Figure 4-13.

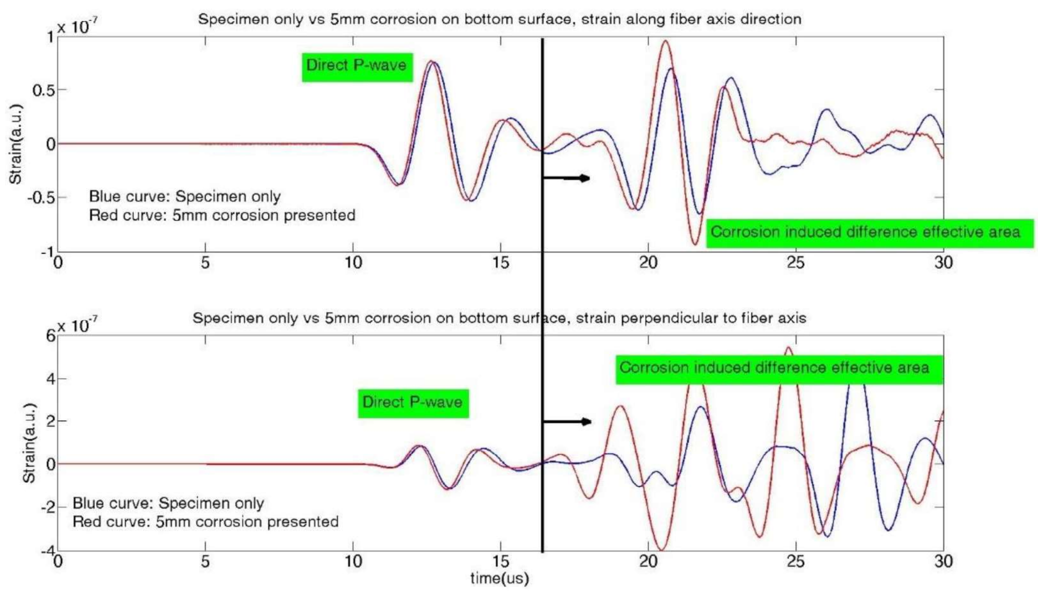

Figure 4-13. Simulation results of corrosion-induced acoustic signals.

The black vertical line in Figure 4-13 marks the boundary between the direct P-wave and echo signals from the bottom surface. Since the direct P-wave should not be affected by the corrosion, the shift observed in the corroded data was attributed to the computational error of the software under different meshing conditions. The phenomenon also presents in the crack simulation data (Figure 4-12).

From this set of simulations, it can be seen that the ultrasonic pulse method can be used to monitor the thickness change and appearance of cracks by the observation of peak shifts and new peak appearances. It is also possible to monitor the temperature change with this method because the thickness change doesn't affect the direct pressure wave. So the location of this peak in the time domain is solely determined by the temperature dependent material properties. The following section shows a calculation of the temperature induced pressure wave velocity change and the corresponding peak delay with a reasonable distance between the acoustic generation/detection pair.

4.3 Temperature induced acoustic velocity change calculation

As indicated in the previous section, the acoustic velocity of the direct pressure wave can be used to monitor the sample temperature. By setting an appropriate gap between the between the acoustic generation unit and the FBG, acoustic velocity can be directly measured by the fly time of the first peak in the AE. The velocity of the longitudinal wave in solids at low temperature is described by the equation:

$$v = \sqrt{\frac{3B+4\mu}{3\rho}} = \sqrt{\frac{E(1-\Upsilon)}{\rho(1-2\Upsilon)(1+\Upsilon)}} \tag{8}$$

where B is the bulk modulus, μ is the shear modulus, E is the Young's modulus, Υ is the Poisson's ratio and ρ is the density if the material. While the theoretical temperature dependence of these elastic constants varies on different materials, some empirical equations can be used on steel to get an estimation of the relationship between fly time variances and temperature changes. These equations are suggested by two scientific organizations (D.T.U. and Eurocode) and adopted in most works that approach the thermal-mechanical analysis of steel structures [18, 19].

For Young's modulus:

$$\begin{aligned} \frac{E(t)}{E(20)} &= 1 + \frac{1}{2000\ln(\frac{t}{1100})} , \quad for \quad 20^\circ C < t \le 600^\circ C \\ \frac{E(t)}{E(20)} &= \frac{690-0.69t}{t-53.5} , \quad for \quad 600^\circ C < t \le 1000^\circ C \end{aligned} \tag{9}$$

For Poisson's ratio:

$$\begin{aligned} \Upsilon(t) &= 3.78\times10^{-5}t + 0.283 , \quad for \quad 0 \le t \le 450^\circ C \\ \Upsilon(t) &= 9.20\times10^{-5}t + 0.259 , \quad for \quad t > 450^\circ C \end{aligned} \tag{10}$$

Since the density variance is negligible, the ratio $\frac{v(t)}{v(20)}$ can be calculated as shown in Figure 4-14 (a).

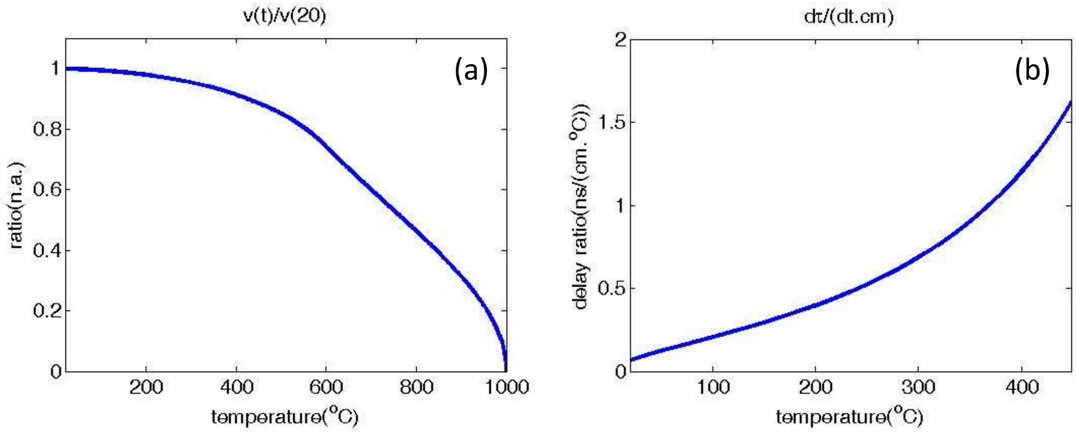

Figure 4-14. (a) The ratio of the sound velocity at temperatures from 0-1000°C to the sound velocity at 20°C; (b) the ratio of the fly time variance at temperatures from 0-1000°C to the acoustic wave propagating distance

Since Eq. 9 is not an accurate description of the sound speed when temperature approaches the melting point, we only consider situations below 450°C to get an estimation of fly time delay. Using the longitudinal wave speed in iron at room temperature (v(20)=5130m/s), the ratio of fly time variance over temperature difference and distance between the voids and the FBG is presented in Figure 4-14(b). The lowest response rate appears at the low temperature end and the value is about 0.1ns/(cm·°C). It means that with 1cm distance between voids and FBG, the signal acquiring and analysis process will need to have a temporal resolution higher than 1ns to obtain a 10°C temperature resolution. Thus, 1cm was set as the starting point in the future temperature monitoring experiments.

5 Simulation of the Fiber Bragg grating response to short acoustic pulse

In conventional FBG acoustic detection methods, it is assumed that the width of the acoustic pulses is much longer than the physical length of the detecting FBG. Under this assumption, the strain exerted on the FBG can be approximated to be uniform at any given time. Therefore, the shape of the acoustic pulse can be easily reconstructed from the intensity change of the reflected light, as shown in Figure 5-1.

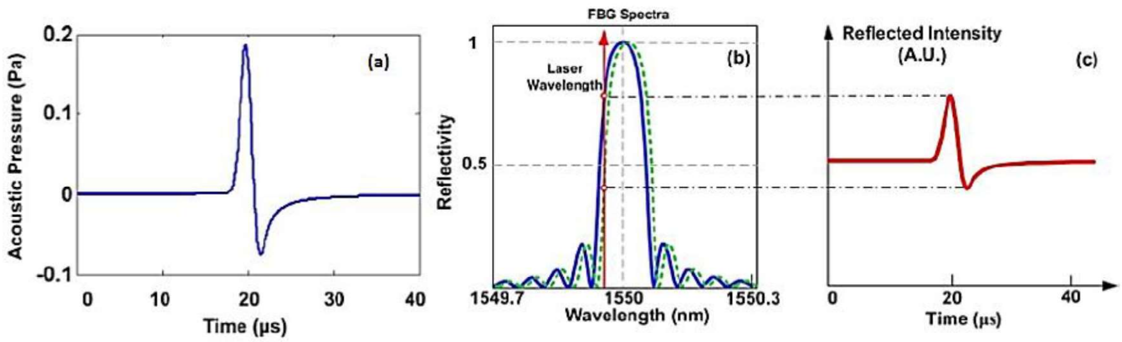

Figure 5-1. While a slow acoustic pulse (a) passes through an FBG, the instantaneous stress will be indicated by a shift in its reflection spectrum (b). The reflection intensity of a laser with its wavelength fixed on one edge of the main peak will be modulated in response to the stress wave (c).

However, this assumption is not applicable in our acoustic defect detection scheme. To detect a defect in metal, the equivalent wavelength of the acoustic wave must be shorter than the dimension of the defect. Since the size of the defects in metal could be as small as several millimeters, the effective wavelength of the acoustic pulse has to be at the sub-millimeter level, which is even shorter than the length of most FBGs. Thus it is necessary to analyze the temporal response of an FBG to a relatively short acoustic pulse in order to understand the recorded AE in the following experiments.

5.1.1 Simulation theory

In this section, the coupled-mode theory and the transfer-matrix method are used to simulate the reflection spectrum of an FBG.

In the coupled-mode theory, the electric field is written as a superposition of the forward and backward propagating modes:

$$E(x,y,z) = b_1(z)\Psi(x,y,z) + b_{-1}(z)\Psi(x,y,z) \tag{11}$$

where ψ satisfies the scalar wave equation for an unperturbed fiber:

$$\begin{gathered}\{\nabla_t^{\,2} + k^2\overline{n}^2(x,y) - \beta^2\}\psi = 0 \\ \nabla_t^{\,2} = \partial^2/\partial x^2 + \partial^2/\partial y^2\end{gathered} \tag{12}$$

where $k = \omega / c$ is the wavenumber in vacuum and $\beta = n_{eff} k$ is the scalar propagation constant.

Assuming the FBG refractive index perturbation has the following periodic form:

$$n^2 - \bar{n}^2 = \Delta n_{ac}(z)\cos(\frac{2\pi}{\Lambda} z + \theta(z)) \tag{13}$$

where Δn_{ac} is the amplitude of the refractive index change, and Λ is the period of the FBG.

The forward propagating component *t*(*z*) and backward propagating component *r*(*z*) follow the coupled-mode equations:

$$\begin{cases} \dfrac{dt}{dz} = +i\delta t + q(z) r \\ \dfrac{dr}{dz} = -i\delta t + q^*(z) r \end{cases} \tag{14}$$

where $\delta = \beta - \pi / \Lambda$, $|q(z)| = \dfrac{\pi \Delta n_{ac}(z)}{\lambda}$ and $\arg(q(z)) = \theta(z) + \dfrac{\pi}{2}$.

The coupled-mode equations shown in Eq. 14 can be written in transfer matrix form as[20]:

$$\begin{bmatrix} t(z+\Delta z) \\ r(z+\Delta z) \end{bmatrix} = \begin{bmatrix} \cosh(\gamma\Delta z) + i\dfrac{\delta}{\gamma}\sinh(\gamma\Delta z) & \dfrac{q}{\gamma}\sinh(\gamma\Delta z) \\ \dfrac{q^*}{\gamma}\sinh(\gamma\Delta z) & \cosh(\gamma\Delta z) - i\dfrac{\delta}{\gamma}\sinh(\gamma\Delta z) \end{bmatrix} \begin{bmatrix} t(z) \\ r(z) \end{bmatrix} \tag{15}$$

By dividing the FBG into small sections and multiply all the transfer matrix of each section, the relationship between the electric field at position L and at position 0 on the fiber can be written as:

$$\begin{bmatrix} t(L) \\ r(L) \end{bmatrix} = T \begin{bmatrix} t(0) \\ r(0) \end{bmatrix} \qquad T = \begin{bmatrix} T_{11} & T_{12} \\ T_{21} & T_{22} \end{bmatrix} \tag{16}$$

where the matrix *T* stands for the chain multiplication of the transfer matrices of each section. The relative values of *t*(*L*), *r*(*L*) and *r*(0) are calculated by defining *t*(0) to be 1. When using a weak FBG, the relative propagating wave intensity *t*(*L*) is approximately 1, so the back reflected intensity *r*(0) can be calculated as:

$$r(0) = -T_{21} / T_{22} \tag{17}$$

5.1.2 Simulation result

A 32ns Gaussian acoustic pulse was used in the simulation, which is chosen according to the pulse width of the pump laser currently used in the system. The length of the detecting FBG was set to 1.5mm. The acoustic detection was conducted by using a laser with a wavelength at the rising edge of the FBG main reflection peak. When the short acoustic pulse passed the FBG, the period of the FBG was partially modulated, and the instantaneous reflection intensity could be calculated at any given time. The calculated reflection intensity signal is shown in Figure 5-2.

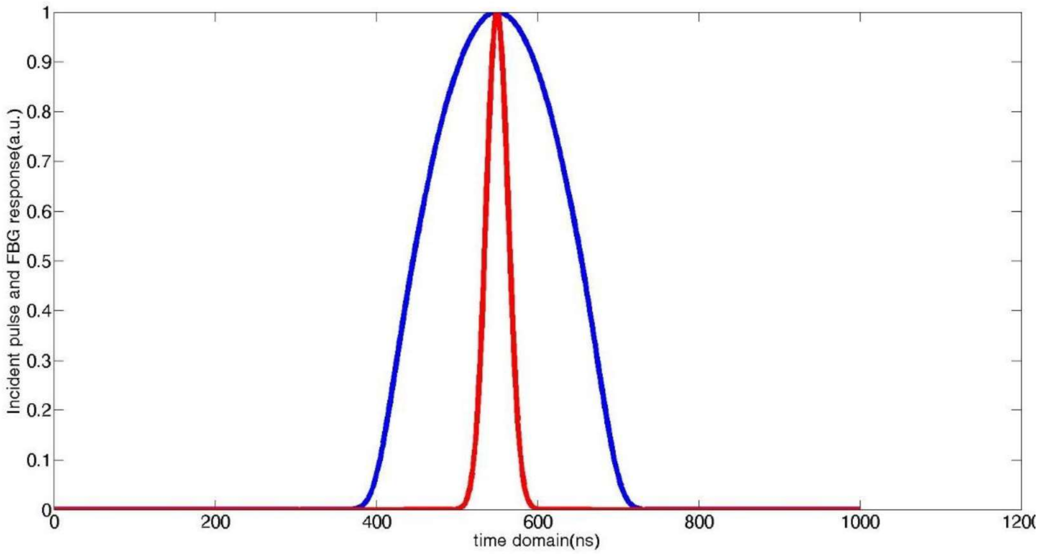

Figure 5-2. The reflection response of a 1.5mm long FBG to a 32ns (0.16mm long in space) acoustic pulse. Red line: acoustic pulse. Blue line: simulated FBG response signal.

As shown in the simulation result, the response signal has a length of ~220ns in time, and ~1.1mm in space correspondingly. The result can be understood as that the pulse width of the recorded acoustic pulse is approximately equal to the sum of the original pulse width and the acoustic wave travel time on the FBG. This means using a shorter FBG can improve the spatial resolution of the detector, as long as the acoustic pulse is shorter than the FBG. The result is compared with the experiment results in the following section 6.2.3.

6 Test and discussion of the laser induced plasma based acoustic generation scheme

In this section, several mechanisms for fiber optics based acoustic generation were analyzed and tested. These included the laser induced plasma mechanism and two thermal expansion based methods. A fiber-optics acoustic generation unit (AGU) was designed and fabricated based on each of these acoustic generation mechanisms. After testing and comparing the performance of these three AGUs, the light scattering based mechanism was chosen to build the FO-SHM used for this project.

6.1 LIP based Acoustic excitation

6.1.1 Principle of LIP based acoustic excitation

The mechanisms of laser-induced acoustic wave excitation include electrostriction, thermal expansion, photochemical changes, gas evolution, and breakdown of plasma formation [21]. Among all these mechanisms, Laser Induced Plasma (LIP) formation breakdown has the highest optical-acoustic conversion efficiency, which can reach around 30% [22]. On the other hand, conventional thermal expansion only has a conversion efficiency in the order of 10^{-12} to 10^{-8} [21]. Studies show that LIP can generate strong acoustic shock wave in both the water confined geometry and glass confined geometry with a fast temporal response to the laser pulse, as shown in Figure 6-1 [23, 24].

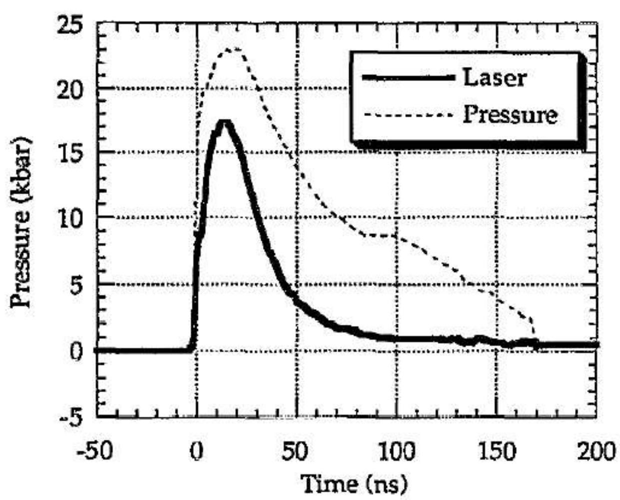

Figure 6-1. Pulse laser (solid line) and laser-induced pressure (dotted line) at a power density of 2.6GW/cm² with water confinement [24].

6.1.2 Experimental comparison of the opto-acoustic conversion efficiency between thermal expansion and LIP

In this section, we presented a test to compare the opto-acoustic generation efficiency between the LIP process and the thermal expansion process. A free space laser beam was focused onto the surface of an aluminum sample to excite acoustic vibration on the sample either through thermal expansion or laser induced plasma breakdown, depending on the laser intensity. A PZT transducer attached on the aluminum sample recorded the acoustic signal. The relationship between the laser energy density and the acoustic intensity was then plotted to show the difference in opto-acoustic converting efficiency for LIP and thermal expansion process. As shown in Figure 6-2, a Nd:YAG pulsed laser with 50ns pulse width was used as the acoustic excitation laser, and the illuminated spot is about $1mm^2$.

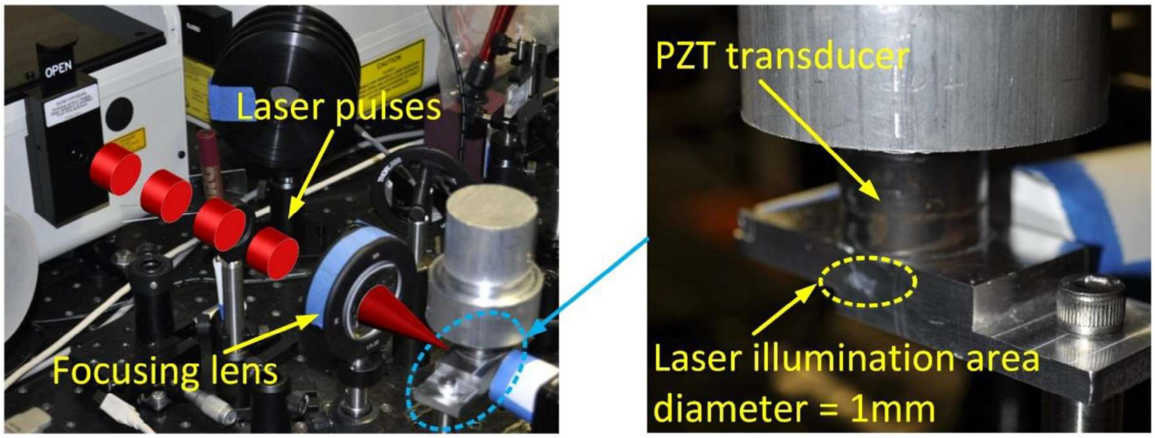

Figure 6-2 Experimental setup to test the opto-acoustic converting efficiency of LIP and thermal expansion process

During the experiment, the laser intensity was gradually increased from the lowest setting. When the calculated energy density was lower than 0.05 J/cm^2, there is no plasma generated due to the high threshold of the LIP process. When the energy density pass 0.05 J/cm^2, the bremsstrahlung radiation associated with LIP process [25] can be visually observed which indicated the LIP process has taken place.

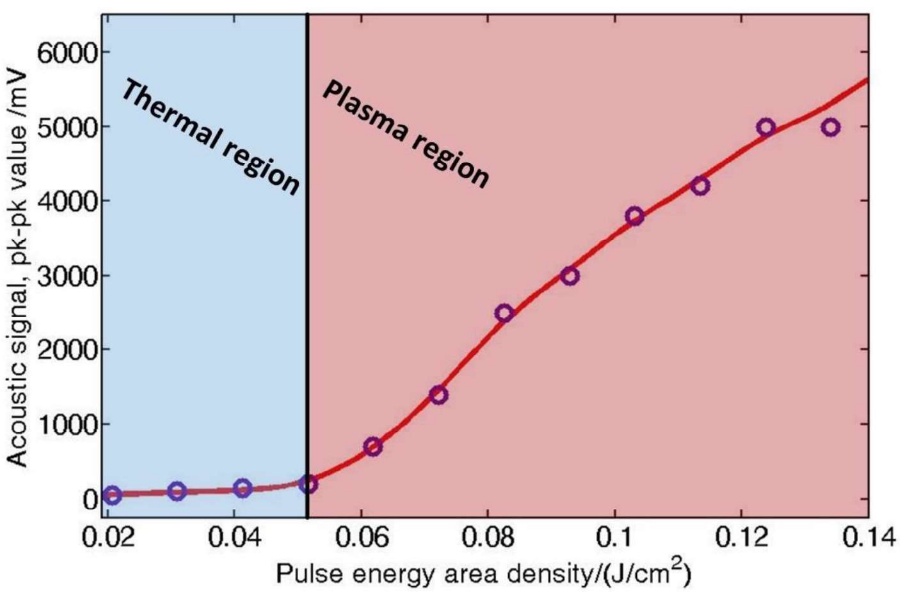

Figure 6-3 Experimental result of the opto-acoustic converting efficiency for the LIP process and the thermal expansion process

The test result is shown in Figure 4-5, the acoustic intensity is represented by the peak-to-peak value of the recorded acoustic signal. In this graph, the opto-acoustic efficiency can be represented by the gradient of the fitted curve. It can be seen that, the opto-acoustic efficiency becomes much stronger when the energy density passes the plasma threshold. This indicates that the LIP process is able to generate much stronger acoustic signal compared to the thermal expansion process, and applying this process in a glass confined geometry (using optical fiber) should be a good candidate to obtain maximum acoustic generation efficiency.

6.2 Demonstration of single point LIP based acoustic generation and detection

6.2.1 *Single point acoustic generating unit*

To test generating acoustic wave inside a solid with pulsed laser and optical fiber, a demonstrative LIP acoustic generation unit was fabricated, as shown in Figure 6-4. A 105/125μm step index MM fiber was used to guide the laser. The large core in the fiber will allow higher energy transmission than small core fibers, and the step-index structure of the fiber could also relieve the energy intensity density in the core center thanks to the weaker self-focusing effect comparing with gradient index fibers. The polished end of the fiber was buried in a tin pool held by a copper casting as the acoustic conductor, allowing the usage of both PZT and FBG as the acoustic detector for characterization.

Figure 6-4. Demonstrative optical fiber LIP acoustic generating unit.

6.2.2 *Single point acoustic detecting unit*

Due to the short acoustic pulse width and broad frequency range of the LIP generated acoustic wave, it is difficult to receive an undistorted signal with a PZT. So we built an FBG based broadband acoustic detector to evaluate the LIP generated acoustic wave. The design of the acoustic detector is shown in Figure 6-5 (a). Matching the acoustic generating unit, another copper casting with a Tin pool was used to hold the FBG. To detect the acoustic wave propagating vertically, the FBG had to be deployed along the cylinder. The end of the fiber was led out of the tin pool and looped to eliminate the reflection from the end surface of the fiber. The FBG was designed to be located only 5mm from the detecting surface. The fabricated unit is shown in Figure 6-5 (b).

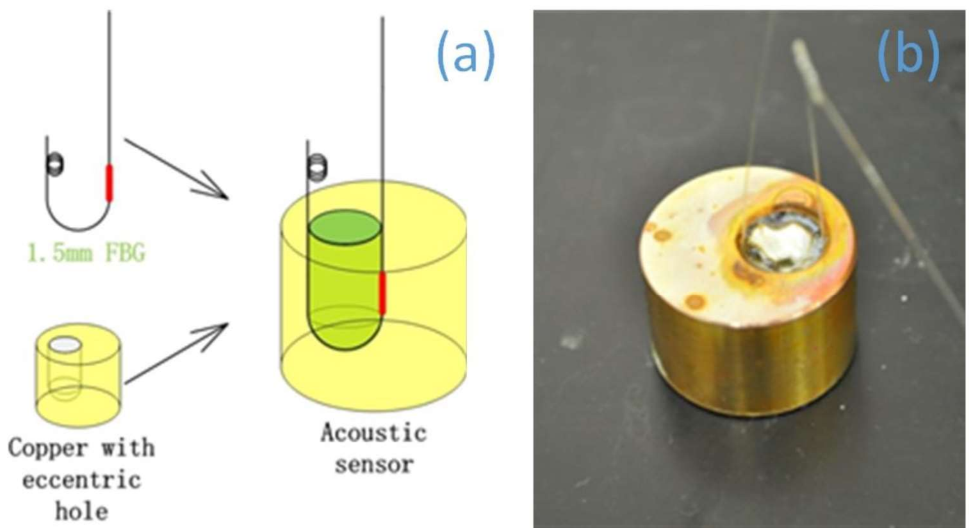

Figure 6-5. Demonstrative FBG acoustic detection unit design (a) and the fabricated unit (b).

6.2.3 *Single point acoustic generation and detection test*

The acoustic generating and acoustic detecting units were held together for a preliminary demonstrative test. A Nd:YAG nanosecond pulse laser was used to generate the LIP exciting light pulse. A tunable laser and an oscilloscope were used to detect the acoustic signal. The system setup scheme is shown in Figure 6-6.

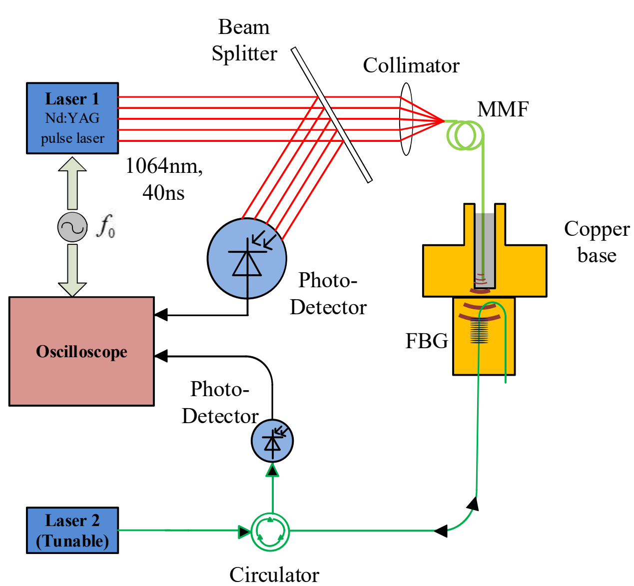

Figure 6-6. System setup of the single point acoustic generation and detection demonstration.

The FBG used in the acoustic detection unit is about 1.5mm long. Its reflection spectrum is shown in Figure 6-7. The detecting laser wavelength is set at 1558.5 nm, which is on the rising edge of the FBG main peak.

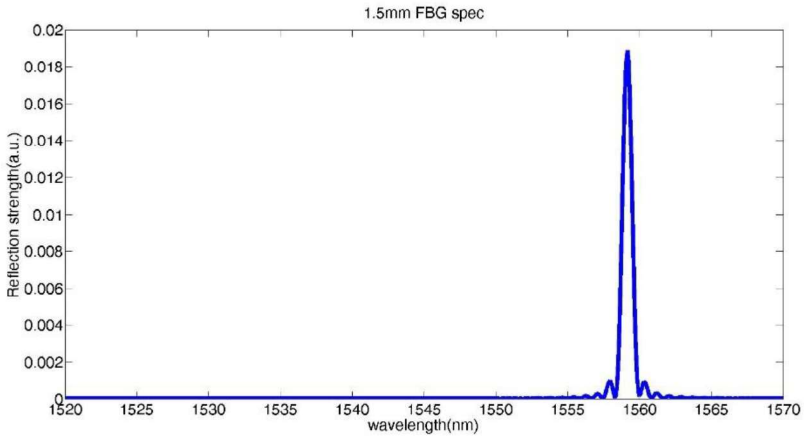

Figure 6-7. Reflection spectrum of the FBG used in the acoustic detector.

The acoustic pulse width generated was calculated to be 0.16mm in space, according to the 40ns time width of the laser pulses. As shown in Figure 6-8, the experiment result (solid line) agrees well with the simulation result (dashed line), only with slight shape distortion and a negative tail.

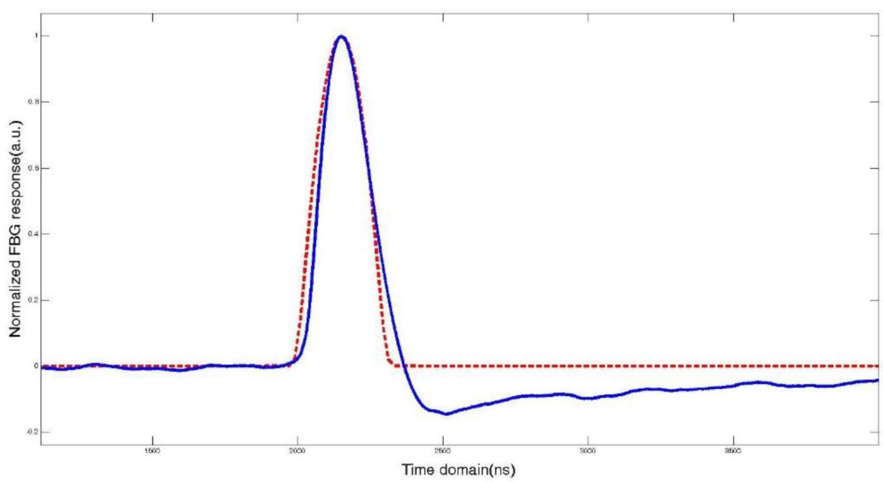

Figure 6-8. Comparison of the experimental result (solid blue line) and the simulation result (dashed red line).

To test the long distance propagation of a LIP generated acoustic wave in solid, another demonstration was performed with a long copper rod. The experiment setup is shown in Figure 6-9.

Figure 6-9. Preliminary FO-SHM unit demonstration test: (a) acoustic generation and detection units directly attached; (b) acoustic wave passes through copper rod before detected by FBG

The acoustic signals generated by 1064nm laser pulses with 0.5mJ pulse energy are shown in Figure 6-10. The signals have been averaged 500 times. As indicated by the signal strength in both results, the acoustic vibration generated by the LIP mechanism should also be able to produce recognizable signal when implemented on a work piece with similar dimensions.

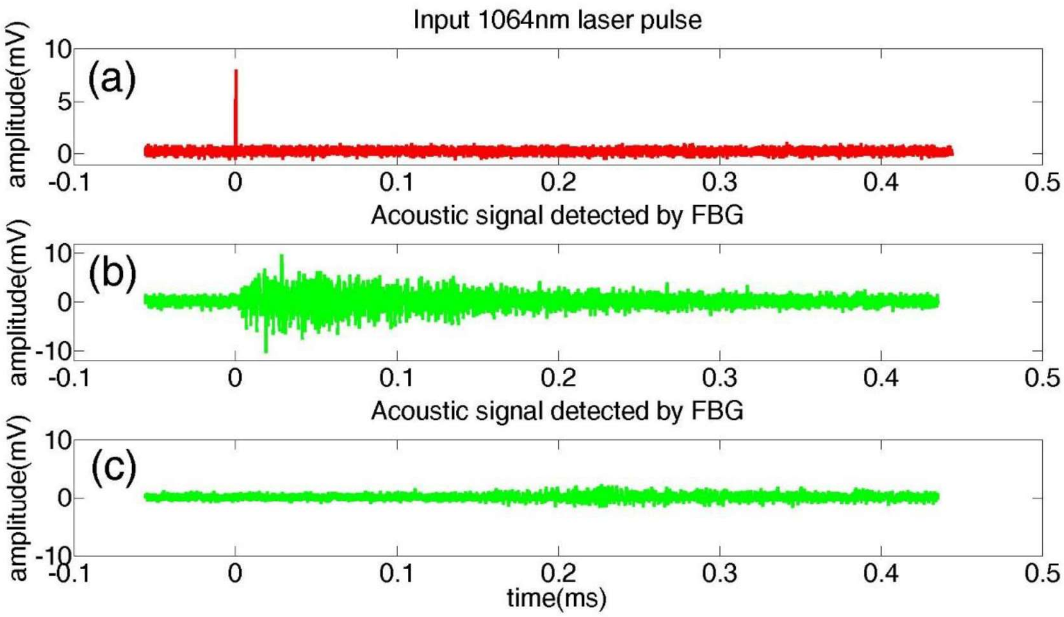

Figure 6-10. Signals acquired with the demonstrative FO-SHM unit: (a) 1064nm laser pulse; (b) acoustic signal acquired with FBG unit directly attached to acoustic generation unit; (c) acoustic signal acquired with FBG unit and acoustic generation unit separated by a piece of 40cm-long copper rod

6.3 Multiplexable LIP & FBG Based FO-SHM Element Design and Fabrication

6.3.1 Multiplexable LIP based in-fiber acoustic generating unit design

As discussed in the previous section, the LIP formation breakdown can be generated in a confined geometry to excite strong acoustic wave. To achieve the goal of multi-point sensing, a multiplexable in-fiber acoustic excitation structure design was proposed. As shown in Figure 6-11, thin metal films are deployed partially inside a multimode fiber, serving as the laser absorbing media which generate laser induced plasma. The part of the laser beam that misses the metal target will redistribute in the fiber core as it propagates, and hit the following targets.

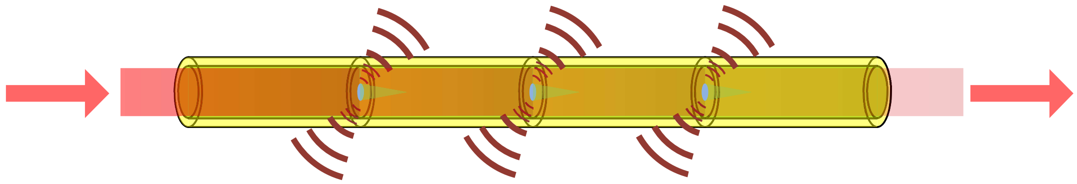

Figure 6-11. Structure of multiplexing in-fiber LIP acoustic generating units.

The multimode fiber chosen for the system is 105/125μm step index fiber, due to its large core diameter and standard cladding layer geometry. More importantly, unlike the graded-index multimode fibers which have the GRIN lens effect [26, 27], step-index multimode fibers have no focusing effect inside the core, which leads to a higher damage threshold than graded-index fibers with similar core diameters.

To achieve proper absorption rate on each absorber for the purpose of element multiplexing, the size of the metal films was chosen to be 5-10μm for the 105μm core fiber. For a quasi-uniform light distribution in the core, the calculation shows that 4.8%-9.5% of light power will be absorbed on each film. A multiplexing of 10 units will reduce the initial light intensity to 36.7%-61.4%, which corresponds to an acoustic intensity drop of 2.1dB-4.3dB between the first and the 10^{th} unit.

The thickness of the metal film is another important parameter that needs optimization. A very thick metal film will be extremely time-consuming to fabricate, and will bring challenge to the splicing of the coated fiber. On the other hand, a very thin metal layer (nanometer scale) may degrade quickly under strong laser pulse exposure, which will greatly reduce the element lifetime. In the tested designs, thickness of 1-5μm was used.

6.3.2 LIP based FO-SHM element design

A single FO-SHM element is a combination of an acoustic generating unit and an FBG acoustic detecting unit. Figure 6-12 shows the design of an LIP based FO-SHM element. In the LIP based FO-SHM system, a multimode fiber with an LIP unit and a single mode fiber with an FBG unit will be attached side by side with the two units separated by a certain distance.

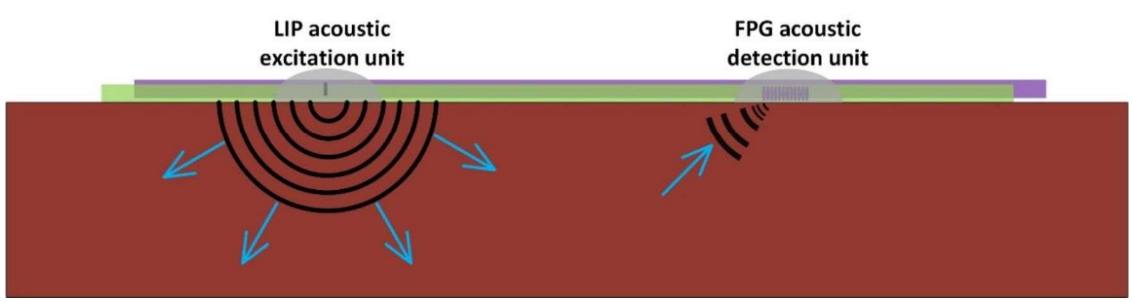

Figure 6-12. Surface attached LIP based single FO-SHM element.

The purpose of maintaining the space between the acoustic generating unit and detecting unit is to provide the system the capability of temperature compensation. The P-wave travelling directly from the generator to the detector depends on the temperature in the medium and will not be affected by flaws and corrosions within the specimen. By monitoring the speed of the P-wave, the temperature of the monitored specimen could be deduced, which can be used to compensate the temperature influence on the FBG in the stress measurement. To optimize the distance between the two units, the geometry of the specimen needs to be taken into consideration in order to avoid overlapping between the direct wave along the surface and signal waves from the inner structures.

6.3.3 Fabrication of a LIP based fiber optics acoustic generation unit (FO-AGU)

The fabrication procedure of an LIP based FO-SHM element was designed as followed:

1. Cleave a 105/125μm fiber;
2. Mill a 10μm diameter, 2μm deep well on the cleaved fiber end with FIB;
3. Fill the well with deposited platinum with FIB;
4. Cleave another 105/125μm fiber and splice it to the treated end of the first fiber, using a standard multimode fiber splicing technique;
5. Observe the acoustic excitation unit from the side under microscope, adjust the splicing parameters and redo the procedure if needed;
6. Splice a 2mm long, -5dB FBG in an SMF-28e single mode fiber;
7. Attach these two fibers side by side, with an optimized distance between the two units.

A demonstrative element was fabricated, as shown in Figure 6-13.

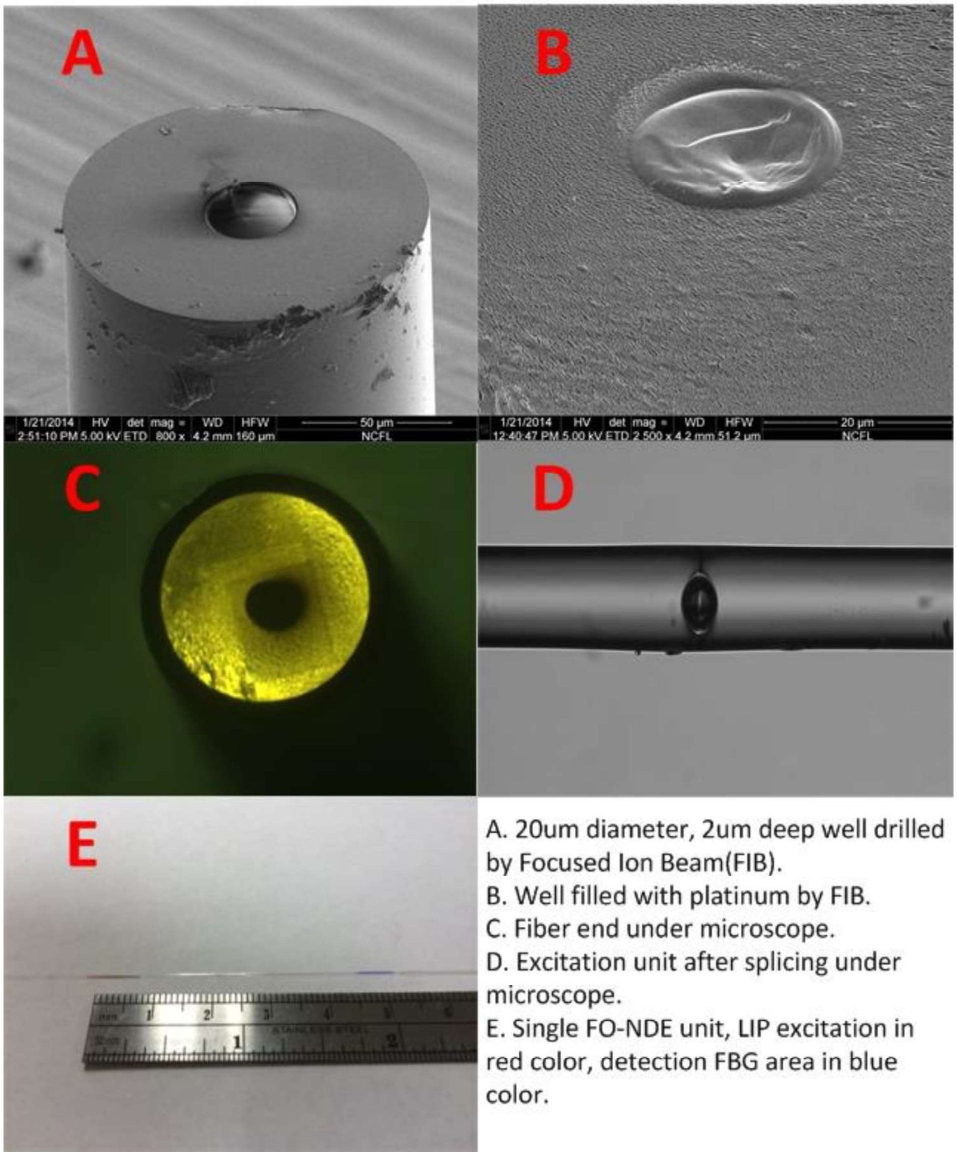

Figure 6-13. Fabrication of a demonstrative LIP based FO-SHM element.

6.4 LIP based FO-AGU test

6.4.1 First unit test

As presented in the previous section, the first LIP based FO-AGU was successfully fabricated with Focused Ion Beam (FIB) and fiber splicing techniques. A measurement with a light source and a power meter showed a 64% transmission rate of the unit. In this section, the unit was put to the test in a simplified test bench.

A PZT detector was used to monitor the generated acoustic wave. A reference acoustic source was made with a fiber pointing to a blade. The unit under test, the reference and the detector were all immersed in water for convenient acoustic transmission. The setup is shown in Figure 6-14 (PZT unit not shown).

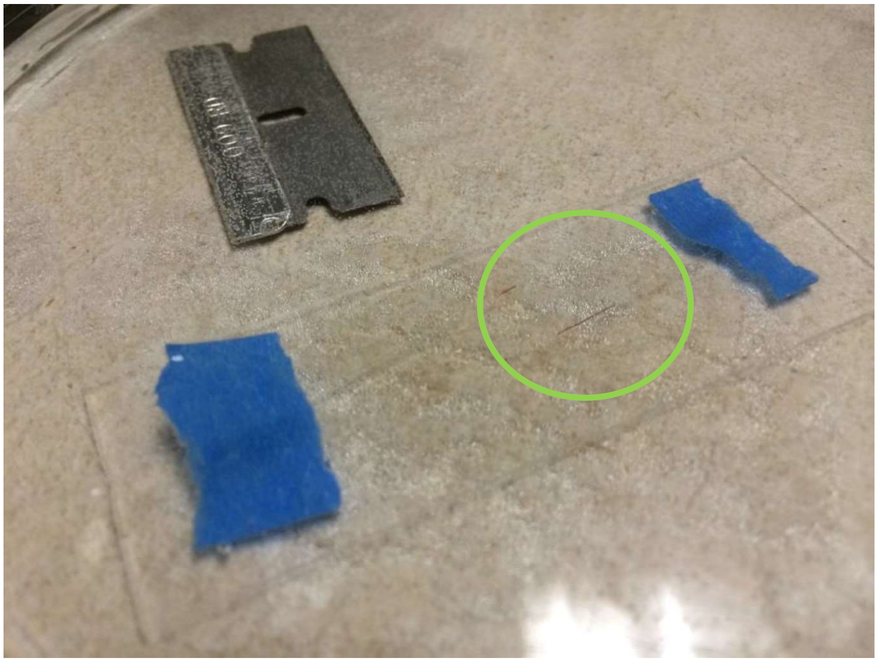

Figure 6-14. LIP unit test setup and unit breakage

When excited with laser pulses with 250uJ pulse energy, the unit broke from the splicing point (Marked with the green circle in Figure 6). After the unit broke, a strong acoustic signal could still be detected by the PZT for several pulses, and then the signal vanished. The phenomenon is believed to be a result of the quick non-confined LIP breakdown of the metal layer remaining on the broken fiber end.

Both fractures of the broken LIP unit were observed under an optical microscope, as shown in Figure 6-15.

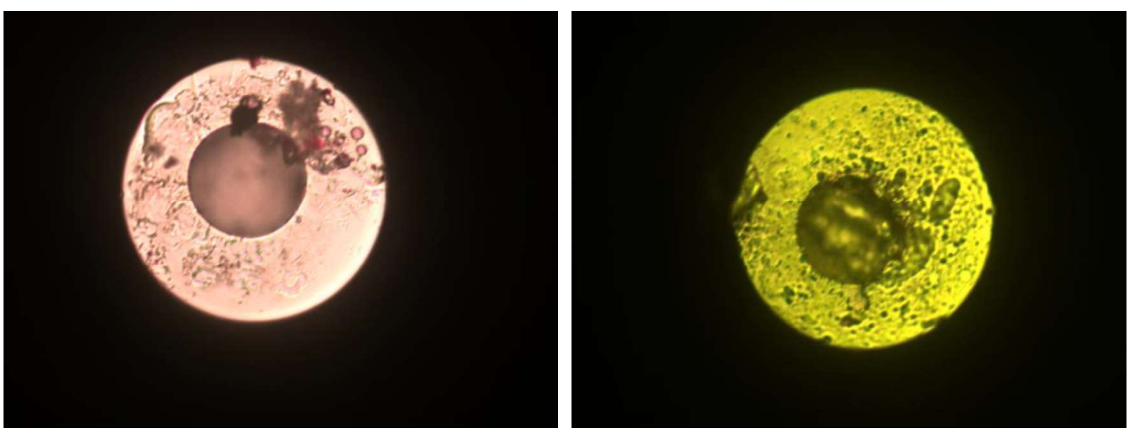

(a) (b)

Figure 6-15. Microscope images of the two fiber ends taken after the unit broke: (a) the fiber with the well for the metal layer and (b) the mating fiber

Comparing the image of the metal-coated fiber end taken before splicing (Figure 6-16) with Figure 6-15 (a), it is obvious that the metal film is totally blown off.

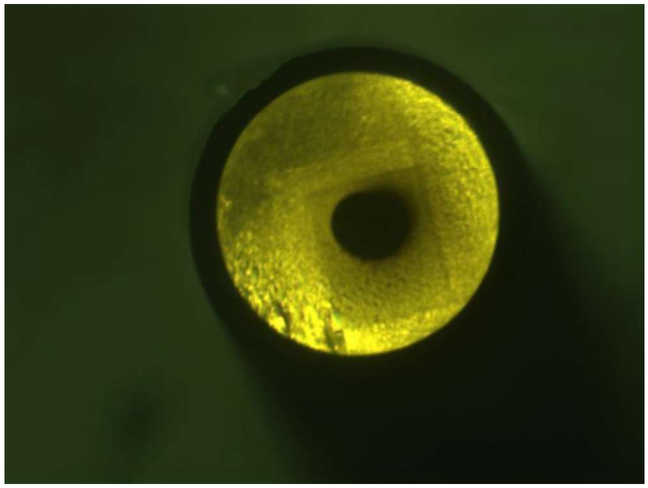

Figure 6-16. Image of the metal coated fiber end before spliced with the mating fiber

It is also worth noting that both fiber ends of the broken unit had smooth fracture surfaces. During the fabrication of the first unit, relatively low arcing energy was used to avoid metal deforming. However, according to the result, only a small part of the two fibers was spliced together, resulting in a low mechanical strength that could not hold the structure under the force of the explosion on the metal sheet. It indicates that stronger splicing is the key to enhancing the signal strength and extending sensor robustness.

6.4.2 Second unit test

To obtain higher mechanical strength, the splicing conditions were adjusted in the fabrication of the second LIP based acoustic generation unit. By applying a cleaning arc before the main arc and increasing the main arc power, the two fiber ends were tightly bonded together, as shown in Figure 6-17. However, after the splicing, a bubble was formed in the unit.

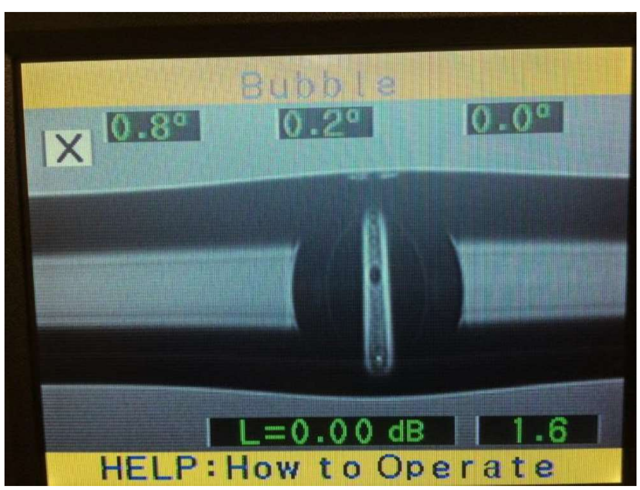

Figure 6-17. Improved splicing of the second LIP FO-AGU

We believe the bubble was formed by the gap in the half-filled well on the fiber tip. In the FIB machining, the metal did not perfectly fill the well, leaving an air void when the two fiber ends met. During the arcing, the air void expanded under high temperature and formed a bubble in the softened silica. The result of a transmission test shows a transmission rate of ~10%, which is much lower than the designed value. Comparing with the first unit, it is obvious that the bubble is the major cause of the high loss.

The unit is then tested in the same setup described in the former section. In the test, strong acoustic pulses were generated, and no evidence of breaking was observed after multiple pulses. One of the acoustic pulses recorded by an oscilloscope is shown in Figure 6-18.

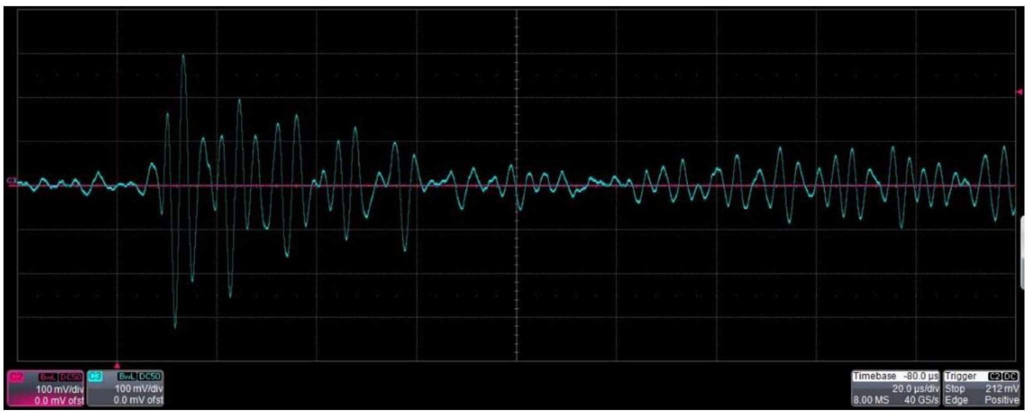

Figure 6-18. Acoustic signal generated by the second LIP unit and detected by a PZT detector in water

6.5 Conclusion

In this phase, we have designed, fabricated and tested the LIP based acoustic generation units, which are able to generate strong acoustic vibration. Although the performance of this LIP based FO-AGU is promising in terms of acoustic intensity, it brings challenges in the fabrication process (time-consuming and very costly). In addition, this structure reduces the mechanical strength of the optical fiber so it may bring problems when attached to a sample and used in a high temperature environment.

7 Test and comparison of two thermal expansion based acoustic generation schemes

Due to the problems associated with the LIP based FO-SHM design, two thermal expansion based acoustic generation schemes were studied. They are Erbium-doped fiber (EDF) based method and scattering-light based method. The design, test and discussion of these two routes are presented in this section.

7.1 EDF based acoustic generation

7.1.1 Mechanism of acoustic generation with EDF

The acoustic generation with EDF is based on the thermal expansion of the fiber. When the laser energy is absorbed by the Er3+ ions in an EDF, part of the energy will transform into heat and cause thermal expansion. When excited by a laser pulse, acoustic waves are generated by the instantaneous expansion and contraction of the fiber.

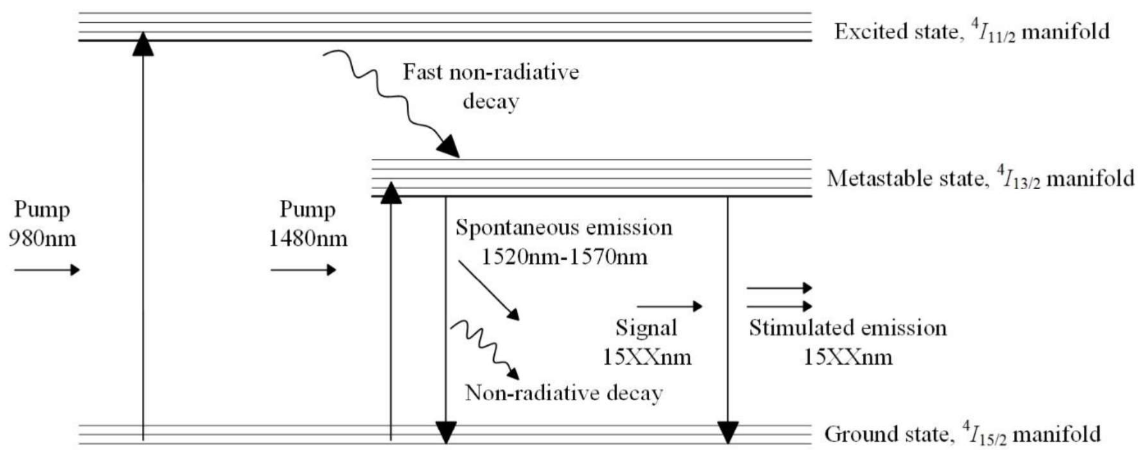

Figure 7-1 level diagram of Er 3+in EDF

Among all the energy transitions of Er3+ as shown in Figure 7-1, the only one that can generate acoustic signal efficiently is the fast non-radiative decay from the excited state to the metastable state. According to former research [28], the lifetime of the excited state $^4I_{11/2}$ is between 1~10μs, which is fast enough for the acoustic generation. Another transition which can possibly generate thermal expansion is from the metastable state to the ground state. This transition includes both spontaneous emission and non-radiative decay, while only the latter one is related to heat generation. As reported in literature [28-31], the lifetime of the metastable state $^4I_{13/2}$ is ~10ms, which is too long for acoustic wave generation application.

In summary, the only transition we can utilize to generate acoustic wave efficiently is the non-radiative decay from $^4I_{11/2}$ to $^4I_{13/2}$. Based on the 1μs~10μs timescale of this transition, it can be calculated that the acoustic wave we could generate with EDF will have a wavelength of 1~10mm on metal.

7.1.2 Determination of the interrogation wavelength in an EDF based system

Using an EDF based acoustic generation scheme, the FBG interrogation light can share the same single-mode fiber with the EDF exciting light, simplifying the element design and increasing its robustness. Because the probe light will pass through the EDF section, its working wavelength should avoid the EDF absorption wavelength range. According to the absorption spectrum of EDFs as shown in Figure 7-2, its absorption peak centering at 1530nm covers widely from E-band to L-band, which is the most widely used spectrum range in fiber optics. If the interrogation light wavelength falls within this range, saturated absorption effect will be introduced, confusing the intensity-based interrogation on the FBG elements.

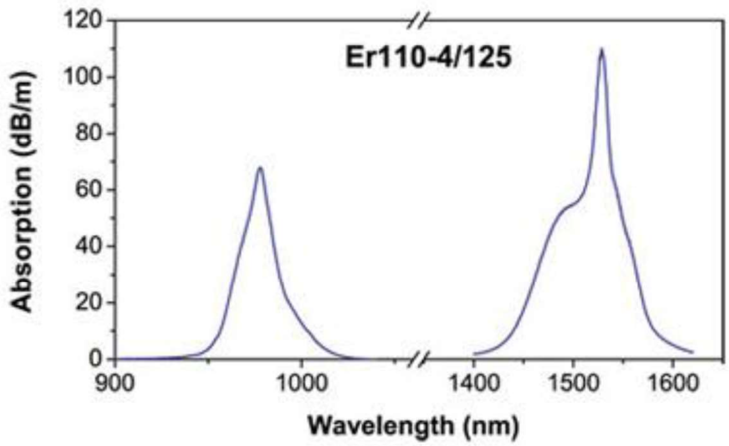

Figure 7-2 Absorption spectrum of Er110-4/125 fiber from Thorlabs

To avoid this potential issue, an O-band (1260nm-1360nm) light source and FBGs should be used for interrogation. By avoiding the absorption peak, the saturated absorption effect could be eliminated and lower transmission loss of the interrogation light could be achieved. Light sources within this wavelength range are widely available in market, and the slightly higher fiber loss in this wavelength range comparing to E-band and L-band is negligible for our relatively short application length.

7.1.3 Options for the 980nm acoustic generating laser

i. Optical Parametric Oscillator (OPO) laser with pulse broadening

The first option is to generate high power 980nm light pulses is to use an OPO laser, which can offer high peak power at relatively low repetition rate. However, due to the non-linearity nature of OPO generation, the pulse width of this kind of laser is too short for our application (<10ns). To generate a sub-µs 980nm pulse with OPO laser, pulses broadening will be necessary, which will substantially increase the system complexity.

ii. Diode laser

While most 980nm lasers in the market are diode lasers, the beam quality of these lasers are usually low comparing to long cavity lasers. As a result, most high peak power fiber-coupled 980nm lasers use multimode fibers. During our market survey, one vendor (ALPhANOV) was found who was able to make single-mode fiber coupled 980nm pulsed laser with a peak power of 2.2W, which is high enough according to our estimation.

7.1.4 EDF based FO-SHM element design

A design of an EDF based FO-SHM element is shown in Figure 7-3. Thorlabs ER80-4/125 EDF is used, which has an absorption of ~60dB/m at 980nm. The length of the EDF section is designed to be 1cm, resulting in ~12% absorption of the acoustic generating light in each element. A 5mm-long FBG with acoustic response frequency up to ~1MHz will be used as the detector. The distance between the EDF and the FBG is 10cm, allowing enough traveling distance for accurate acoustic speed measurement. All parameters are subject to adjustment according to test results in the future.

Figure 7-3. Design of an EDF based FO-SHM element

7.2 Scattering light&metal absorption based acoustic generation

7.2.1 Light scattering based FO-SHM element design

Another thermal expansion based design is to scatter the laser pulses out of the optical fiber so that the surrounding material, either the adhesive or the metal, can absorb the laser energy and generate acoustic waves. This FO-SHM element design uses two fiber cores, one multimode core for acoustic generation light propagation and the other single-mode core for probe light propagation. A femtosecond laser will be used to inscribe scattering voids inside the large diameter core to generate scattered light which leaks out of the core and excite acoustic wave by interacting with the surrounding material. The same femtosecond laser will also be used to inscribe type-II FBGs for acoustic detection so the whole fabrication process can be accomplished with one single setup. This new design eliminates the needs for fiber coating removal and fiber splicing, hence significantly increases the mechanical strength of the fiber device and reduces the risk of fiber breakage during embedment and fast temperature changes. Another advantage of this design is its intrinsic high temperature compatibility. Scattering voids and type-II FBGs are created by localized material melting and compaction associated with multi-photon ionization induced dielectric breakdown, and which are stable up to the glass transition temperature [32]. For silica fiber, type-II FBGs are reported to be stable during long time temperature cycling test up to 1050°C [33].

Based on the idea, three schemes were designed, from which the final design will be chosen based on the availability of the special fiber.

a. Scheme 1

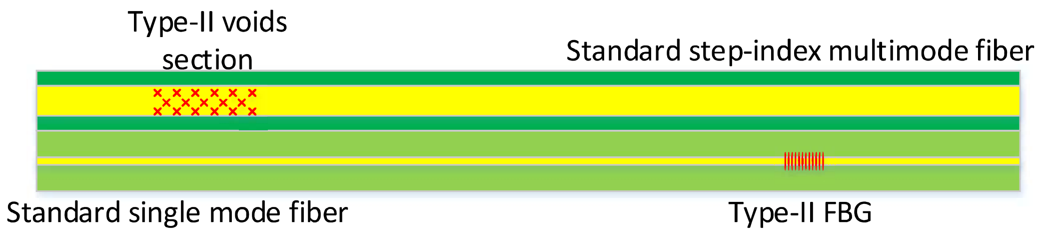

Figure 7-4. Standard multimode fiber + standard single mode fiber

This option uses two separate standard fiber and bond them together with a high temperature coating. A standard multimode fiber is inscribed with scattering voids and used as the acoustic generation unit. The FBG is inscribed in a standard single mode fiber and used as the acoustic detection unit. The advantage is that the acoustic generation light and probe light are completely isolated so there will not be any unwanted interference. The drawbacks are the increased overall size and the complexity in fiber embedment.

b. Scheme 2

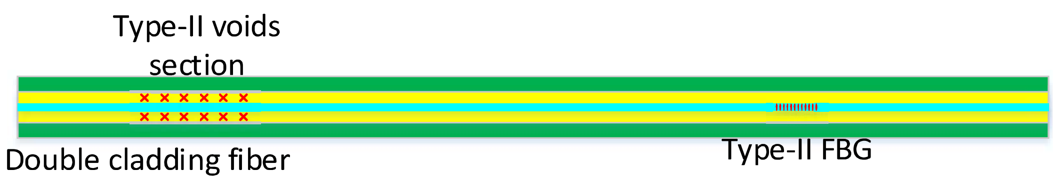

Figure 7-5. Un-doped double cladding fiber (DCF)

This option uses a double cladding fiber with undoped core and silica outer cladding. The acoustic generation light propagates inside the inner cladding and core, while the scattering voids are inscribed in the inner cladding only so it doesn't introduce additional loss to the probe light which propagates inside the single mode core. The FBG is inscribed inside the core with tight focus laser beam (spot size < 1um) so it generates a minimum loss to the acoustic generation light. This type of fiber needs custom fabrication, and can be pursued in the next phase of this project.

c. Scheme 3

Figure 7-6. Twin-core fiber

This option is similar to option 1 but uses a twin core fiber, a type of special fiber with two cores and one cladding. This type of fiber needs custom fabrication, and can be pursued in the next phase of this project.

7.3 Experimental comparison and analysis of the two thermal expansion based acoustic generation methods

7.3.1 Test system setup

In this phase, we built experimental setups to compare the acoustic generation capabilities of the proposed thermal expansion based acoustic generation methods. The system schematic is shown in Figure 7-7. A 980nm pulsed laser with 2W peak power was used as the acoustic excitation source and modulated by a function generator to output burst pulses with 1KHz burst rate and 90~200KHz pulse frequency. 10% of the total power was split and monitored by a photodetector, while the remaining power went into the acoustic generation unit (AGU), which in this experiment is a segment of single mode fiber with scattering voids or EDF. The AGU was buried inside a metal piece and a PZT was attached to monitor the generated acoustic signal. The PZT signal was then amplified by a band pass amplifier and averaged to show the acoustic signal on an oscilloscope. The light through the AGU was monitored by another photodetector as a reference on how much energy is absorbed by the AGU.

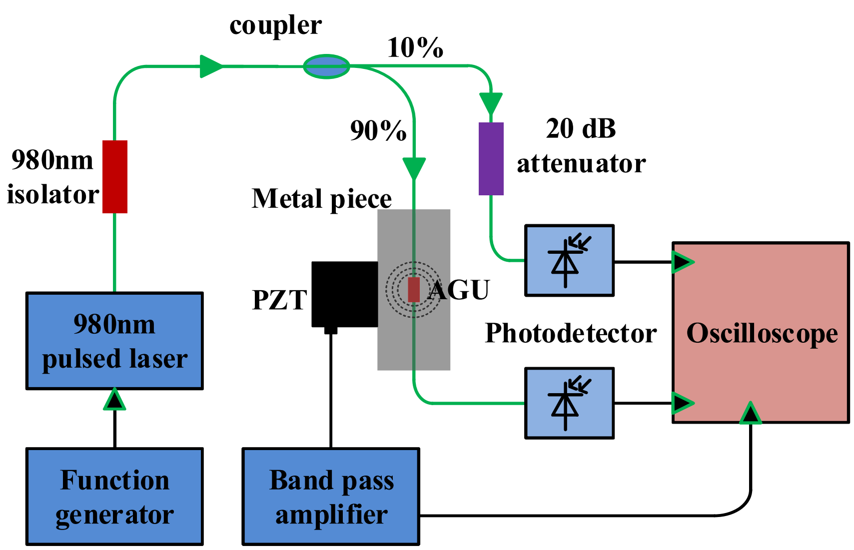

Figure 7-7. AGU test scheme with a PZT as the acoustic detector

The key components used in the experimental setup are listed as follows.

Table 2 Equipment used for thermal expansion based acoustic generation methods comparison

980nm pulsed laser	ALPhANOV PDM 980
C-band tunable laser	Newport TLB-6700
Oscilloscope	Lecroy 725Zi
Photodetector	Menlosystem FPD510
Balanced photodetector	Newport 2117-FC
Bandpass amplifier	Preamble 1822
Function generator	Tektronix AFG 3252

Pictures of the completed experimental setup are shown in Figure 7-8.

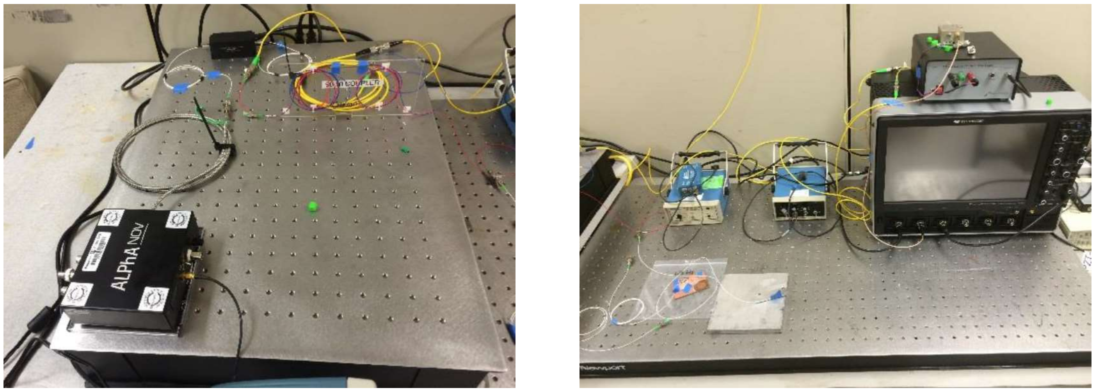

(a) (b)

Figure 7-8. Experimental setup of the EDF based FO-SHM system: (a) acoustic generation system using a 980nm pulsed laser; (b) test bench

To acquire high-power light pulses with specific pulse width, a burst square wave train was generated by a function generator as the controlling signal. As shown in Figure 7-9 (b), a laser power measurement shows a semi-square waveform with a peak power of ~1.5W. The frequency of the bursts was set at 1KHz, while the frequency of the square wave was set to be tunable from 100KHz to 3MHz.

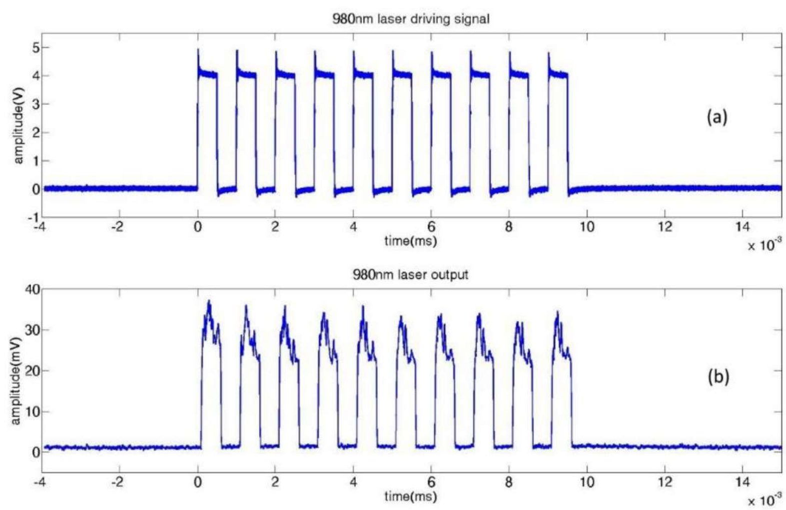

Figure 7-9. (a) Driving signal and (b) measured laser output power of the 980nm pulsed laser

7.3.2 Scattering acoustic generation vs EDF acoustic generation

Several tests were performed to compare the acoustic generation efficiency between the EDF-based method and the light scattering method. A typical one is shown in this section. Figure 7-10 shows the AGUs used in this experiment. The AGU shown in Figure 7-10(a) consists of 4 mm of SMF-28e single mode fiber with scattering voids inscribed. The distance between each void was ~0.5μm and the spot size of the femtosecond inscribing beam was less than 1μm. The AGU shown in Figure 7-10(b) was made of 40cm EDF and the bending radius was about 2.25cm which didn't cause much light leakage. BOth acoustic generation fiber sections are buried in the tin layer with a thickness around 3mm. The PZT acoustic detector was attached to the back of the copper plate, with a thin layer of ultrasonic gel applied in between to reduce the acoustic wave reflection on the boundary.

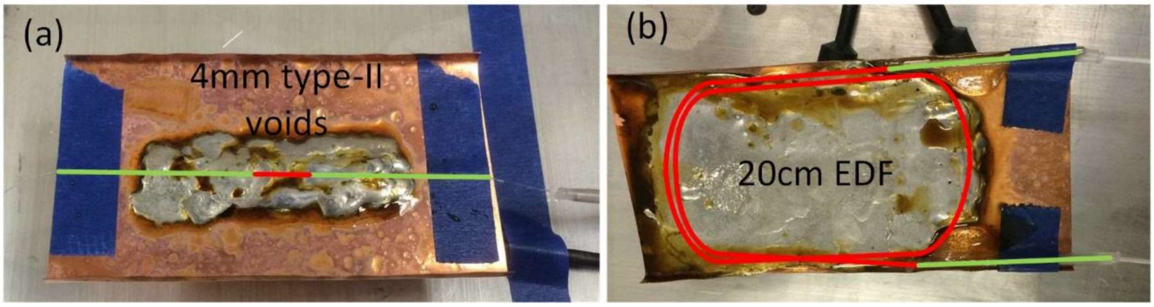

Figure 7-10. (a) AGU made with 4mm section of SMF-28e with scattering voids inscribed by a femtosecond laser; (b) AGU made with 40cm coiled EDF (Thorlabs ER80-8/125)

The photodetector monitoring results showed that the transmission loss for the scattering-based and EDF-based AGUs are 1.25dB and 6dB respectively, corresponding to absorption ratio of 25% and 75%. The acoustic signals generated by these two AGUs with the same 980nm laser pulses are shown in Figure 7-11. The repetition rate of the 980nm laser pulses was set to 90KHz.

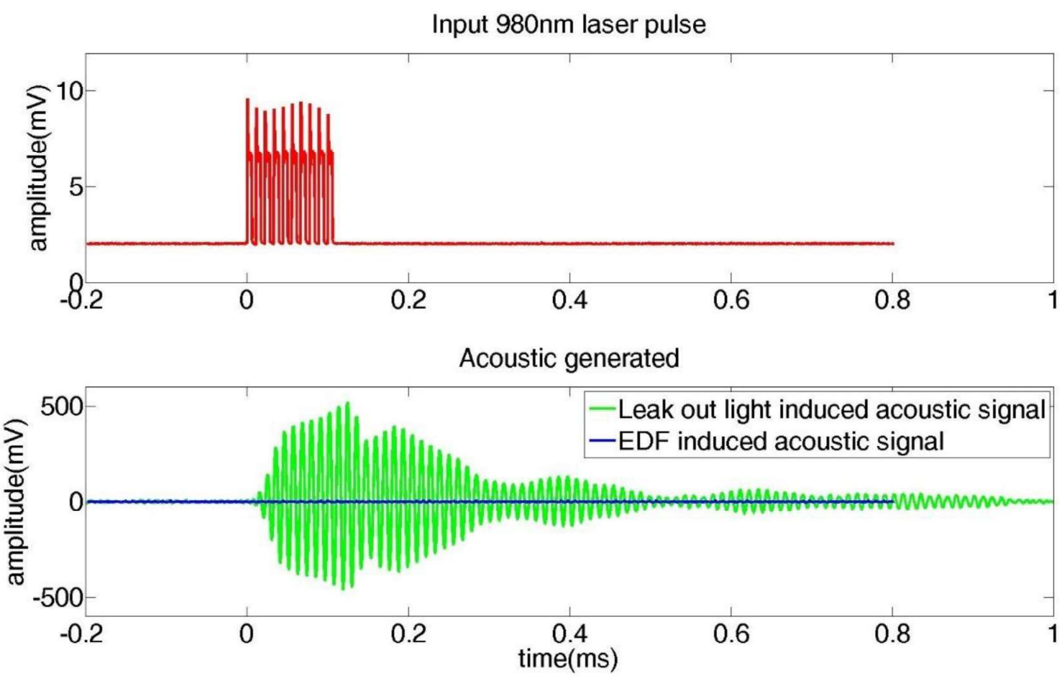

Figure 7-11. Acoustic signals generated by the scattering-based and EDF-based AGUs

The results clearly show that generating acoustic vibration with scattered light is superior in terms of opto-acoustic conversion coefficient compared to the EDF-based mechanism. The significant difference in the acoustic generation efficiency between the two methods is discussed in the following section.

7.3.3 Analysis of light-acoustic conversion efficiency

Let's consider an acoustic generation unit with cylindrical geometry and cross section diameter D_M. When it absorbs energy from a laser pulse, the material temperature arises. The temperature increment is:

$$\Delta T = \frac{\Delta Q}{m \cdot C_V} \qquad \Delta Q = \eta \cdot P \cdot t_0 \tag{18}$$

where P is the pulse peak power, t_0 is the duration of the pulse, η is absorption rate, C_V is the specific heat of the material, m is the mass of the unit and L is the length of the unit.

$$m = L \cdot \pi \cdot {D_M}^2 \cdot \rho \tag{19}$$

$$\Delta T = \frac{\eta \cdot P \cdot t_0}{\pi \cdot \rho \cdot L \cdot D^2{}_M \cdot C_V} \tag{20}$$

The corresponding strain is

$$\varepsilon = \Delta T \cdot \alpha \tag{21}$$

Here ρ is the density of the material and α is the linear thermal expansion coefficient.

The generated acoustic pressure is approximated by the tensile stress caused by this strain.

$$p = E \cdot \Delta T \cdot \alpha = E \cdot \alpha \cdot \frac{\eta \cdot P \cdot t_0}{\pi \cdot \rho \cdot D^2{}_M \cdot C_V \cdot L} = \frac{E \cdot \alpha}{\rho \cdot C_V} \cdot \frac{\eta \cdot P \cdot t_0}{\pi \cdot L \cdot D^2{}_M} = \frac{E \cdot \alpha}{\rho \cdot C_V} \cdot A \tag{22}$$

While the parameter $A = \frac{\eta \cdot P \cdot t_0}{\pi \cdot L \cdot D^2{}_M}$ is independent of the properties of the material, the acoustic pressure strength is mainly decided by four intrinsic coefficients of the material (Young's modulus, thermal expansion coefficient, density and specific heat). Comparing these properties of fused silica and tin as shown in Table 3, we can see that the acoustic strength will be about 65 times stronger if we switch the acoustic generating material from fused silica to tin.

Table 3. Material properties

	Fused silica	Metal tin

E	73 GPa	87 GPa
α	0.55 ppm/K	23.4 ppm/K
ρ	2.648 g/cm^3	7.28 g/cm^3
C_V	740 $J \cdot kg^{-1} \cdot K^{-1}$	210 $J \cdot kg^{-1} \cdot K^{-1}$
$\frac{E \cdot \alpha}{\rho \cdot C_V}$	2.05×10^{-2}	1.33

Since the fiber core is made of Erbium doped fused silica, this analysis suggests that directly illuminating metal with excitation light will generate a significantly stronger acoustic signal as compared to the EDF-based method.

7.4 Conclusion

Based on the analysis, the scattering based thermal expansion process was chosen as the acoustic generation mechanism in the FO-SHM element. The AGU designed based on this mechanism showed sufficient opto-acoustic generation efficiency and is mechanically strong. Due to the limitation of available optical fiber, we chose to use the two optical fiber scheme to build the FO-SHM element. This means that each FO-SHM monitoring elements will be formed with two fiber, one multimode fiber for acoustic excitation laser transmission, another single-mode fiber for the probe light transmission. Microstructures will be fabricated inside the multimode fiber for light scattering, and the FBG will be fabricated in the single mode fiber for acoustic detection. The acoustic wave will be generated from the surrounding adhesive by its absorption of the laser energy. The details of the FO-SHM design and the overall system design are presented in the following sections.

8 The design and fabrication of an all fiber optics structure health monitoring system

According to the information acquired in the previous phases, a detailed overall system design was presented in this phase.

8.1 System design and operation procedure

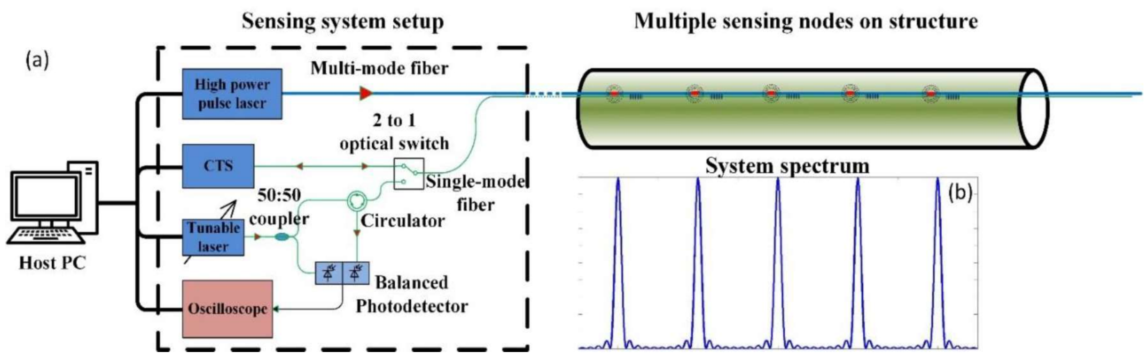

Figure 8-1 (a) System schematic of an FO-SHM system; (b) Sample spectrum of an FO-SHM system containing 5 nodes

The schematic of a multiplexed FO-SHM system is shown in Fig. 2. The acoustic detection fiber used was a Corning SMF-28e standard fiber, and the acoustic excitation fiber was a 105/125 µm step-index multimode fiber. The laser used for acoustic excitation was a flash lamp pumped 1064nm Nd:YAG free space laser with 10 Hz repetition rate and 50ns pulse width. The laser pulse energy was 150uJ. An optical sensing interrogator was used for fast spectrum acquisition, and for monitoring the spectra of all FBGs in the sensing chain as shown in Fig. 2(b). After obtaining the system spectrum, the spectrum location of the target FBG in the current cycle can be read. A C-band tunable laser was used as the probe light, the wavelength of which was tuned to the FWHM wavelength of the target FBG. A balanced photodetector was used to measure the fluctuation of the reflected optical power from the target FBG, which is related to the acoustic signal strength. A 50:50 fiber coupler was employed before the photo-detector to provide a reference arm, which eliminated the DC component in the measurement and allowed the detector to work at the highest possible gain. A high-speed oscilloscope with 2 GHz bandwidth was used to record the acoustic signal detected by the photo-detector. The system was switched between the FBG spectrum acquisition cycle and the acoustic signal acquisition cycle by a MEMS optical switch. The parameters of our interest can be monitored by the analysis of the obtained spectrum information and the acoustic signature. All the instruments in the system were controlled and synchronized by a PC through USB and Ethernet ports.

8.2 FO-SHM multi-parameter test procedure

We designed the following procedures to perform multi-parameter monitoring with an FO-SHM sensing element.

8.2.1 Temperature monitoring

The first step of the multi-parameter monitoring will be the determination of the sample temperature, because the measurement of other parameters will be affected by temperature. To monitor the temperature of the sample, we need to measure the acoustic velocity of a certain elastic mode. As illustrated in section 7.2.1, the distance between the acoustic generation/detection pair is designed to provide such an information. By setting this distance in the proper range based on the thickness of the sample, the peak representing the direct pressure wave in the AE can be separated from other bottom reflection peaks. Because the direct pressure is not affected by the thickness of the sample, under the non-guided wave assumption, the fly time of this peak can be a direct indication of the sample temperature. After the temperature is determined, this information will be used to calibrate the measurement of the other three parameters.

8.2.2 Strain monitoring

The monitoring of the strain is through the monitoring of the FBG spectrum peak shift. However, the FBG peak is also affected by temperature. The relationship between the peak shift and the sample temperature should be measured and recorded before an on-site application. In the actual multi-parameter application, this information together with the temperature determined in the first procedure can then be used to correct the FBG spectrum peak shift and produce an accurate measurement of the strain.

8.2.3 Crack and corrosion monitoring

The appearance of cracks can be monitored by actively scanning the AE for new peaks. The differential of the AE should be calculated continuously to reveal such changes. The corrosion can be monitored by measurement of the thickness change of the sample. This is possible by monitoring the peak locations of the bottom reflection waves. Like the strain measurement, the fly time of any bottom reflection peak is also affected by the sample temperature. So measuring and recording the relationship between the bottom reflection peak locations and the temperature is also essential.

8.3 **Experiment setup**

8.3.1 Pulse laser coupling system

In this research project, we used a free space Nd:YAG pulsed laser for the acoustic excitation due to its high energy/pulse capability. During the previous research phases where the experiment was only preliminary or confirmatory, a simple free space to fiber coupling setup was used. Basically, we used a long focal length lens to focus the pulsed laser into the multimode fiber. This setup showed problems like unstable coupling efficiency, difficulties in the alignment and damages to the fiber core during the alignment process. To solve this problem and reduce the alignment time for an everyday experiment, we designed and built the following coupling system.

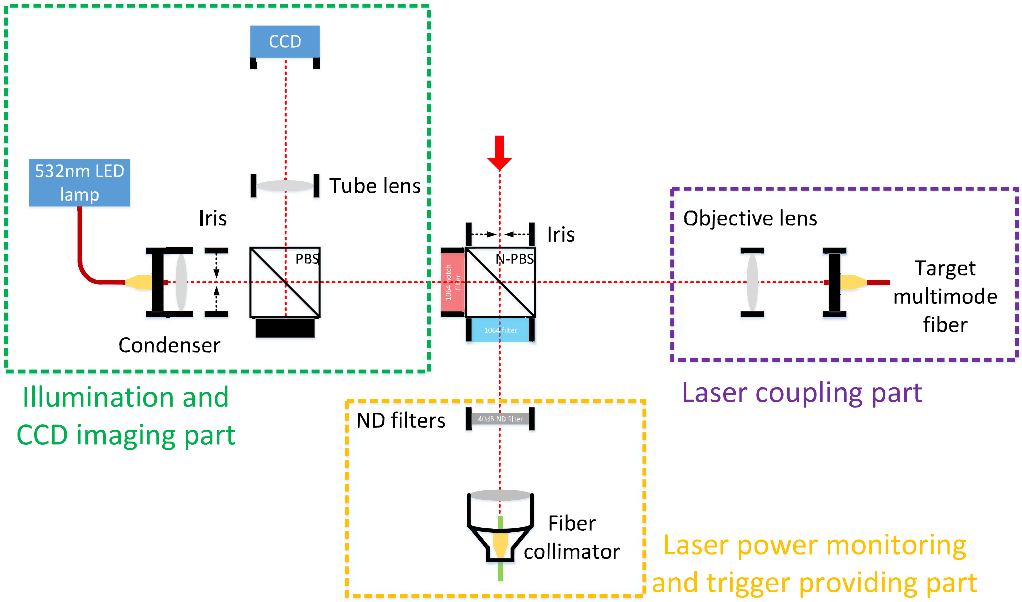

Figure 8-2 Simplified pulse laser optical fiber coupling scheme with CCD imaging system

Figure 8-2 shows a simplified schematic of the pulse laser to optical fiber coupling scheme This system is composed of a CCD imaging module, an illumination module and a laser power monitoring module. The imaging module provides the real-time image of the fiber coupling end surface and aids the alignment of the fiber core to the laser beam. The alignment procedures are as indicated in Figure 8-3(b). The fiber core is firstly moved far away from the laser beam and a single laser pulse is used to put a damage mark on the surrounding ferrule. Then a software provided cross hair is aligned with the damage mark to indicate the laser beam location. Finally, the core is aligned with the cross hair and the laser will be put to continuous working mode. The laser power monitoring module is connected to a photodetector by a single mode fiber. Besides monitoring the laser pulse intensity, it also provides a trigger signal for the sensing system. The completed coupling system is shown in Figure 8-3(a).

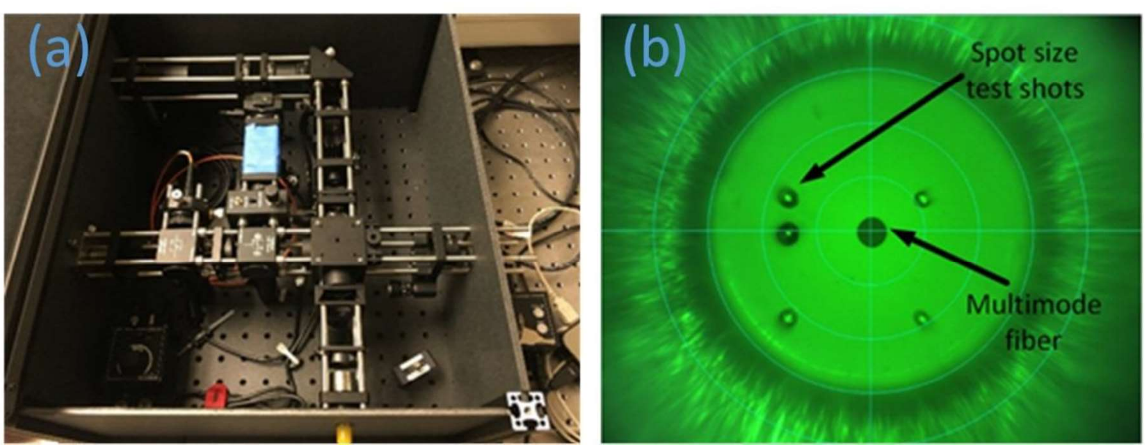

Figure 8-3 (a)Free-space laser to optical fiber coupling system; (b)Fiber core alignment method

8.3.2 Experimental setup

Figure 8-4 shows the preliminary experiment setup we used to demonstrate the feasibility of the multiplexed FO-SHM system. Despite the large size of the current system setup, it is possible to replace most of the equipment with smaller size substitutes and build the overall system in a portable enclosure.

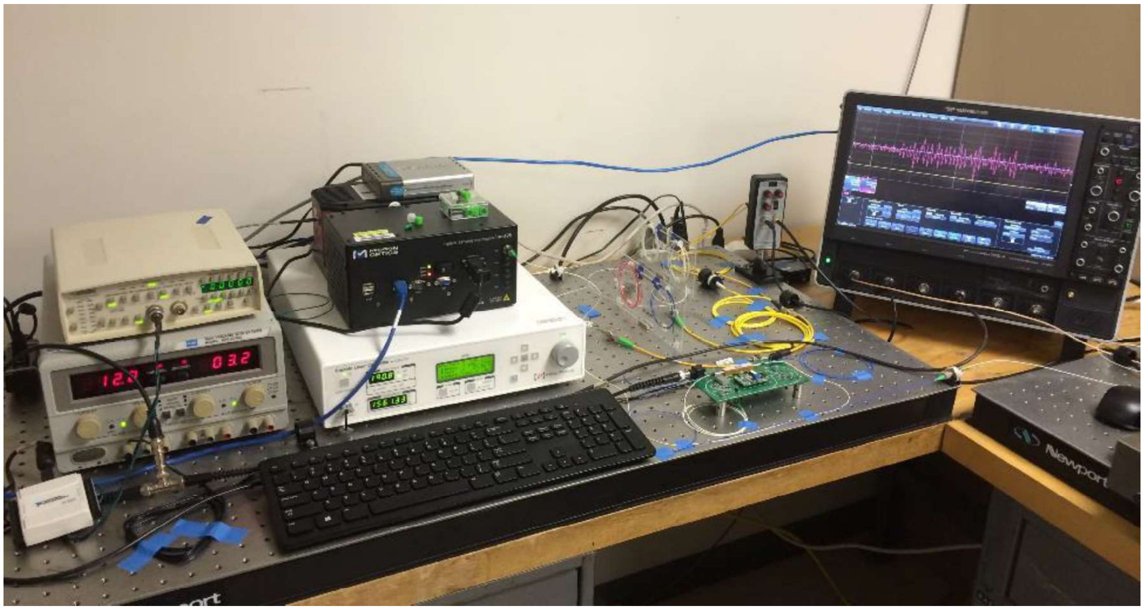

Figure 8-4 Preliminary experiment setup

8.3.3 FBG spectrum tracking system

As proposed in section 8.1, the FBG spectrum tracking functionality was added to the acoustic interrogation system. To achieve this functionality, a LabVIEW program was built to communicate with and control the equipment. Under the control of this program, the tunable laser wavelength is always tracking the FBG FWHM point when the environment temperature changes. This provides a consistent acoustic response sensitivity and thus ensures the signal stability. Figure 8-5 shows the FBG FWHM point tracing after the FBG point is touched by hand and experiences a rapid temperature rise and slow cool down process. The white line is the current FBG FWHM wavelength, and the red line is the current output wavelength from the tunable laser.

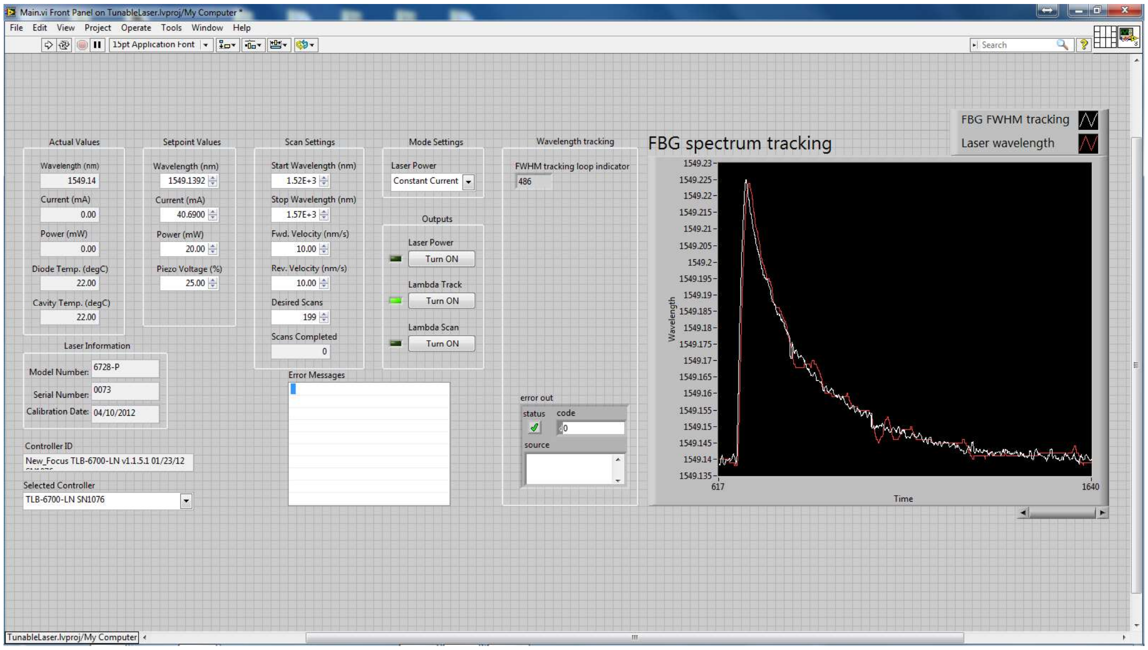

Figure 8-5 FBG tracking system LabVIEW control panel

9 Demonstration of the single-point FO-SHM multi-parameter monitoring in the low-temperature range

In this section, a demonstration of the multi-parameter monitoring capability and the system multiplexing capability was performed in the low-temperature range.

9.1 FO-SHM node installation and acoustic signature analysis

To demonstrate the multi-parameter monitoring capability of this FO-SHM system, a quarter-inch thick 7075 aluminum plate was used as the device under test (DUT). A single FO-SHM node was surface-attached to the aluminum plate as shown in Figure 9-1 (a). The FBG section was attached by an epoxy while the acoustic generation unit was attached with an epoxy-graphite mixture. The cured epoxy was semi-transparent and the added graphite helped increase laser absorption. The microstructure used in this acoustic generation unit was a special splicing point fabricated with a thermal fusion splicer as shown in Figure 9-1 (b). This structure can be easily fabricated by moving the two fiber ends to different heights while applying arc to splice them, and the light scattering ratio can be controlled by using different offset height. The light scattering ratio on this node was 40%.

To find the optimized location to mount the FO-SHM unit on the DUT, two sets of pre-installation tests were performed. In the first set of the pre-installation tests, an EFPI fiber sensor and direct laser illumination were used to generate and record the acoustic signal. Figure 9-1 (c) shows the schematic for this test. A multimode fiber transmitting the excitation laser pulses was positioned to directly illuminate the surface of the DUT and generate pulsed acoustic vibrations. The polished end of a single-mode fiber was placed near the reflective surface of the DUT, forming a Fabry-Perot interferometer (FPI) that monitors the normal displacement of the surface. With this setup, we were able to monitor the acoustic signature of the DUT while changing the locations of the acoustic excitation and detection. In these tests, the acoustic generation point and the acoustic detection point were placed about 20 mm to the nearest edge of the DUT, and the distance between themselves (source-receiver distance) was linearly increased. In the second test set, the FPI in the first test set was replaced with a surface attached FBG. The distance to the nearest edge was also 20 mm.

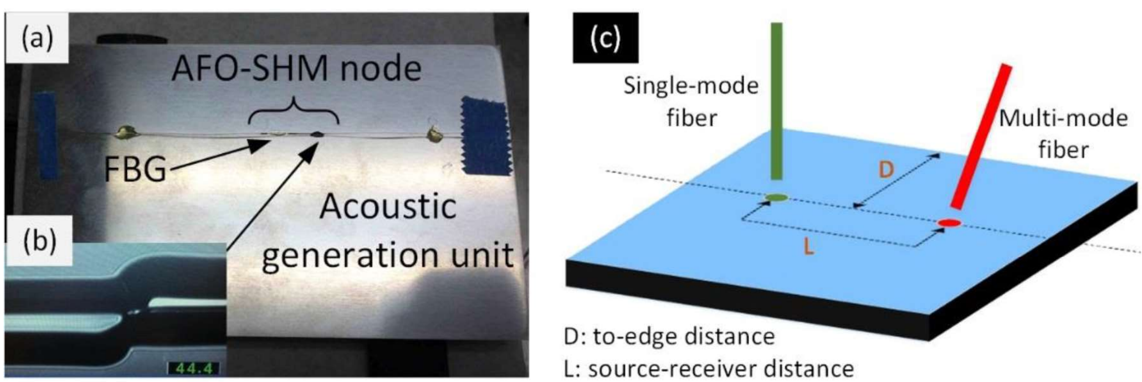

Figure 9-1 (a) FO-SHM node installed on the tested aluminum plate; (b) optical fiber special splicing structure; (c) pre-installation test with EFPI fiber sensor and direct laser illumination.

To better analyze the acoustic signatures obtained in these two sets of experiment, the acoustic velocities for different elastic modes are given in the following Table 4.

Table 4. Propagation speed of the elastic waves in 7075 aluminum

7075 aluminum elastic constants	Pressure wave speed	Shear wave speed	Surface Rayleigh wave speed
$\rho = 2.81\times10^{3} Kg/m^{3}$ $\lambda = 52.2GPa$ $\mu = 26.9GPa$	$V = \sqrt{\frac{\lambda+2\mu}{\rho}}$ $= 6142 m/s$	$V = \sqrt{\frac{\mu}{\rho}}$ $= 3094 m/s$	$2850 m/s$ [34]

The acoustic signatures obtained in these two test sets are shown in Figure 9-2(a) and Figure 9-2 (b) separately. The EFPI sensor only detects the normal surface displacement, making itself less sensitive to body waves directly come from the acoustic source because their particle movement directions are almost parallel to the surface. The FBG detects acoustic wave by its sensitivity to strain, thus is more sensitive to body waves compared to the EFPI sensor. Because of this difference, more peaks can be observed in the second set of acoustic signatures. In Figure 9-2 (a) and (b), three distinguishable peaks are found in the acoustic signatures. The locations of these peaks in the time domain are recorded by a peak finding algorithm and used in the following curve fitting formula (Eq. 23) to determine their propagation velocities and numbers of reflection experienced.

$$t = \frac{\sqrt{(2D)^2+(L+\Delta)^2}}{V} \tag{23}$$

In this equation, t is the peak location in time domain, L is the source-receiver distance, D is the distance from the source-receiver line to the presumed reflection surface, V is the velocity of a certain elastic mode, and Δ is a needed term mainly to compensate two possible errors: 1) the error in the recorded source-receiver distance; 2) the difference between the peak location in time domain and the actual travel time of the wavefront of a certain acoustic pulse.

Table 5. Curve fitting results of the three peaks and the expected values

	Curve fitting result			Expected value	
	$V(m/s)$	$D(mm)$	$\Delta(mm)$	$V(m/s)$ a	$D(mm)$ b
Direct R-wave	2894.7	0	1.33	2850	0
Reflected R-wave	2824.1	19.4	0.88	2850	20
Direct P-wave	6110.4	0	2.10	6142	0

[a]Data refer to Tab. 1; [b]Data from the actual experiment setup.

The results of the curve fitting are shown in Figure 9-2. By comparing the curve fitting results to the expected values, these three peaks are identified to be the directly propagating surface Rayleigh wave (referred to as direct R-wave), the side reflected surface Rayleigh wave (referred to as reflected R-wave), the directly propagating pressure wave (referred to as direct P-wave). An "In-direct wave zone" is marked in Figure 9-2 (a) because it is after the slowest direct wave (direct R-wave). Inside this zone, the area before the fastest possible side reflection wave (side reflected pressure wave) is marked as the "Bottom reflection zone" in Figure 9-2 (b).

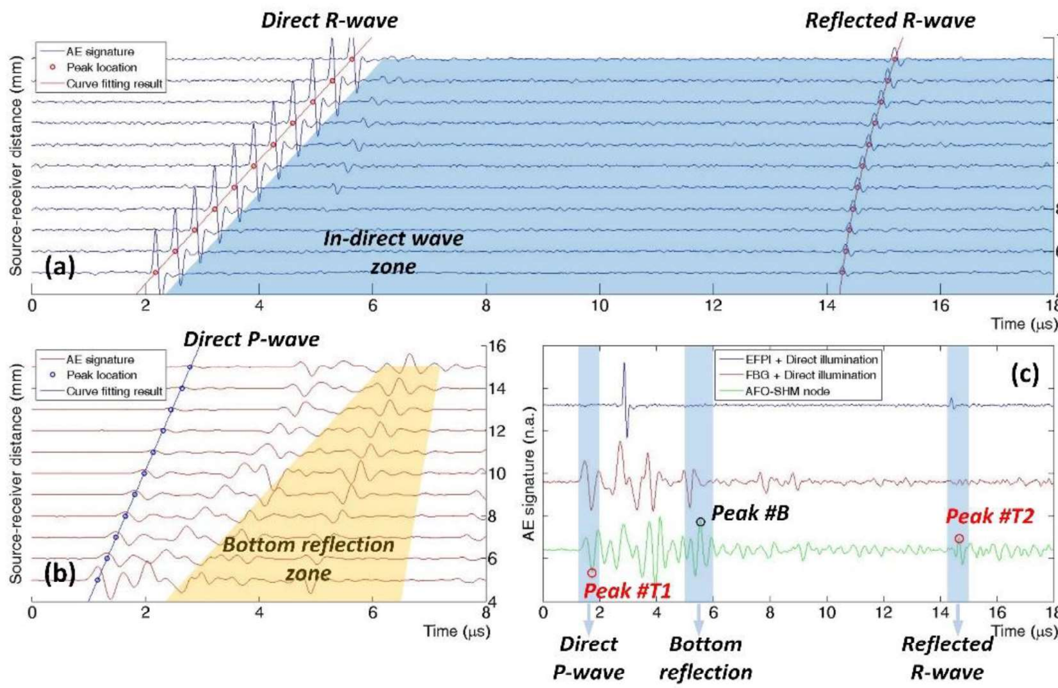

Figure 9-2 (a) Acoustic signatures obtained with EFPI sensor and direct laser surface illumination, the shift of each curve represents the source-receiver distance; (b) Acoustic signatures obtained with FBG sensor and direct laser surface illumination, the shift of each curve represents the source-receiver distance; (c) The final acoustic signature of the FO-SHM unit and its related acoustic signatures from the two pre-installation tests.

Based on the findings in the pre-installation tests, the final orientation of the FO-SHM unit on the DUT was set to be 20.5 mm away from the nearest edge and the source-receiver distance was chosen to be 7 mm to obtain sufficient separation between peaks. We found that the reflected R-wave was not very obvious in the second test possibly due to its overlapping with other multi-reflection body waves. By slightly changing the to-edge distance from 20 mm to 20.5 mm, this peak can be recognized in the final acoustic signature. The final FO-SHM acoustic signature was shown as the green curve in Figure 9-2 (c), the red curve and the violet curve are the data from the pre-installation tests with 7 mm source-receiver distance and 20 mm to-edge distance. In the following multi-parameter monitoring demonstration, the direct P-wave (referred to as #T1) and the reflected R-wave (referred to as #T2) will be used for temperature monitoring while the largest peak in the "Bottom reflection zone" (peak #B) will be used for thickness monitoring.

9.2 Multi-parameter monitoring demonstration of a single FO-SHM node

In this section, we present the monitoring of temperature, strain, thickness of the DUT and initiation of cracks on the 6.35 mm thick aluminum plate.

9.2.1 Strain monitoring

To apply strain on the sample, the sample was placed on a mechanical vice and the compression force was exerted by the jaws of the vice along the fiber direction as shown in Figure 9-3. A dial indicator was used to record the relative displacement of the two jaws. We assume that the deformation of the steel vice jaws was small due to its much higher stiffness compared to the thin aluminum plate, so this relative displacement is equal to the compression of the aluminum sample. The ratio of this compression over the total length of the sample was calculated and used as an approximated reference for the strain. The relationship between the calculated strain and the FBG peak shift is showed in Figure 9-4.

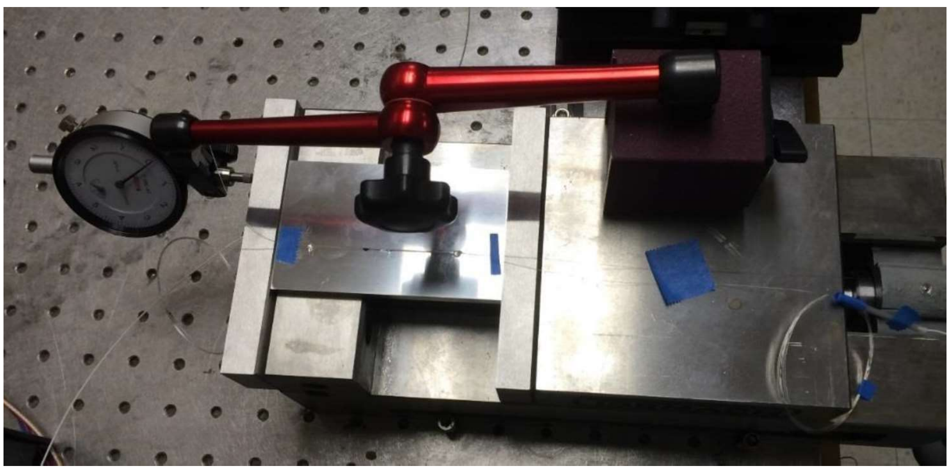

Figure 9-3 Strain test setup

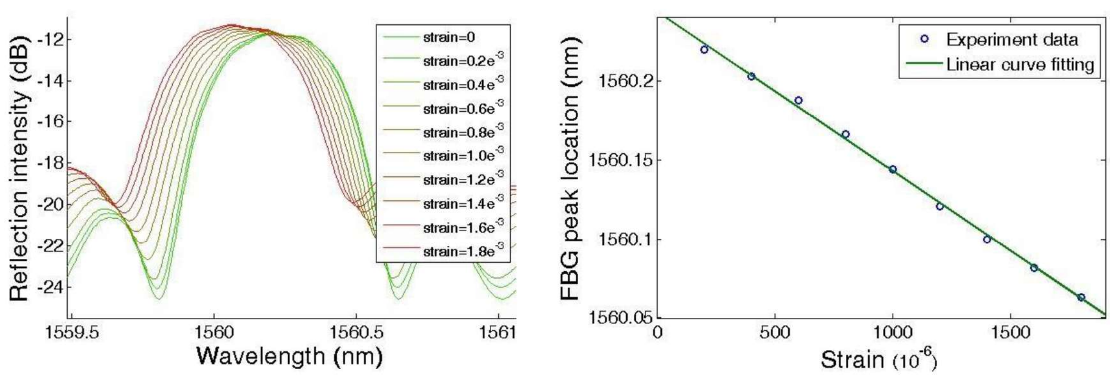

Figure 9-4 (a) FBG spectrum monitoring during the strain change process; (b) FBG peak location shifts caused by the strain changes.

A linear curve fitting of the FBG peak location data gives a strain sensitivity at 0.101 nm/millistrain. The following Eq. (24) shows the theoretical relationship between the FBG peak location shift and the applied strain along the fiber axis[35]. λ_B is the FBG peak wavelength which is around 1560 nm in our experiment, n is the effective refractive index of the optical fiber which is about 1.4682 at 1550nm for the Corning SMF-28e we used, ν is the Poisson's ratio which is 0.17 for silica, p_{11} and p_{12} are the components in the strain-optic tensor which are 0.1 and 0.285 respectively for silica[36].

$$\frac{\Delta\lambda_B}{\varepsilon} = \lambda_B\left(1 - \frac{n^2}{2}[p_{12} - \nu(p_{12} + p_{11})]\right) \tag{24}$$

This calculation yields a theoretical strain sensitivity of about 1.2 nm/millistrain. The difference between this theoretical value and the linear curve fitting result can be used to calculate the strain transfer ratio from the host material to the FBG, which is around 0.101/1.2=8.4%. In the prior research[37], the strain transfer ratio was found to be increasing with the increase of the adhesive length and to ranging from 56% to 82% for adhesive length from 5 cm to 15 cm. Considering that the adhesive length is only 3.5 mm in our experiment, we believe 8.4% strain transfer ratio is reasonable.

9.2.2 Thickness monitoring

During the thickness monitoring demonstration, the sample was milled off by about 10% of the initial thickness from the bottom by 4 incremental steps. The machining process is illustrated in Figure 9-5.

Figure 9-5 Milling off sample bottom to simulate the corrosion

The acoustic signatures obtained at these thicknesses are shown in Figure 9-6. We can see that the temperature indication peak #T1 and #T2 did not shift during the thickness changing process. This is because that these two peaks are acoustic waves traveling along the surface and have no interaction with the bottom of the sample. The thickness indication peak #B, shifted almost linearly during the thickness changes. The total travel length for peak #B can be calculated by

$\sqrt{(L^2 + (2N \times t)^2)}$, where L is the source-receiver distance, t is the thickness of the sample and N is an integer representing how many rounds the wave gets reflected before it reaches the receiver. When the relative change of the thickness is small, the travel length difference may be approximately governed by Eq. (25), which explains the linear relationship between the peak shift and the thickness change.

$$\Delta\sqrt{(L^2 + (2N \times t)^2)} \approx 2N \times (L^2 + (2N \times t)^2)^{-1/2} \times \Delta t \tag{25}$$

(3)

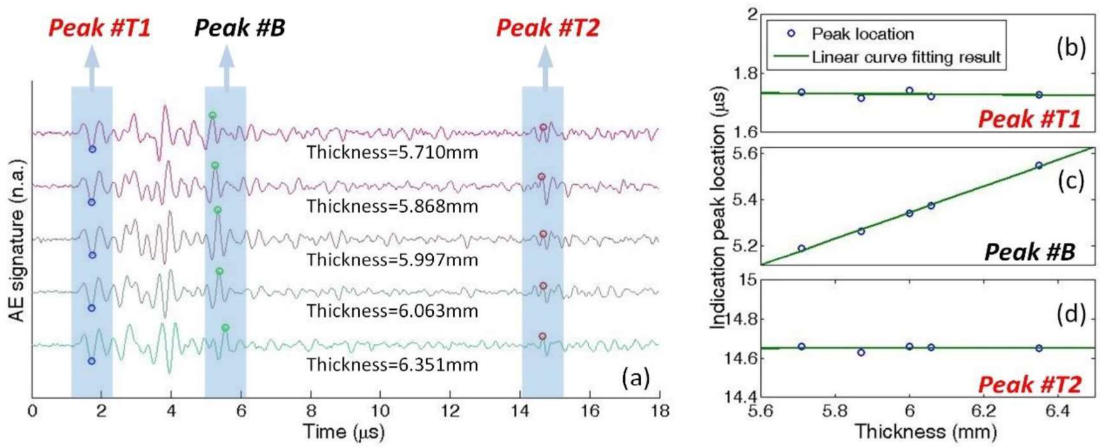

Figure 9-6 (a) Acoustic signatures in the thickness monitoring test; (b) peak #T1 center shift; (c) peak #B center shift; (d) peak #T2 center shift.

9.2.3 Temperature monitoring

In the temperature monitoring demonstration, the sample was placed inside a temperature control furnace while the temperature was raised step by step and was stabilized for about 1 hour at each step before a measurement was taken. Figure 9-7 shows the time domain shifts of the three signature peaks due to the temperature induced acoustic velocity changes. The linear curve fittings give the peak shift versus temperature response rates for these monitored peaks. Using these rates and the temporal locations of these peaks, the acoustic velocity change rates can also be calculated. The results are presented in Table 6.

Table 6. Peak location associated response rates to temperature change

Peak	#T1	#B	#T2
Peak shift over temperature (ns/°C)	2.26	3.52	5.34
Acoustic velocity change percentage over temperature (10^{-3} /°C)	1.31	0.63	0.36

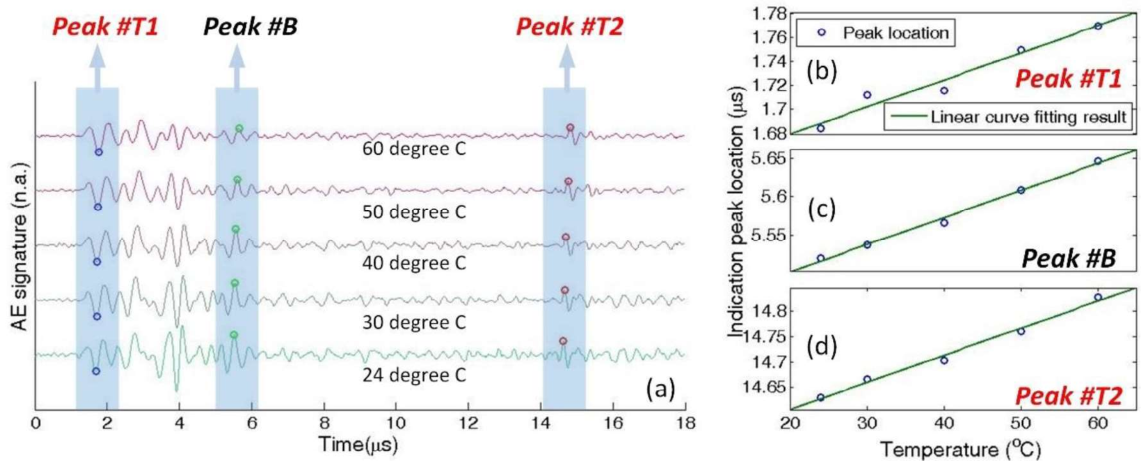

Figure 9-7 (a) Acoustic signatures in the temperature monitoring test; (b) peak #T1 center shift; (c) peak #B center shift; (d) peak #T2 center shift.

The FBG spectra were also recorded during the temperature changing process and are shown in Figure 9-8 (a). The FBG peak locations are shown in Figure 9-8 (b) and a linear curve fitting shows that its response rate to temperature change is about 13.4 pm/°C in this temperature range.

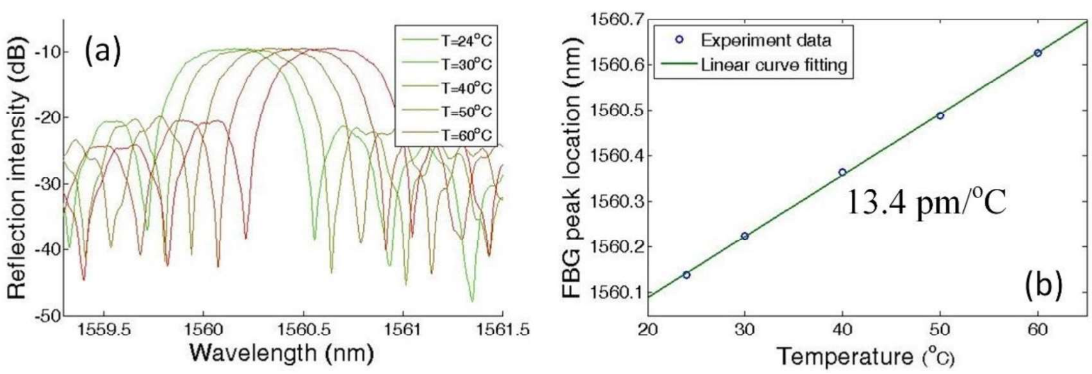

Figure 9-8 (a) FBG spectrum monitoring during the temperature change process; (b) FBG peak location shifts caused by the temperature changes.

9.2.4 Crack detection

To demonstrate the capability of the system to actively detect a crack, a slot with about 1 mm width, 3 mm depth, and 1cm length was machined on the sample 1cm away from the FO-SHM node as shown in Figure 9-9 (a). The acoustic signature evolution is shown in Figure 9-9 (b). Comparing the acoustic signature with/without the crack, it can be seen that several new peaks were generated from the reflections of the crack. In ultrasonic flaw detection, the generally accepted lower limit of detection for a small flaw is one-half wavelength. Because of the short laser pulse width (50 ns) used in the system, the generated acoustic pulse width is in the sub-millimeter range. Therefore, we believe this method should be responsive to cracks with sizes in the millimeter range and above.

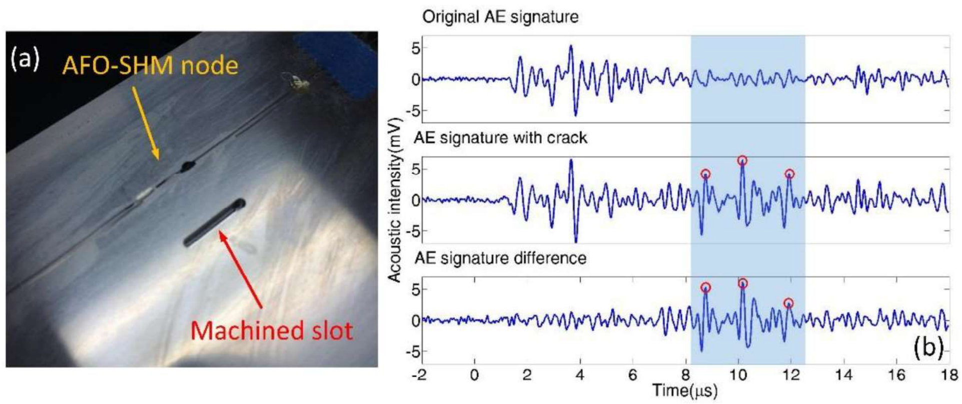

Figure 9-9 (a) FO-SHM sample with a machined slot on it; (b) Comparison of the original acoustic signature and acoustic signature with a machined slot on the sample.

Besides the active crack detection as shown above, this system is also sensitive enough to do passive detection, i.e., detect the shock wave associated with the sudden formation of a large crack. This was demonstrated by an industry standard pencil lead break (PLB) test. Figure 9-10 shows the PLB test signal. The yellow line shows a recorded PLB signal with the excitation point 2cm away from the FO-SHM element. And the red line shows a recorded PLB signal with the excitation point 6cm away from the FO-SHM element. This can be useful when we deploy this system in a field test in the phase II of this project and want to maximize the possibility of crack detection.

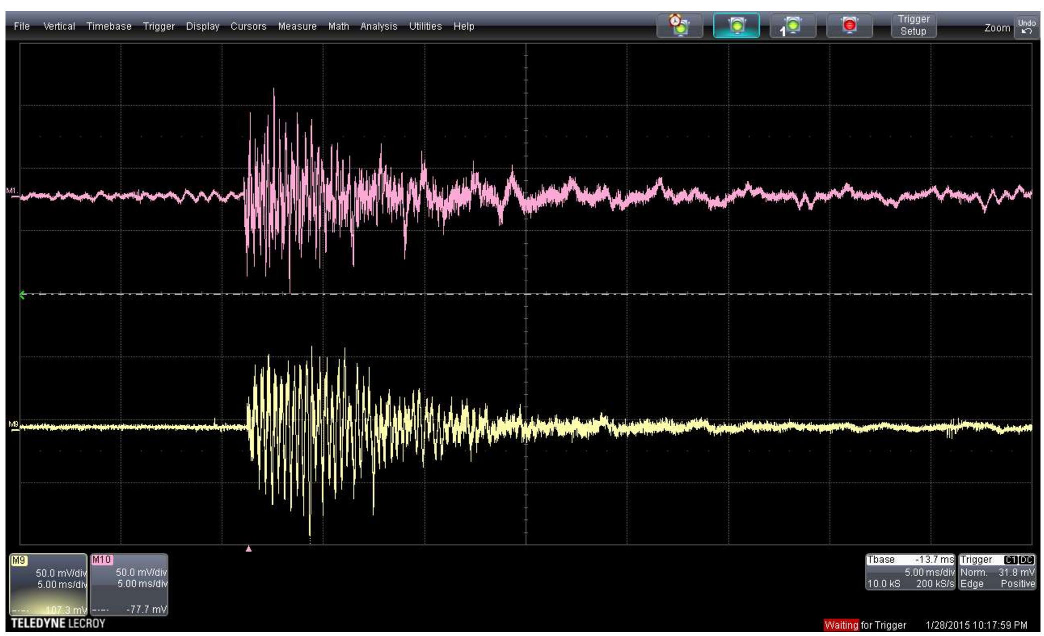

Figure 9-10 PLB test result with the FO-SHM element

To summarize, we have demonstrated the FBG spectrum change and acoustic signature variation for applied strain on the sample, applied temperature change, thickness change and crack. For temperature monitoring, peak #T1 and peak #T2 in the acoustic signature will be used because their peak locations are not affected by the thickness change. Peak #B will be used for thickness monitoring and its temperature induced shift should always be compensated by the shifts of peak #T1 and #T2 according to their temperature response rates. As for strain monitoring, the FBG peak shift will be used after its temperature induced shift being compensated using the current temperature value and its temperature response rate acquired in section 9.2.3. In future practical applications for real time crack detection, the differential of the acoustic signature should be updated continuously to reveal the appearance of crack-related new peaks.

9.3 Demonstration for multiplexed FO-SHM monitoring

This section presents a demonstration of the multiplexing capability of the FO-SHM system. The design of a multiplexed FO-SHM system has been shown in Figure 8-1 previously.

9.3.1 Multiplexed FO-SHM sample preparation

To achieve uniform acoustic excitation at all sections, the scattering light intensity at each section should be the same. In a cascaded multi-point acoustic generation fiber chain, this means that the scattering loss ratio increases at each section. We used femtosecond laser inscribed type-II voids as the structure to introduce scattering light and the loss ratio can be monitored and controlled during the fabrication process. Figure 9-11 shows the type-II voids inscribed with different laser intensity. Red light was transmitted in these fiber to show the scattering light intensity during the fabrication process. As we can see, the voids on the left which are inscribed with lower laser intensity introduce less light scattering compared to the other ones on the right which are inscribed with higher laser intensity.

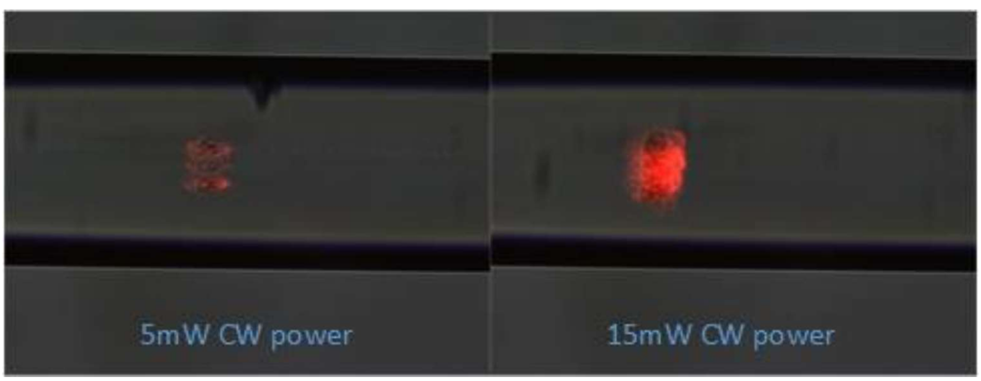

Figure 9-11 Type-II voids for acoustic generation

Figure 9-12 shows an FO-SHM network testing unit constructed with two FO-SHM nodes. The length of the optical fibers connecting these two nodes was about 1 meter. Node #1 was attached to the the ¼” thick aluminum piece with a simulated crack, with an FBG wavelength of 1560 nm. Sample #2 had a similar geometry to sample #1 but had no crack on it, and its FBG wavelength was around 1530 nm. Table 7 shows the key properties related to acoustic generation and acoustic detection of each section.

Table 7 Properties of each section

Section	#1	#2
Center wavelength	1530nm	1560nm

Light loss	30%	50%
Relative acoustic intensity	30%	(1-30%)x50%=35%

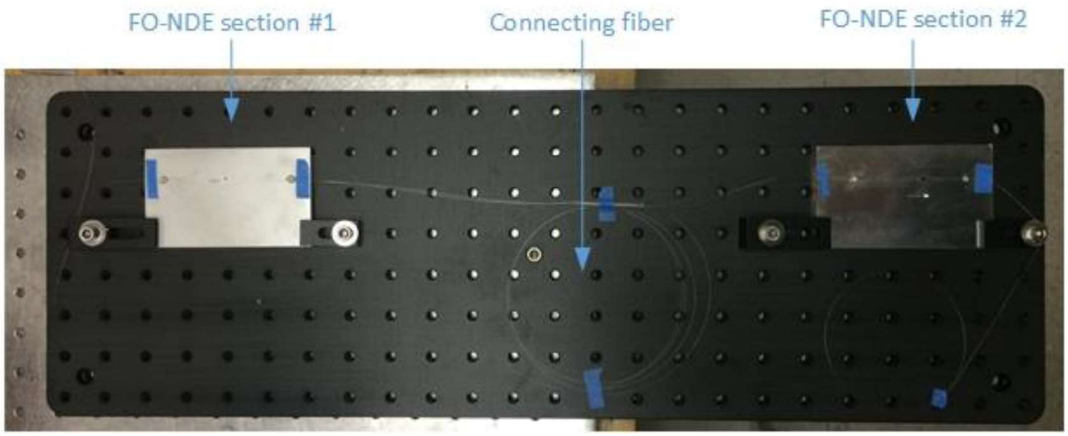

Figure 9-12 Sample for multiplexed FO-SHM system demonstration

We can see from the testing result shown in Figure 9-13 that the acoustic intensity is at the same level, which agrees with our expectation. The messier acoustic signature in section 2 was caused by the crack fabricated on the #2 aluminum sheet.

9.3.2 Multiplexed system controlling software and test result

Figure 3 shows the controlling software built for the multiplexed FO-SHM system. The cell in the top left indicates the number of the current section under monitoring and the related FBG FWHM wavelength. The bottom left cell indicates the working state of the system. The center cell shows the spectrum of all sections and the wavelength tracking of the current section. The cell on the right shows the latest updated acoustic signature of all monitored sections.

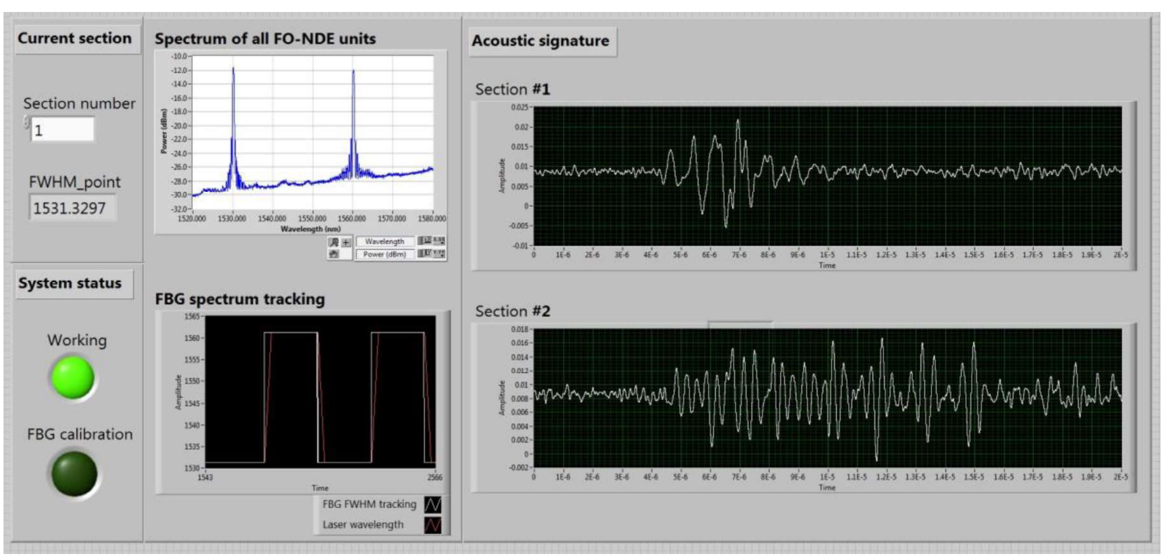

Figure 9-13 LabVIEW controlling software for the multiplexed FO-SHM system

9.4 Conclusion

In conclusion, a multiplexable all-fiber-optics structure health monitoring system was presented in this phase. In the demonstration of this system, the temperature, strain, thickness changes of an aluminum sample were quantitatively associated with the FBG spectrum shift and the peak shifts in its acoustic signature. The occurrence of an artificial crack was related to the appearance of new peaks in the acoustic signature. The multiplexing capability was also preliminarily demonstrated by the acquisition of spectrum information and acoustic signatures from an FO-SHM network containing two cascaded nodes. Despite that the concept of FO-SHM has been brought up for several years, to our best knowledge, this is the first experimental realization and demonstration of such a system.

The demonstrated temperature range is from 24ºC to 60ºC, which is the allowed working temperature of the epoxy used in the FO-SHM node. By changing the epoxy to a high temperature adhesive such as a ceramic adhesive, this system is expected to be able to reach much higher temperatures.

10 High temperature FO-SHM element surface embedment design, simulation, and test

The work done in this phase serve as preparations for the final demonstration in a harsh environment. The preliminary high temperature tests and simulation were focused on the final demonstration material – P91 pipes. Several different surface attachment methods and adhesives were tested and analyzed towards improving the high temperature survivability. Type-II FBG was also fabricated and tested in this phase.

10.1 Numerical simulation of thermal stress on surface attached FO-SHM sensor

Since our next major step in this project is high temperature test, it is important to build a simulation model to assess high temperature related problems, such as the CTE mismatch induced thermal stress. The software package we used is COMSOL multi-physics thermal stress module. This module consists of two sub-modules which are heat transfer module and solid mechanics module. These two sub-modules are one way coupled by thermal expansion effect. Based on the size of the T91 tube currently available, a model with 1.25" outer diameter and 0.75" inner diameter was built. The thickness of the ceramic adhesive was set to be 1 mm and the optical fiber was placed 0.5mm away from the tube surface.

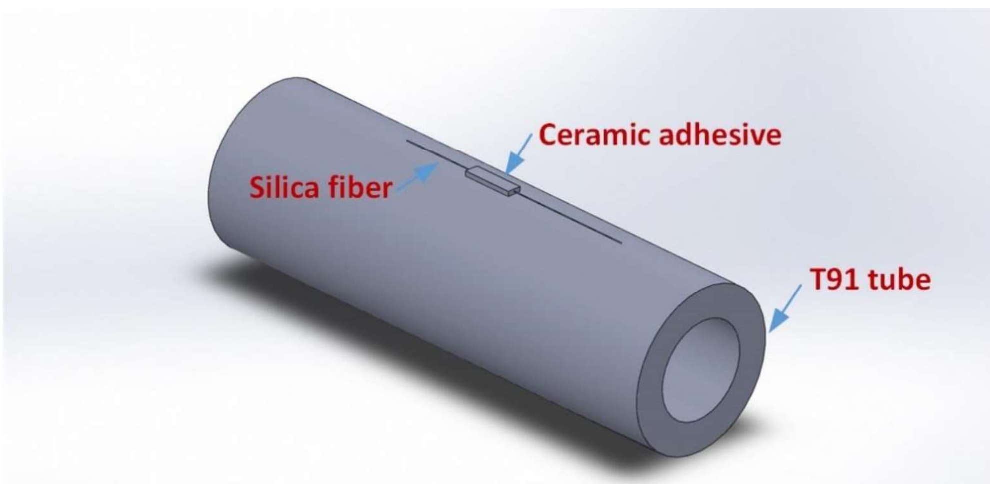

Figure 10-1. Simulation model.

Due to the size difference between the tube, adhesive, and silica fiber, each section was meshed differently to ensure accurate result while saving calculation time. As shown in Figure 10-2, the tube has the roughest mesh size. The mesh on the adhesive is finer, which gives it 5 layers of mesh. The silica fiber has the finest mesh which is 4 mesh per cross section.

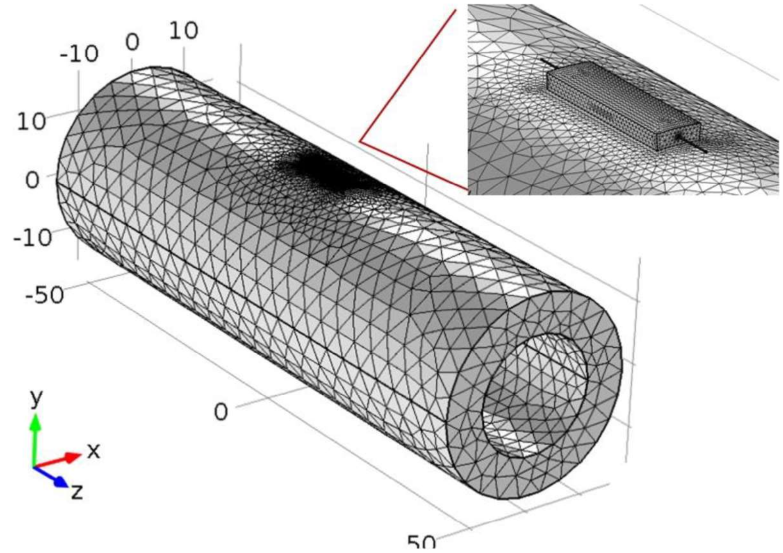

Figure 10-2. Mesh for FEM analysis.

The material properties used during the simulation are listed in Table 8. The values for silica and steel come from the COMSOL material library and the values for ceramic adhesive come from the adhesive manufacture.

Table 8 Material properties for thermal stress simulation

Material Contents		Ceramic	Steel	Silica
Property	Name	Value	Value	Value
Coefficient of thermal expansion	alpha	8.1e-6[1/K]	12.3e-6[1/K]	0.55e-6[1/K]
Young's modulus	E	390e9[Pa]	200e9[Pa]	73.1e9[Pa]
Poisson's ratio	nu	0.26	0.33	0.17

The T91 pipe is able to work continuously up to about 650 ºC, and this is set as the working temperature in the simulation. Figure 10-3 shows the simulation result in the form of Von-Mises stress. Von-Mises stress is widely used as a criterion to decide whether or not a material will fail. If the maximum value of Von-Mises stress on a piece of material is smaller than the yield strength of this material, it will not deform, or vice versa. As shown in Figure 10-3, most of the stress is concentrated around the adhesive. The majority part of the tube body has zero stress because its thermal expansion is not constrained in the model.

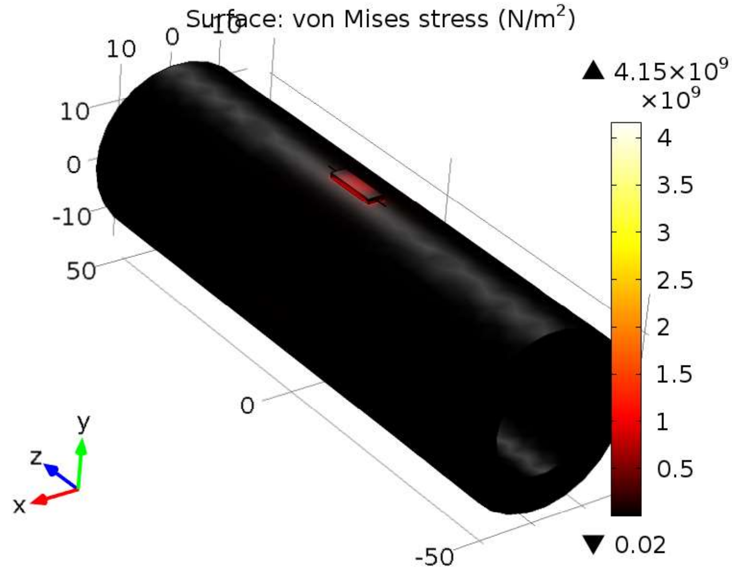

Figure 10-3. Von-Mises stress of the whole model.

The stress and strain distributions in different sections are shown in Figure 10-4. Figure 10-4 (a) shows that the highest stress is located around the corner, suggesting that sharp corners and edges should be avoided in the sample fabrication. And the highest Von-Mises stress (1720 MPa) is higher than the yield strength of T91 (415 MPa). Figure 10-4 (b) shows the strain along the fiber axis instead of stress, with the highest value of 6.55 $m\varepsilon$ at the center of the fiber. It is known that standard silica fiber has a yield strain about 1% [38], so the fiber breakage may not be our main concern. Figure 10-4 (c,d) shows that the highest Von-Mises stress is located around the corner at the value of 4050 MPa, which is much higher than its yield strength (20 MPa). This also suggests that sharp corners should be avoided in real sample preparation. Based on these values, in a high temperature environment, the most vulnerable part of this surface attached sensor will be the ceramic adhesive due to its low yield strength. This suggests that other alternative adhesive materials be searched for substitution.

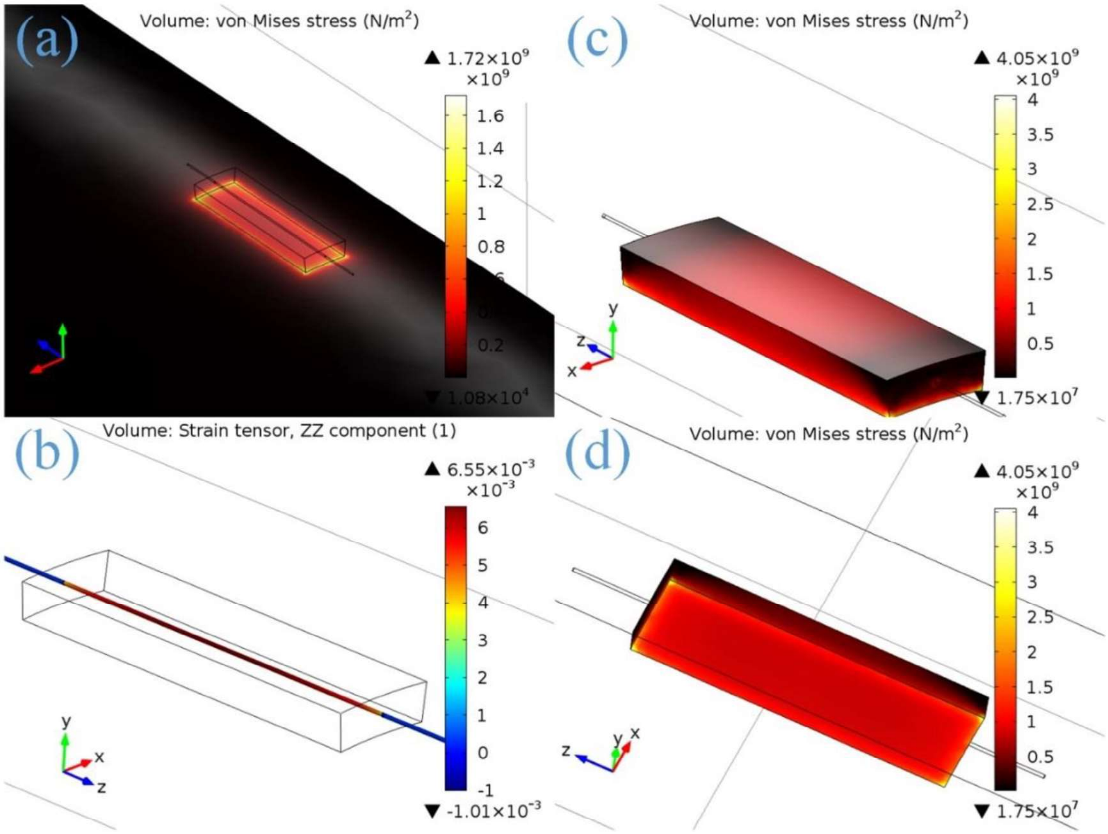

Figure 10-4. (a) Von-Mises stress on the tube; (b) Strain along the fiber axis; (c) Top view of Von-Mises stress distribution on the adhesive; (d) Bottom view of Von-Mises stress distribution on the adhesive.

10.2 High temperature test of a surface attached FO-SHM element (ceramic adhesive)

In this phase, we prepared a P-91 sample with an FO-SHM element attached on the surface by a high temperature ceramic adhesive. We are familiar with this adhesive and know that it can reach a temperature over 1000°C so it became the first candidate we tested for high temperature FO-SHM element attachment.

10.2.1 Fabrication of a ceramic adhesive attached FO-SHM sample

The FO-SHM element was surfaced attached to a T91 tube with the high temperature ceramic adhesive purchased from COTRONICS CORP. The surface was polished with 400 grit sandpaper prior to applying the adhesive for stronger bonding. The width of the applied adhesive was around 1.5mm and the length was about 5mm. The adhesive was firstly at the room temperature for 4 hours before the final curing at 65° C. Before heated up to high temperature, the lead-in/out fiber was secured by blue tapes on the surface. The FBG used in this FO-SHM element is a -3dB type-I grating, due to the lack of type-II FBG fabrication capability at that time.

Figure 10-5. FO-SHM element surface attached to a P91 pipe by high temperature ceramic adhesive.

10.2.2 High temperature test result and analysis

In this test, the P-91 sample was heated inside a high temperature furnace. The first procedure was to fully cure the adhesive, which is to maintain the furnace temperature at 65ºC for two hours. After this procedure, the furnace was stabled at 100ºC, 200ºC and 300ºC each for 2 hours. This ensured that the sample temperature is consistent with the furnace temperature setting. The FO-SHM signal was recorded at these four temperature points by the LabVIEW controlling software introduced in section 9.3.2. At 300ºC, we noticed that the FBG spectrum was distorted, so we stopped this high temperature test to inspect potential fiber breakage. The FO-SHM element looked intact by visual observation after cooled to room temperature as can be seen from Figure 10-6. The adhesive bonding was relatively strong, but the FBG adhesive section could be intentionally pulled off from the pipe. The adhesive was then carefully observed under the microscope and several cracks were found as shown in Figure 10-7. As the crack may induce irregular strain distribution around the FBG section, this can be one of the causes for the FBG spectrum distortion.

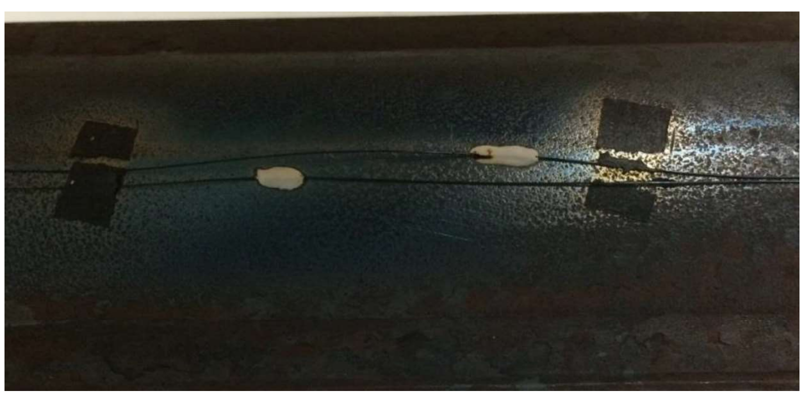

Figure 10-6 Surface attached FO-SHM element after the high temperature test

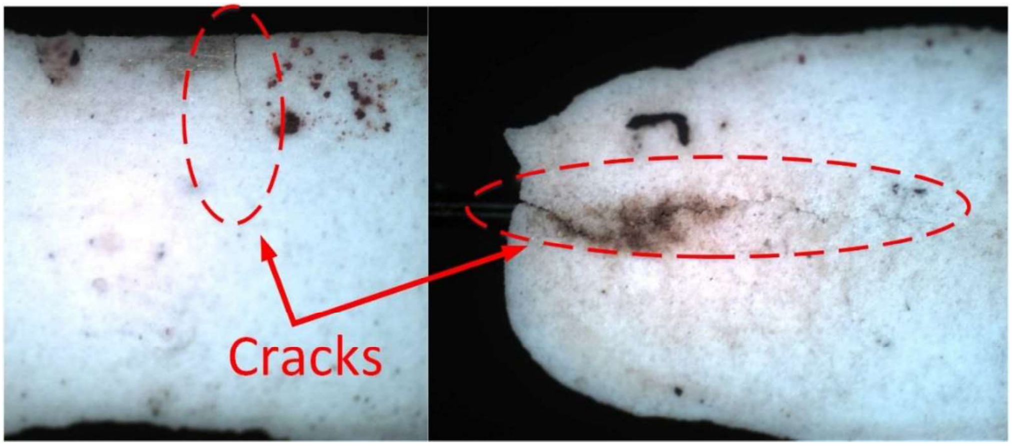

Figure 10-7 Ceramic adhesive after heating up to 300° C

As shown in Figure 10-8, the AE changes at different temperature points, which should be caused by the temperature dependence of the elastic wave speed. Besides that, the signal strength is not stable when the temperature changes. This unexpected phenomenon is related to the irregular shape change of the FBG spectrum, which was observed during the heating up procedure.

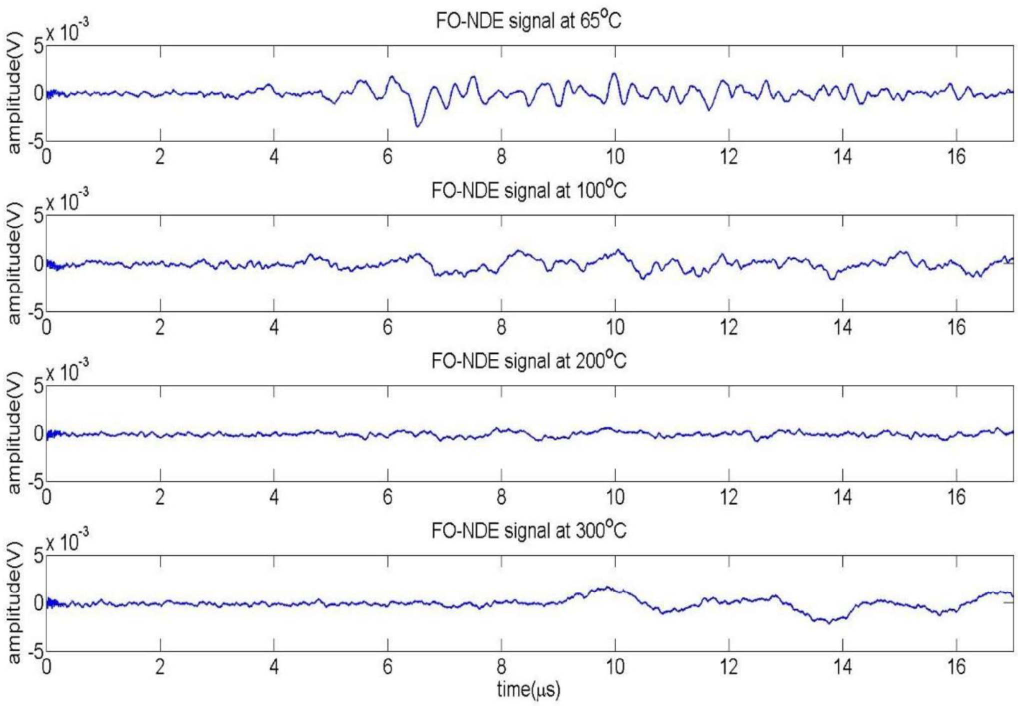

Figure 10-8 Signal of the surface attached FO-SHM element at different temperature points

To further study the causes of the FBG distortion in a high temperature environment, a second test was performed on the same P91 pipe, but with only the FBG section attached. The test followed a similar procedure as the first test, with the temperature range extending to 650° C.

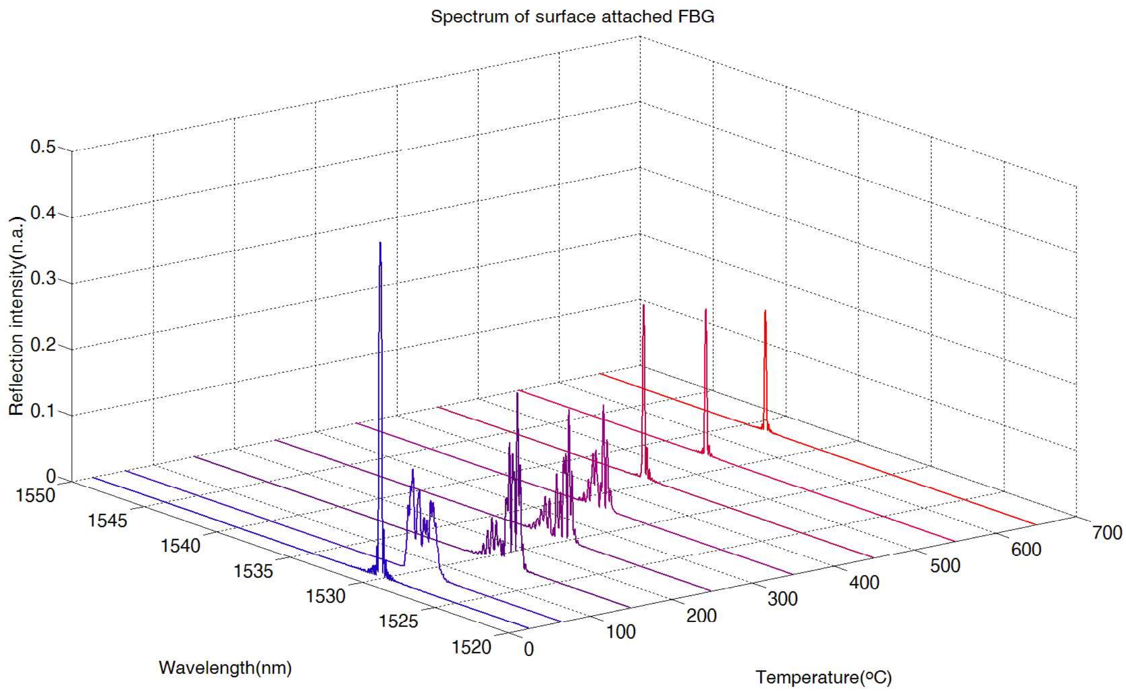

Figure 10-9 FBG spectrum during the second high temperature test

As we can see in Figure 10-9, the FBG spectrum experienced an irregular distortion/broadening at a temperature lower than 350° C and returned to normal shape after the temperature passing 400° C. Besides that, the reflection peak intensity dropped as the temperature steadily increased. The second phenomenon was a known effect when a type-I FBG is used at high temperature. This issue is mainly due to dopant diffusion and strain relaxation, and should be avoided in our final demonstration by replacing the type-I FBG with type-II FBG. As for the irregular FBG spectrum distortion, possible cracks as shown in Figure 10-7 can be one cause. Another major cause should be the non-uniform strain distribution induced by thermal stress, this will be illustrated by the following simulation results.

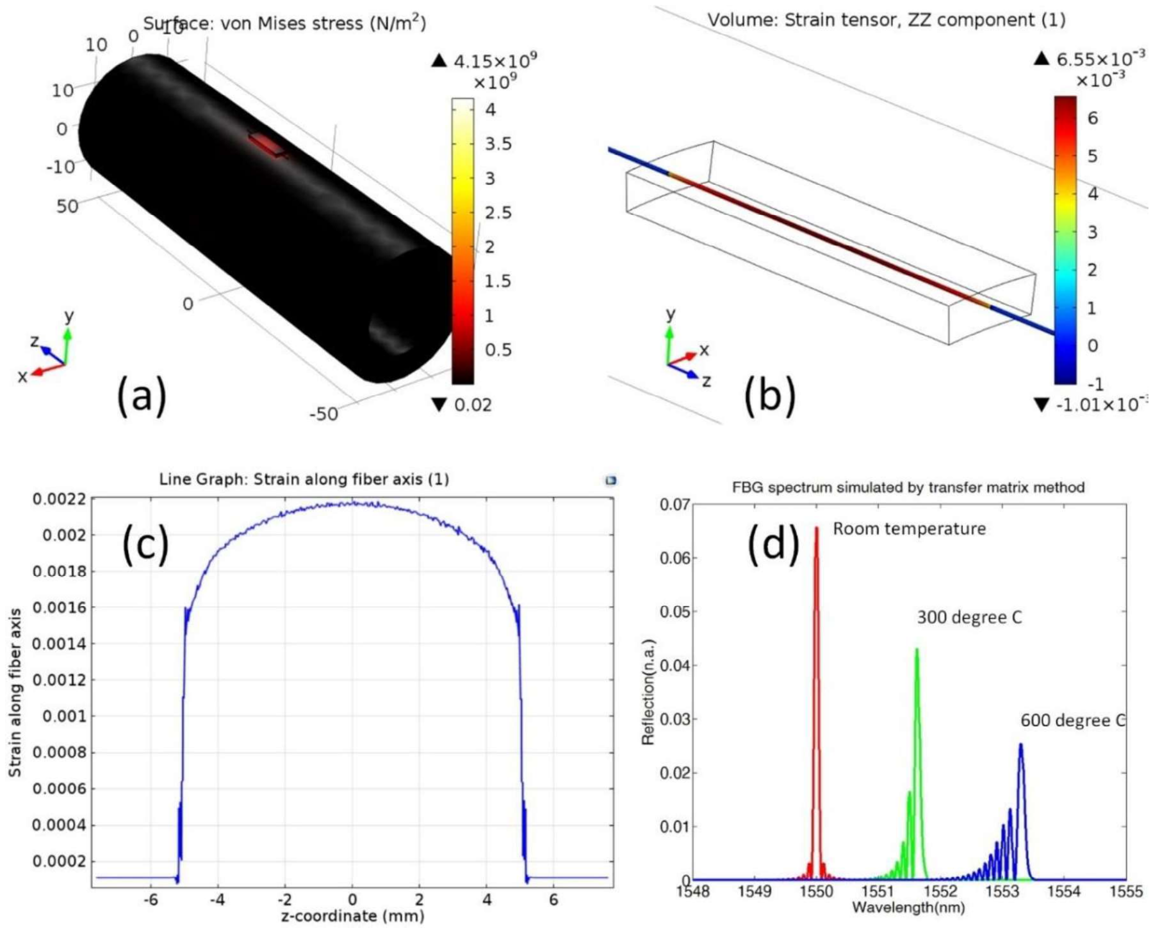

Figure 10-10 (a) Simulation model with surface attached FBG heated to 600º C; (b,c) Non-uniform strain distribution along the silica fiber; (d) Simulation result of FBG spectrum with non-uniform strain.

The same COMSOL simulation model shown in the previous section was used, however, the focus was put on the strain distribution on the fiber instead of the highest von Mises stress. As shown in Figure 10-10 (b, c), after heated to high temperature, the strain on the fiber shows a non-uniform distribution. This non-uniform distribution is caused by the edge of the adhesive, which should transform to a flatter distribution if the adhesive is much longer than the FBG inside it. FBG with these strain distributions at different temperature points were then simulated with transfer matrix method to give the predicted spectrums as shown in Figure 10-10 (d). Comparing the experimental results in Figure 10-9 and simulation results in Figure 10-10 (d), it can be seen that the first several spectrums in the experiment agree with the simulation results pretty well in terms of shape broadening/distortion. However, the experimental spectrum recovered its normal shape after 400º C. This may be caused by the release of the holding force between the ceramic adhesive and the silica fiber. Because the thermal expansion coefficient of the ceramic adhesive ($8.1e^{-6}$ (1/K)) is larger than the CTE of silica ($0.55e^{-6}$ (1/K)), the thermal mismatch may cause the bonding to be loose at a higher temperature, thus weakening the non-uniformity of the strain distribution on the silica fiber.

Based on these experimental findings and simulation predictions, we proposed and tested a surface embedment design, intended to solve the cracking issues and achieve a more stable FBG spectrum during high temperature environment.

10.3 High temperature test of a surface embedded FO-SHM element (ceramic adhesive)

In this phase, we tested a surface embedment design to mount the FO-SHM element on a P-91 sample. In this design, the whole optical fiber was buried into a pre-cut slot on the pipe by the same ceramic adhesive used in the previous section. Based on the simulation results from the previous section, the high temperature thermal strain should be uniform along the FBG because the adhesive length is much longer than the FBG length. In addition, we hope this can also avoid crack formation in the adhesive.

10.3.1 Surface embedment design and thermal stress analysis

As shown in Figure 10-11, a thin slot with about 1mm radius will be cut on the surface of the workpiece. The optical fiber holding the FO-SHM element will be placed in the slot and sealed with ceramic adhesive. To eliminate shape edges and irregular thermal stress distribution, overfilled adhesive will be scraped off and the finished surface of the adhesive will be flat and smooth.

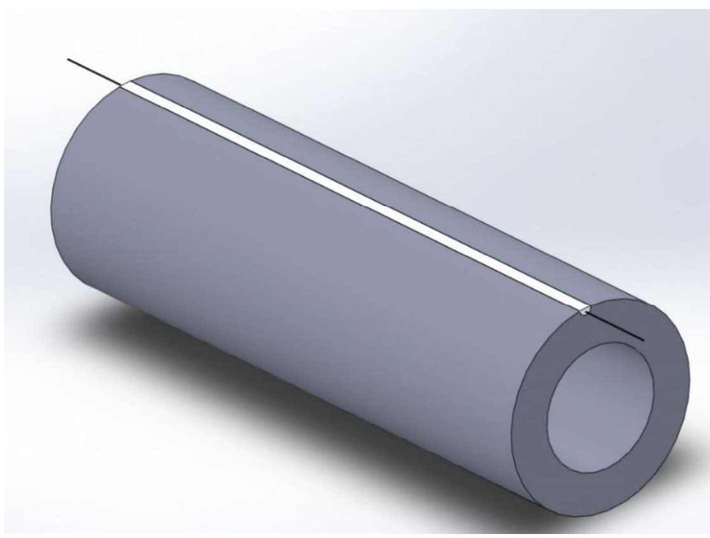

Figure 10-11 New schematic of FO-SHM element embedment

The simulation results acquired with COMSOL are shown in Figure 10-12. As our intuition predicts, the strain distribution on the center part of the fiber (where the FBG is at) is basically flat, which means that the FBG spectrum distortion/ broadening will be minimized as the temperature rise.

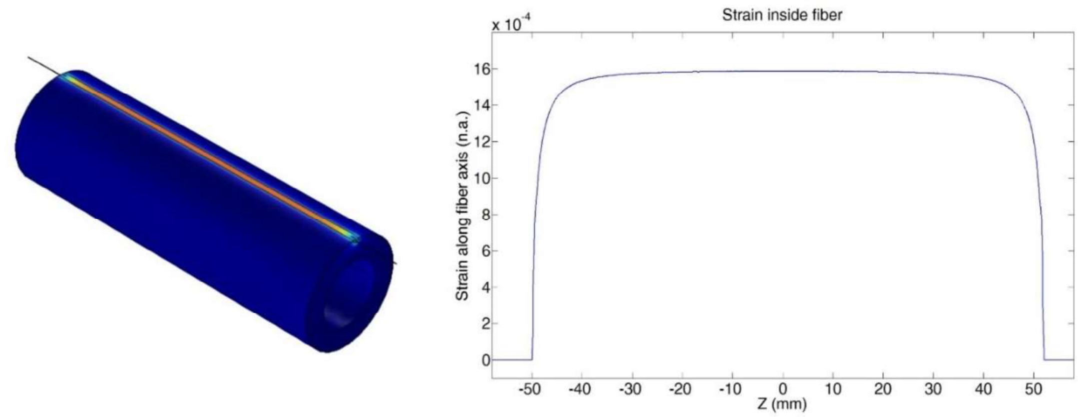

Figure 10-12 COMSOL simulation result of thermal strain distribution at 200° C

10.3.2 High temperature test result and analysis

Figure 10-13 Full embedment sample preparation and new large volume tube furnace used in the test

Figure 10-13 shows the fabrication process of a P91 testing sample containing a full embedded FBG fiber link. A shallow 90 degree V groove was cutting on the P91 pipe with a square end mill as shown in Figure 10-13 (A). The depth of the V-groove was about 0.5mm. Then the optical fiber containing the FBG section was placed inside the V-groove and sealed by ceramic adhesive as shown in Figure 10-13 (B). The adhesive was then cured at room temperature for 4 hours following the instruction of the adhesive manufacturer. After this step, the adhesive became solid and the excessive amount of adhesive which stuck out of the V-groove was polished off by sand paper. Figure 10-13 (C) shows the sample after polishing. This testing sample was then placed inside a new large volume tube furnace as shown in Figure 10-13 (D). The heating procedure started with 2 hours at 150 ºC which served as the final curing process for the ceramic adhesive. Then the temperature was raised to 200 ºC and idled for few hours. The initial plan was to idle at each temperature points for 4 hours until the temperature reaches 800 ºC. However, we found that the FBG fiber link broke inside the ceramic adhesive after 2 hours at 200 ºC so the experiment was stopped at this temperature. After the sample was cooled down and taken out of the furnace, there was no visible damage on the adhesive.

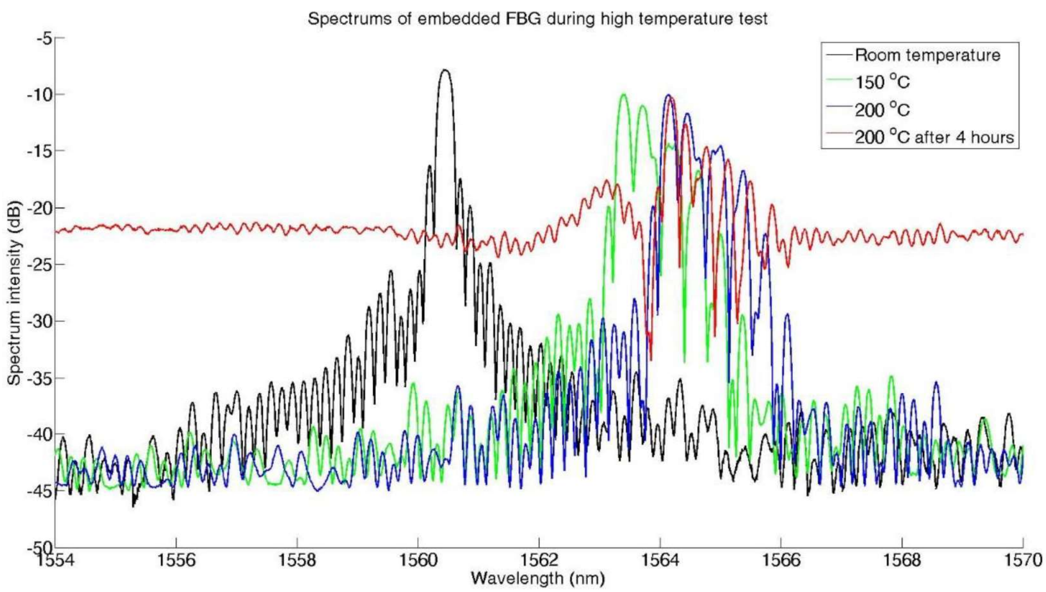

Figure 10-14 FBG spectrums during the temperature changing process

Figure 10-14 shows the changes of the FBG spectrum during the heating process. The black curve is the spectrum after 4 hours room temperature curing of the adhesive. It can be seen that the spectrum is in its normal shape without irregular distortion. This indicates that there is no non-uniform strain distribution on the FBG section. The green curve is the spectrum after the 2 hours final curing at 150 ºC. The spectrum position shifted mainly due to the temperature change and the thermal strain. The shape of the spectrum was also distorted which suggests that the strain distribution along the FBG section became non-uniform. In the last quarter, the simulation suggested that when the buried length of the optical fiber is much longer than the length of the FBG, the thermal strain should be evenly distributed through the FBG section. The disagreement between the simulation result and this experiment result can be caused by two reasons. Firstly, the cured ceramic adhesive was not perfectly isotropic. Secondly, a not perfectly controlled polishing process generated a non-uniform cross section shape of the adhesive around the FBG section. At the time that the temperature just reached 200 ºC, the FBG spectrum (blue curve) shifted but remained similar shape to the spectrum at 150 ºC. However, after about 2 hours at this temperature, the lower boundary of the spectrum (red curve) suddenly jumped up from -45 dB to -22 dB which indicates a breakage in the fiber link.

Comparing the experimental results from the previous section to this experiment, it becomes clear that in the high temperature range, the strain breakage threshold of a bare optical fiber drops to about 0.2%. This value is calculated by setting the temperature to 200 ºC in the COMSOL model we used in the last quarter and it also agrees with the experience of other researchers in our lab. The reason that the FBG survived a high temperature test up to 650 ºC in the last quarter is because of the point attachment plan. Because the length of the adhesive was comparable to the length of FBG, when heated to high temperature the FBG could slide inside the ceramic adhesive so the strain on the fiber was lower than the predicted value given by the simulation.

10.4 Low CTE metallic adhesive based FO-SHM sample high temperature test

Based on the results acquired from the previous phase, we did more market search and found one high temperature metallic adhesive with lower CTE compared to what we previously used. During our tests, we found this adhesive providing stronger bound to both the P91 pipe and the silica fiber. In this section, we present the AE analysis with FO-SHM element attached on a P91 pipe by this new adhesive and its high temperature test results. Relatively short length of adhesive was used for the surface attachment of the FO-SHM element.

10.4.1 Low CTE adhesive based FO-SHM element design

Based on the previous two sets of experiment, we proposed a new embedment plan featuring short section attachment, stainless tube protection and low CTE metallic adhesive. Firstly, two pieces of small diameter stainless tube are surface attached to a P91 pipe by high temperature adhesive. These two tubes are placed in-line with each other and separated by a distance slightly larger than the length of the FBG section. The two optical fiber containing the FBG and the acoustic generation structure will be placed inside the stainless protection tubes. The FBG section will be aligned in the gap between the two tubes and the acoustic generation unit will be certain distance from the FBG (hidden in one of the tubes). Finally, a low CTE metallic adhesive (CTE=$4e^{-6}$ /K) will be applied to both the FBG section and the surface area of the tube section covering the acoustic generation unit. The structure is illustrated in Figure 10-15.

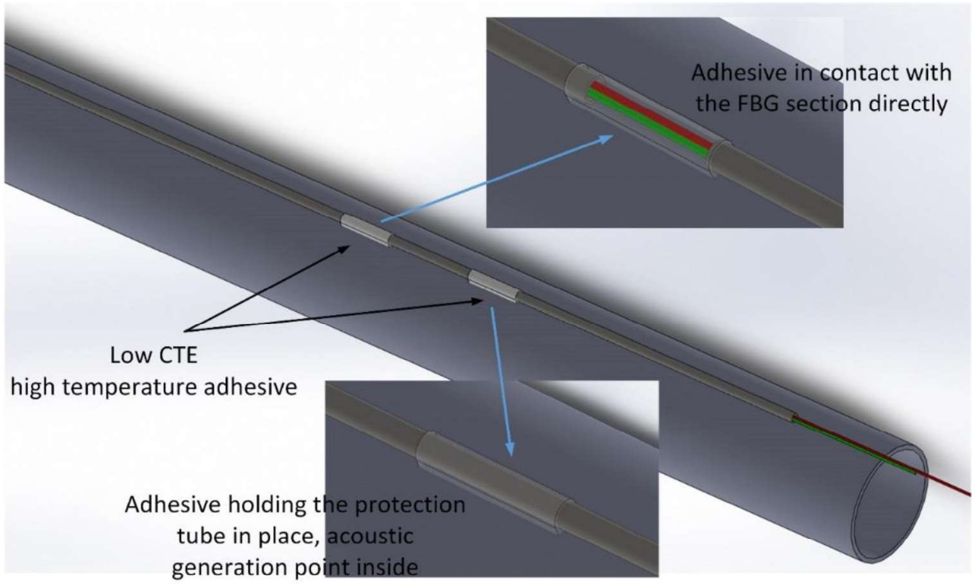

Figure 10-15 New FO-SHM embedment plan

10.4.2 FO-SHM fabrication and AE signature observation on P-91 pipe

A P91 pipe with 28.8mm OD and 5mm wall thickness was used in the following test sets. Firstly the AE signature was obtained using the EFPI sensor and laser direct illumination method. Figure 10-16 shows two different test conditions. In the first case, the EFPI fiber and the acoustic excitation fiber were placed at the same angle on the pipe, i.e., a line connecting these two points will be parallel to the axis of the pipe. In the second case, the acoustic excitation fiber was placed to a different angle as the EFPI fiber remained in the same location.

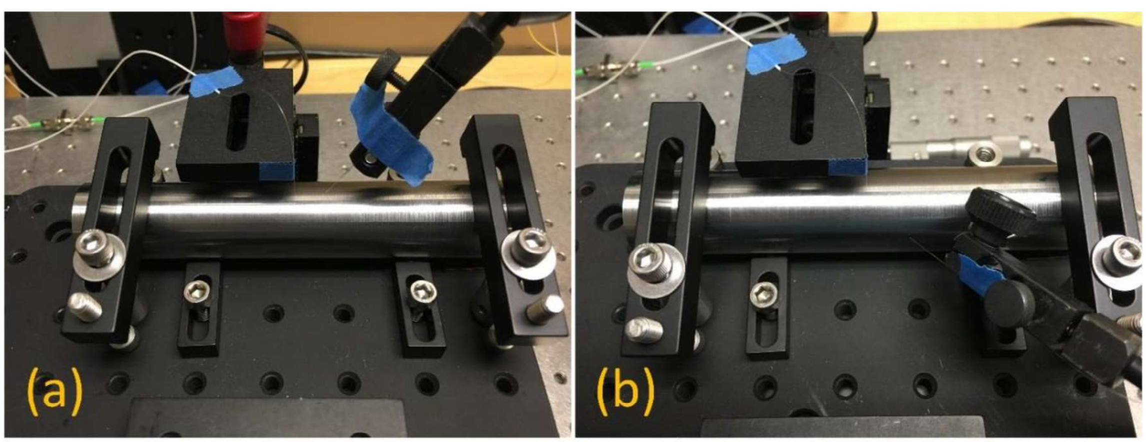

Figure 10-16 Experiment setup for AE signature acquisition on a P91 pipe with EFPI sensor and direct laser illumination acoustic generation

From Figure 10-17, we can see that the direct surface waves contribute to the most obvious peaks in the AE signatures. This agrees with the experimental results discussed in the previous section. The 1st order direct surface wave travels directly from the excitation point to the detection. The 2nd order direct surface waves travel an additional round on the pipes from two directions. In case (a), the additional paths for the two directions were the same so the two 2nd order waves combined into a larger peak. In case (2), since the excitation point was placed at a different angle compared to the detection point, the symmetry was broken and the additional paths for the two directions differed. As a result, two individual peaks can be observed in the AE signature.

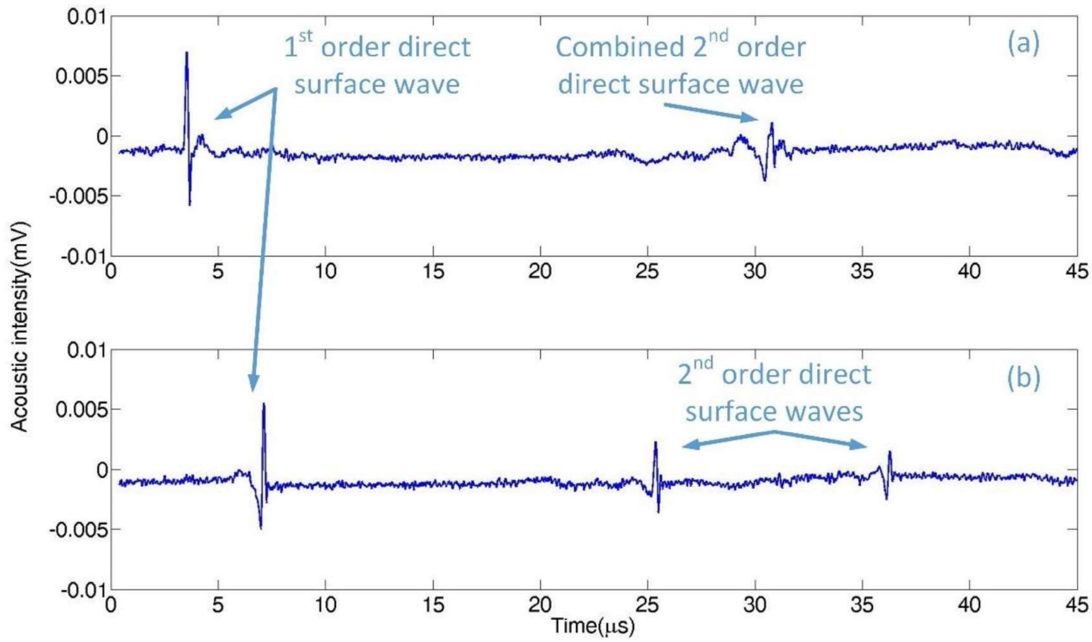

Figure 10-17 AE signatures acquired in the first test set

The second test set was done by attaching FBG on the P91 pipe with the newly received low CTE high temperature metallic adhesive. A stainless tube was also used for fiber protection as designed in the last quarter. Figure 10-18 (a) shows the materials and equipment for making such adhesive. Figure 10-18 (b) shows the experiment setup for acquiring AE signature on the P91 pipe with surface attached FBG and direct laser illumination acoustic generation. In this test set, the laser illumination point was placed at the same angle as the FBG on the P91 pipe, and the distance between these two points was adjusted.

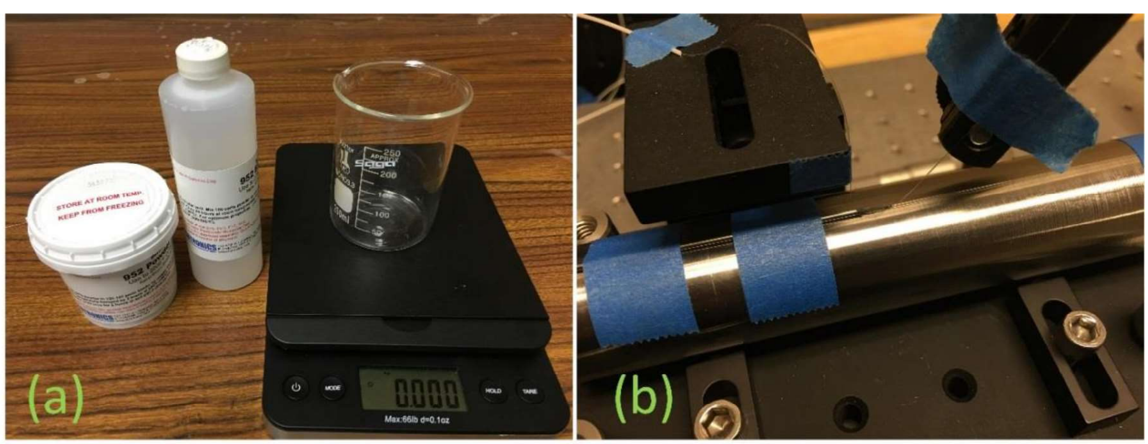

Figure 10-18 Fabrication process and experiment setup for FBG + direct illumination FO-SHM sample

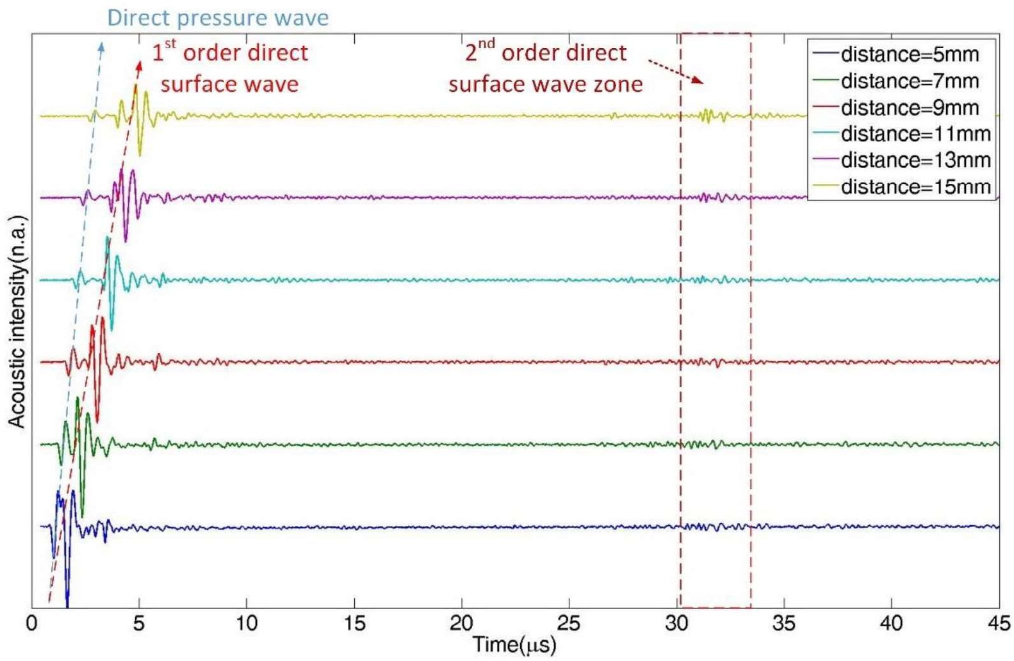

Figure 10-19 AE signatures at different distance between excitation point and detection point

From Figure 10-19, we can see that by replacing the EFPI sensor with FBG, more peaks including the direct pressure wave, direct shear wave and bottom reflected waves were presented in the AE signatures (direct shear wave and bottom reflection not marked). Also, since the acoustic excitation point and the acoustic detection point were at the same angle on the pipe, the 2nd order direct surface waves were combined. To get cleaner 2nd order surface wave peaks, the angle for the acoustic generation and detection point were slightly separated in the final test set.

In the final test set, the distance between the excitation point and the detection was set to 10 mm. Also the direct illumination acoustic excitation point was moved to a slightly different angle on the pipe. In Figure 10-21 (a) we can see that this generated two cleaner 2nd order direct surface wave peaks as we expected. Then the end of the direct illumination fiber was attached to the surface of the P91 pipe and surrounded by the low CTE adhesive. Another protection tube was used to secure both optical fibers on the pipe. This step completed the final state of a single FO-SHM sensing node on a P91 pipe.

Figure 10-20 Completed state of the FO-SHM node on a P91 pipe

The AE signature for the completed FO-SHM sensing node on a P91 pipe is shown in Figure 10-21 (b). As compared to Figure 10-21 (a), more bottom reflection peaks can be observed. This is possibly due to the difference in acoustic generation. It appears that confining the laser energy inside its metallic surrounding generates stronger body wave as compared to the surface illumination acoustic generation method. In the final demonstration, the direct surface waves will be used for temperature calibration and the bottom reflected waves will be used for corrosion-induced thickness change measurement.

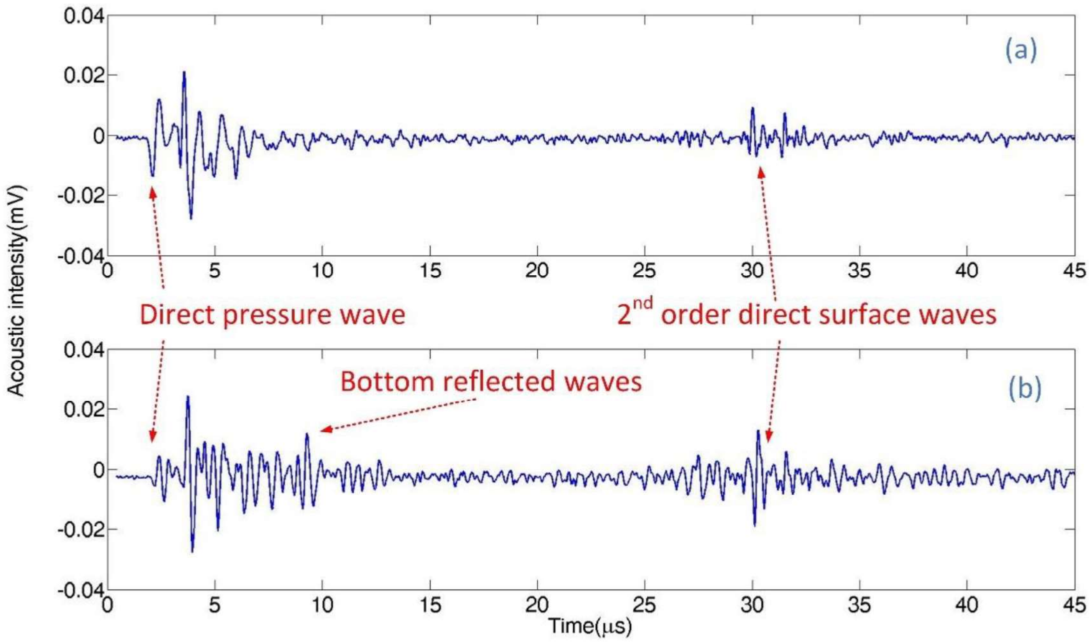

Figure 10-21 (a) AE signature for FBG and direct illumination; (b) AE signature for the completed FO-SHM sensing node

10.4.3 High temperature test results

In the high temperature test, a new P-91 FO-SHM sample was made because the previous ready-for-test sample was damaged by accident during the preparation stage. This caused the acoustic signature to be slightly different from the signal shown in the previous section. Each measurement was made after the FBG spectrum peak location was relatively stable, which indicated that the temperature was stable. A special technique was used to expedite the heating rate of the sample. To get the sample to reach a stable temperature point T fast, the furnace was adjusted to T+25 degree and let sit for 8 minutes. Then the furnace temperature was brought back to T. After 2 minutes, the FBG spectrum and the thermocouple reading would be almost stable. Besides the thermocouple integrated with the furnace, another thermocouple touching the surface of the sample was also used and the temperature was recorded by this thermocouple. The recorded FBG spectrum are shown in the Figure 10-22.

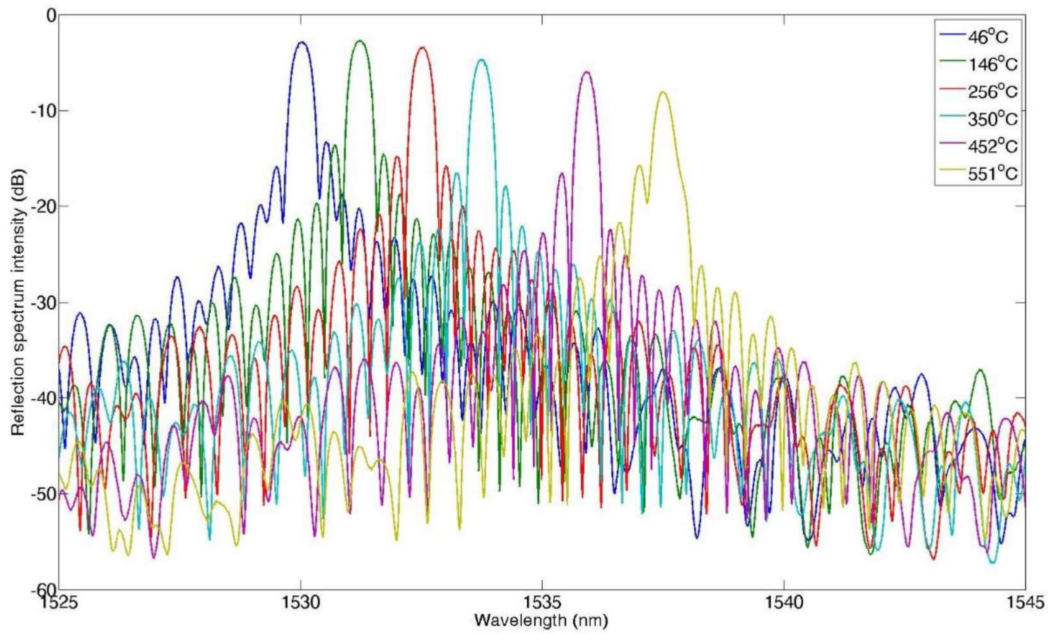

Figure 10-22 FBG spectrum during high temperature test

It can be seen that the FBG spectrum shifts to the right as the temperature rises and the peak intensity slowly drops. The drop in peak intensity is due to the usage of a type-I FBG. We can see that up to 500ºC the FBG has retained its shape very well and is starting to change shape when reaching 550 ºC. This is a significant improvement compared to the previous sample under high temperature test and has confirmed our prediction that a low CTE adhesive will help prevent inadvertent alteration to the shape of the FBG spectrum. In the final demonstration, we will improve the shape uniformity of the adhesive applied and hopefully increase the temperature threshold where the FBG spectrum turns irregular.

The acoustic signatures generated during the test are shown in the Figure 10-23, and their intensities are adjusted according to the FBG intensity. It can be seen that the direct pressure wave maintains its shape and intensity very well and can be used for temperature detection. An increase in the low-frequency vibration of the acoustic signature was unexpected. This can be viewed in Figure 10-24 where the FFT information of the acoustic signature is shown.

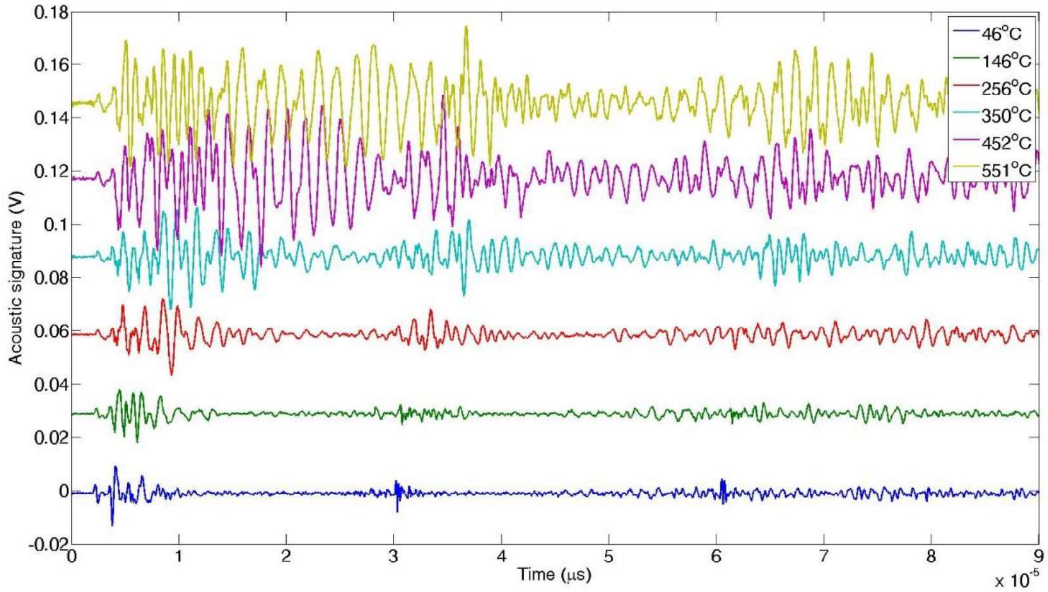

Figure 10-23 Acoustic signatures during the high temperature test, intensities calibrated by their relating FBG intensities

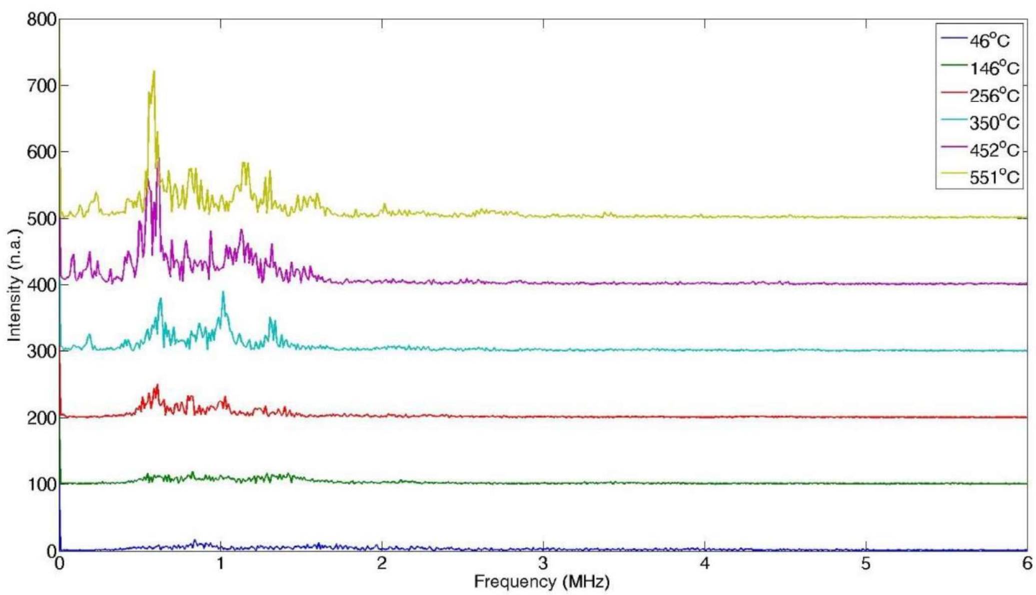

Figure 10-24 FFT information of the acoustic signatures during the high temperature test

Once the temperature reached 550°C and the FBG spectrum started to deviate from its normal shape, the temperature rise procedure was halted and the furnace was allowed to cool with its door closed. Within an hour, the temperature dropped back to 450°C and the FBG spectrum reverted to its typical shape. However, after cooling overnight, the FBG spectrum completely disappeared when observed the next morning. The spectrum became an almost flat line at around

-40dB. Strangely, the FBG fiber was not found physically broken; the visual examination of the FO-SHM section also detected no breakage. Unfortunately, when taken out of the furnace for further observation, the fiber link was damaged, preventing conclusive examination.

10.5 Type-II FO-NDE components fabrication and high temperature test

10.5.1 Type-II FBG fabrication and test

In this section, we present the fabrication and performance test of the type-II FBG. As seen in the previous experimental results, the type-I FBG will continuously degrade in the high temperature environment, thus is not suitable for our high temperature application. To solve this problem, type-II FBG was proposed to be used as the acoustic detection unit, which was reported to work stably at 1000ºC [33]. While the type-I FBG is formed by refractive index change induced by the photo-sensitive process in the germanium doped core, the type-II grating is formed by inscribing micro voids inside the fiber core with very high intensity laser. A femtosecond laser point by point FBG inscription setup was built in our lab to write this type of grating. In this system, the fs laser pulse is focused by a 100X objective lens to inscribe voids with less than 1 um diameter inside the fiber core. A high precision air bearing stage holding the optical fiber is moving with a stable speed during the inscription process. The periodical accuracy is ensured by the accuracy of the repeat rate of the femtosecond laser and the stable moving speed of the air-bearing stage. The typical parameters we used for FBG inscription are shown in Table 9. The setup is shown in Figure 10-25 and the result of typical grating inscribed by this system is shown in Figure 10-26.

Table 9 Typical type-II FBG inscription parameters

Femtosecond repeat rate	1 kHz	FBG period	1.07 um
Pulse energy	0.4 uJ	Fiber moving speed	1.07 mm/s
Pulse width	125 fs	FBG length	2 mm

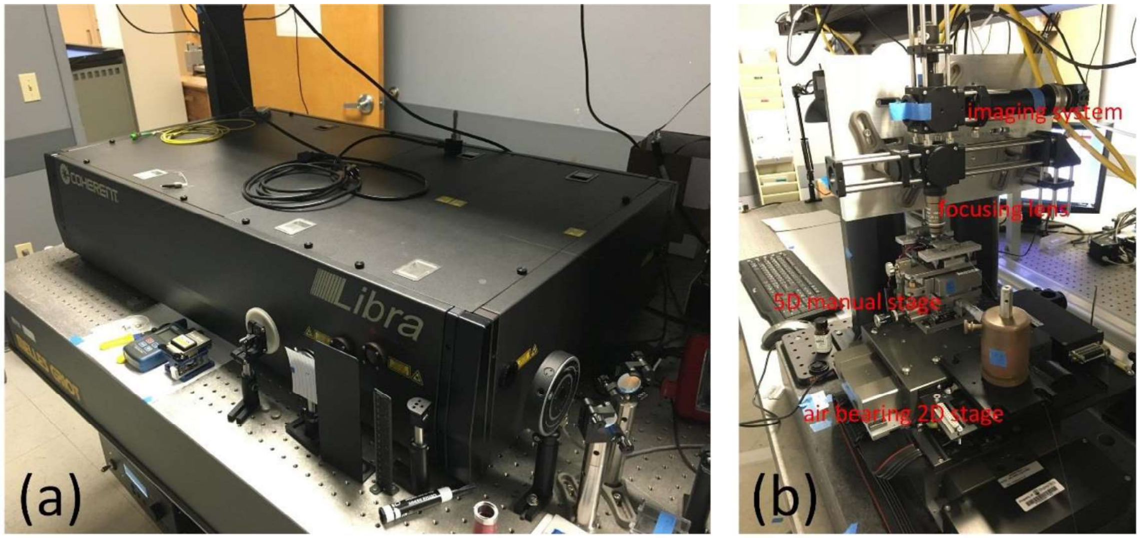

Figure 10-25 (a) The Libra femtosecond laser; (b) The point-by-point type-II FBG inscription system.

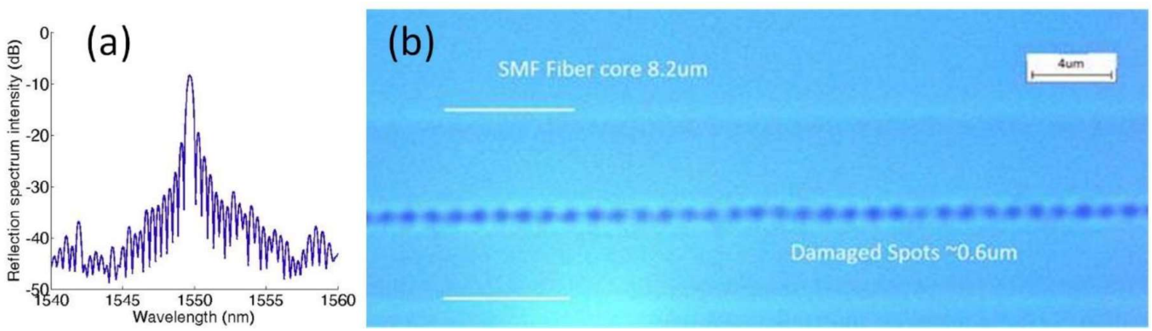

Figure 10-26 (a) Type-II FBG spectrum; (b) The periodical structure of the type-II FBG under 100X microscope.

A P-91 sample with surface attached type-II grating was then fabricated with the metallic adhesive. This sample was tested from 25ºC to 700 ºC. The FBG spectrum distortion started to show at 600 ºC and the FBG broke at 700 ºC. From 25 ºC to 500 ºC, the FBG spectrum was stable in terms of the shape and peak intensity. This result is shown in Figure 10-27.

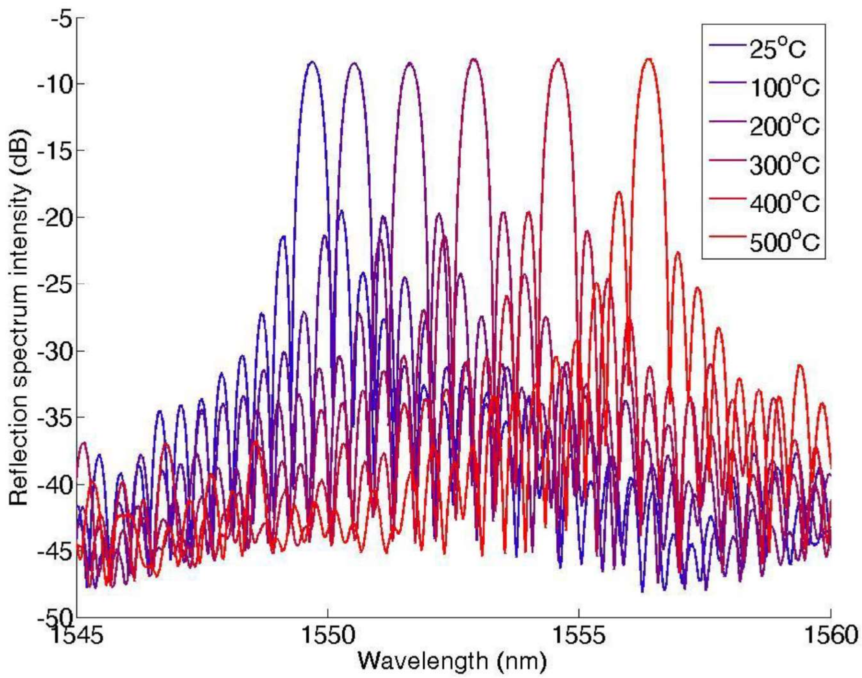

Figure 10-27 Surface attached type-II FBG high temperature test result

10.5.2 Type-II acoustic generation unit fabrication

A similar setup with 20X objective lens was built to fabricate the acoustic excitation unit used in the FO-NDE element. This lower magnification lens was used to generate larger size voids for the higher light scattering ratio. When using the parameters shown below, the size of the voids is about 10 um.

Table 10 Parameters used for the inscription of the acoustic generation type-II voids

Distance between voids	40 um	Laser pulse energy	8 uJ
Position of voids	Center of the core	Pulses for each voids	100
Total length	1mm	Total loss	10%

A typical result of the fabricated acoustic generation unit is shown in Figure 10-28. A red laser was injected into the fiber for viewing purpose, and the red dot is the scattered light from the type-II voids.

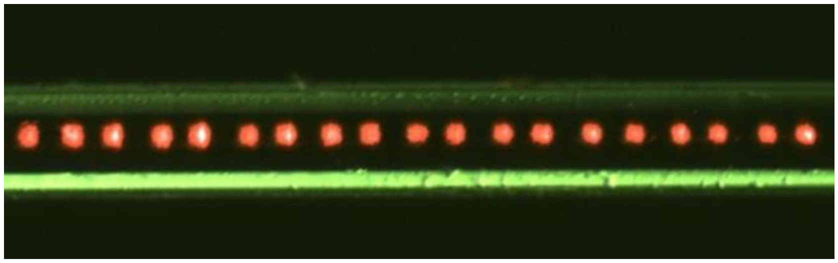

Figure 10-28 Type-II voids constructed acoustic generation unit

11 Other preparations for the final demonstration

11.1 Water-filled P-91 pipe test

Because we plan to use chemical etching in the final demonstration to simulate inner surface corrosion, it is important to know how the liquid inside the pipe will affect the acoustic signature. In this test, we first measured the acoustic signature on an empty P-91 pipe with the attached FO-SHM element. Then the pipe was filled with water as shown in Figure 11-1, and the acoustic signature was measured again. These two acoustic signatures were then compared as shown in Figure 11-2. Surprisingly, the acoustic signature didn't differ much after the pipe was filled with water. In the final demonstration, the liquid in the pipe will be an acid which may have slightly different acoustic impedance from the water. However, based on this test, we believe that the acid should not affect the acoustic signature much, which will be beneficial to experimental accuracy.

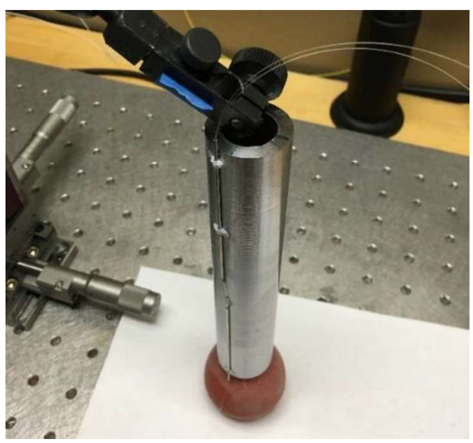

Figure 11-1 Water-filled pipe setup

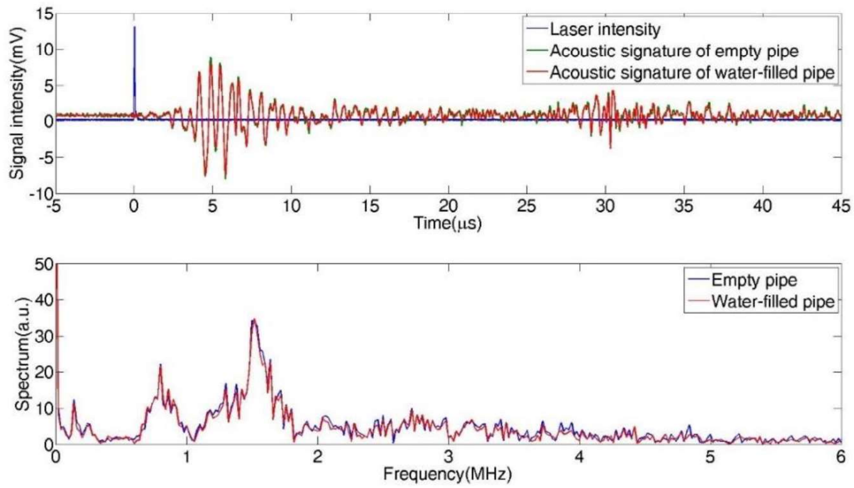

Figure 11-2 Acoustic signature comparison between empty P-91 pipe and water filled P-91 pipe

11.2 Analytical model of guided elastic wave propagation

To prepare for the final demonstration which will be using ultrasonic structure health monitoring technique on a P91 pipe, it is necessary to study the elastic wave generation and propagation on such a structure. When the thickness of a pipe is much smaller than the acoustic wavelength and the tube diameter, the elastic modes supported can be approximated by the modes supported by a thin plate [39], which are SH modes and Lamb-type modes [13]. According to our online market search, most stocked P91 pipes generally satisfy these conditions so we will use SH modes and Lamb modes to describe the elastic wave propagation on thin-wall pipes in the future study.

The frequency equations for SH modes and Lamb waves can be deduced by the elastic motion equation and stress-free boundary conditions. The results are[13]:

SH modes $$\beta^2 = (\frac{\omega}{V_S})^2 - (\frac{n\pi}{d})^2, \qquad n = 0,1,2,3.......... \tag{26}$$

Symmetric Lamb waves $$\frac{\tan(qd/2)}{\tan(pd/2)} + \frac{4\beta^2 qp}{(q^2-\beta^2)^2} = 0 \tag{27}$$

Anti-symmetric Lamb waves $$\frac{\tan(qd/2)}{\tan(pd/2)} + \frac{(q^2-\beta^2)^2}{4\beta^2 qp} = 0 \tag{28}$$

Here β is the wave number, ω is the frequency, d is the thickness of the plate, V_S is the shear wave speed in this bulk material, V_L is the shear wave speed in this bulk material, p and q are defined as followed.

$$p^2 = (\frac{\omega}{V_L})^2 - \beta^2, \; q^2 = (\frac{\omega}{V_S})^2 - \beta^2 \tag{29}$$

Using MATLAB to solve these equations we acquired dispersion curves for these three modes, the results are shown in Figure 11-3. The X axis of the dispersion curves is the product of the frequency and the thickness of the tube, the Y axis is the phase velocity. It can be seen that when the thickness of the tube changes, such as due to corrosion, these dispersion curves will shift and consequently change the acoustic signature of a pipe. Therefore this provides a possible way to monitor the thickness of a thin-wall pipe.

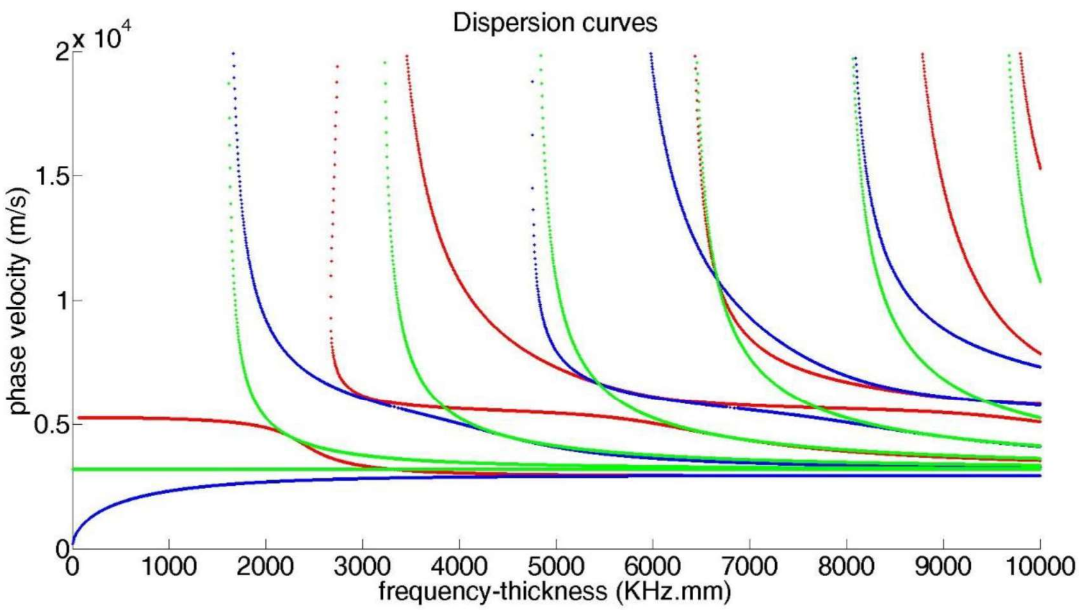

Figure 11-3 Dispersion curves for symmetric Lamb waves (red curves), anti-symmetric Lamb waves (blue curves) and SH waves (green curves)

11.3 FEM simulation of the guided elastic wave and experimental result

11.3.1 Simulation of elastic wave generation on a thin-wall tube with laser heating

To study the elastic wave generated by laser heating, a simulation model was built with the COMSOL thermal-elastic module. A thin-wall tube with 0.5” diameter and 0.5mm wall thickness was used as the testing workpiece. A 1 mm by 1 mm surface area was chosen as the heat source in-flow area, to represent the laser heating area. The time profile of the in-flow heat was set to a Gaussian pulse with 50ns standard deviation which agrees with the laser source we used in the experiment. Due to the fact that a P91 material can’t be found in COMSOL’s material library, the properties of standard steel AISI 4340 was used in the simulation. As seen in Figure 11-4, the generated elastic waves propagate with circular wave fronts.

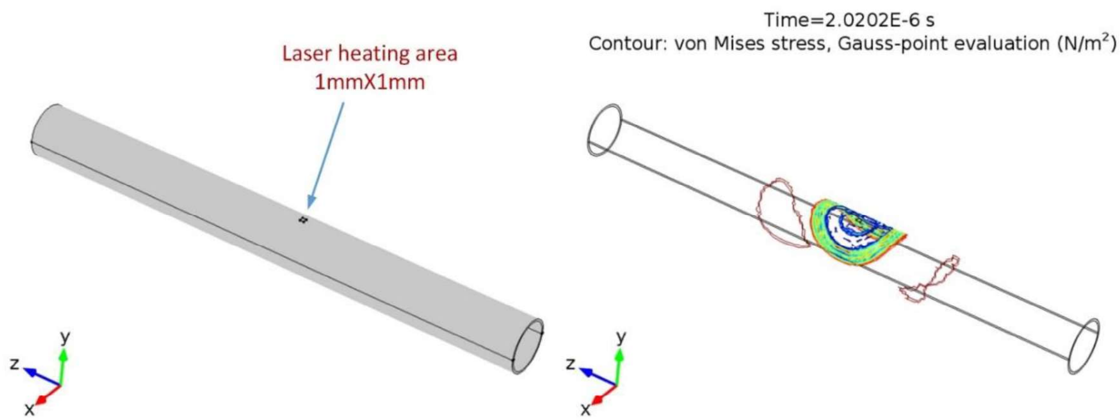

Figure 11-4 COMSOL simulation result of elastic wave generation by laser heating

The propagation of the elastic waves was monitored in a surface point 1cm away from the source area. The monitored value was the surface displacement in Y direction (normal to the surface). The result will be shown together with an experimental verification result in the following section.

11.3.2 Comparison of simulation result and experimental result

To verify the accuracy of the COMSOL simulation, a confirmatory experiment was conducted with direct laser heating and EFPI sensing. A copper tube with very similar sizes to the simulation model was used in the experiment. A multimode fiber which guided the high-intensity laser pulse pointed to the surface of the tube with about 2mm distance from the surface, this generated a circular heating area with roughly 1 mm diameter. The polished end surface of a single-mode fiber was placed near the surface of the tube (distance smaller than 1mm), served as the EFPI sensor that detects the surface displacement in the normal direction. The laser used for acoustic generation is the 1064nm Nd:YAG laser with 50ns pulse width and 0.3mJ pulse energy, the laser source used for EFPI is a tunable C-band laser.

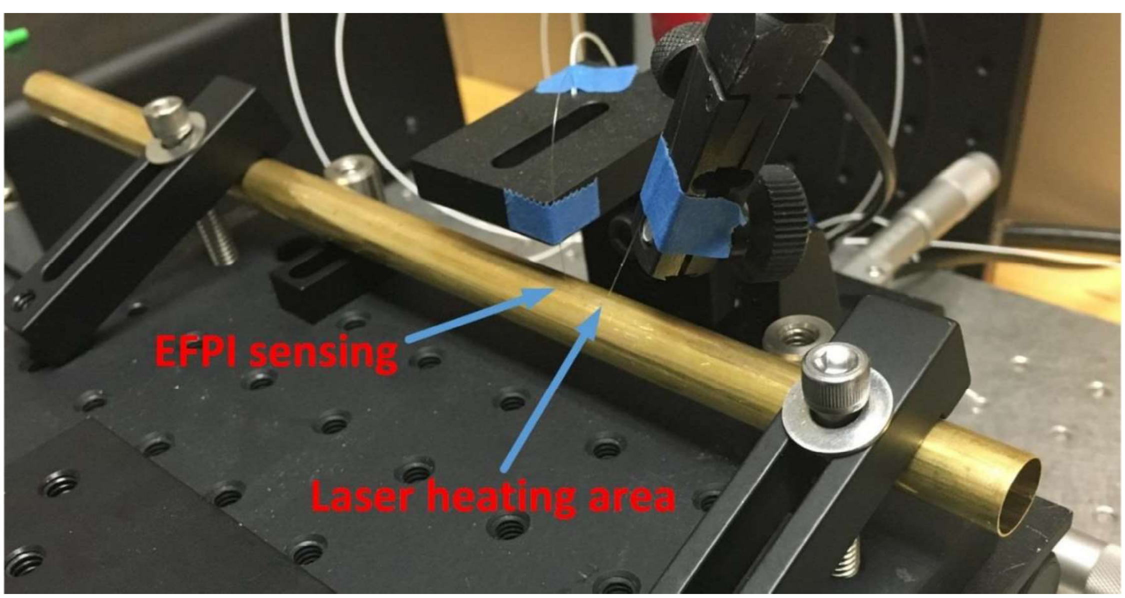

Figure 11-5 Experiment setup for thin-wall tube elastic wave generation and detection

The normalized acoustic signatures from both the simulation result and the experimental result are plotted in the upper graph in Figure 11-6. The features of these two plots are similar in terms of the transition from several smooth vibrations to vibrations with higher frequency spikes. The lower graph in Figure 11-6 shows the Fourier transformations of these two acoustic signatures, and they are very similar. Although these two acoustic signatures are similar, there is still a noticeable difference between them such as the total time duration of the smooth vibration area. These differences should be caused by three reasons. Firstly, the laser heating area in the simulation model is a rectangular area while in the experiment it is a circular area. Secondly, the material used in the COMSOL model is stainless steel and the actual material used is a certain type of copper. Finally, the mesh size in the simulation model may not be fine enough to give a high accuracy prediction. The mesh used in the current simulation is in the fine grade and a single run of the simulation takes about one day. In the next quarter, we will try higher mesh sizes and see if they will produce more accurate results.

In all, we believe this model is good enough for preliminary experiment prediction, such as studying the effect of changing tube thickness or cracks on the acoustic signature. This will save time for future experiment and help prepare the final demonstration.

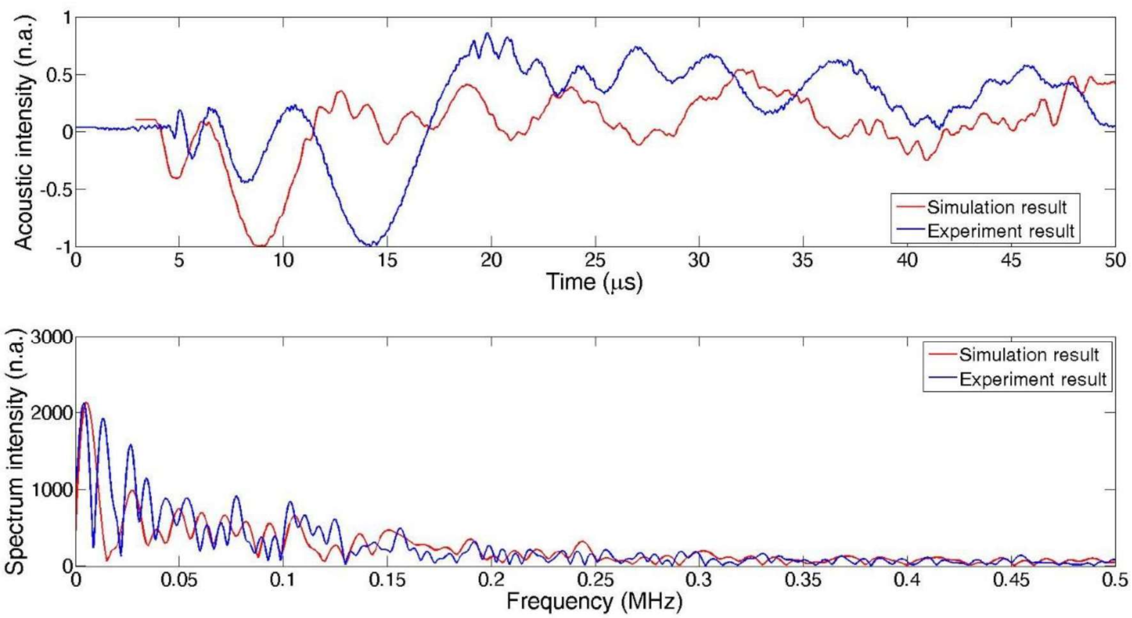

Figure 11-6 Results comparison between the COMSOL simulation result and the experimental result

11.4 Single point acoustic generation improvement

11.4.1 Test of inline light scattering acoustic generation

In the previous experiments, a single point light scattering mechanism was used in the AGU. As shown in Figure 11-7 (b), several type-II voids are inscribed inside the multimode fiber at a single point by a femtosecond laser. With such a structure, light scattering only happens at this single point and so is the acoustic excitation. In this case, the generated acoustic pulse width will be determined by the time duration of the laser pulse which is very short. This short acoustic pulse can easily be dislocated by the irregular shape of the adhesive holding the AGU. There are two ways to minimize this effect so a truer acoustic signature can be obtained. The first one is to use a laser with longer pulse duration, preferably tunable pulse width. The other way is to generate distributed light scattering in an AGU instead of single point light scattering. In this way, the pulse width of the generated acoustic waves will be similar to the size of the acoustic generation area. In this quarter, the second method was tested by fabricating an FO-SHM sensor with inline light scattering voids as shown in Figure 11-7 (a). Its acoustic signature was compared to another FO-SHM sensor with single point light scattering structure. All other parameters for these two FO-SHM sensors are the same, including the total light loss in the AGU, the size of the sample, sensor position on the sample, etc.

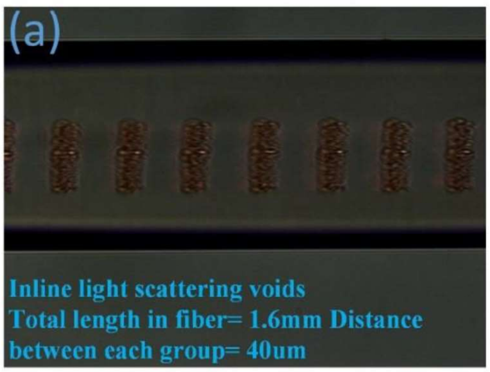

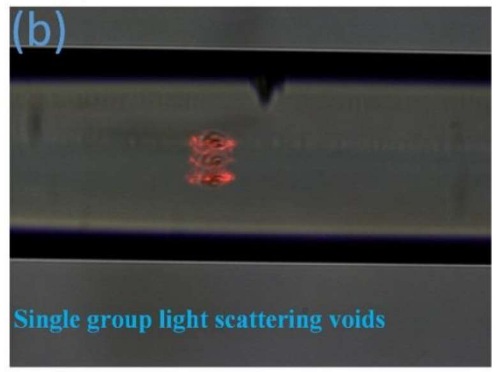

Figure 11-7. (a) Microscope photo of inline type-II voids; (b) microscope photo of single group type-II voids.

As the left two graphs in Figure 11-8 show, pulses in the acoustic signature of the FO-SHM sensor made with inline AGU are broader than the pulses generated by the single point AGU. The comparison between the spectrums of this two acoustic signatures shows that the inline AGU signal has stronger components in the frequency range lower than 2 MHz while the single point AGU signal has stronger components in the frequency range higher than 2 MHz. These comparisons agree with our expectation that by increasing the size of the acoustic excitation area, the generated acoustic pulses will have longer pulse width.

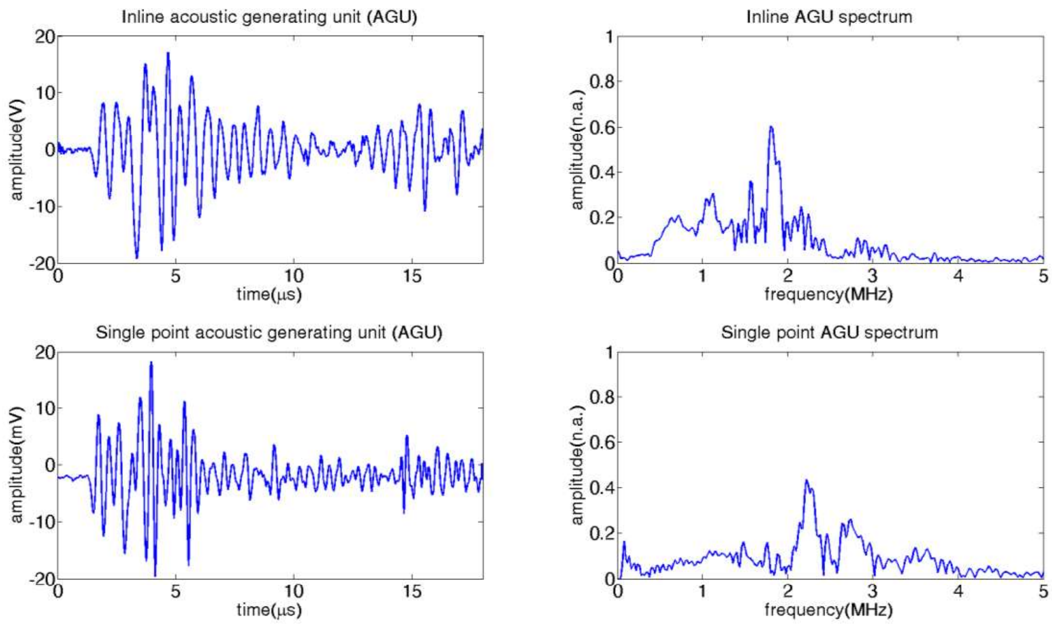

Figure 11-8. Top graphs: Acoustic signature and spectrum of the FO-SHM testing sample made with inline AGU; bottom graphs: Acoustic signature and spectrum of the FO-SHM testing sample made with single point AGU.

This is a useful finding for future experiments because that controlling the acoustic excitation geometry allows adjusting the pulse shape in the acoustic signature.

12 Final in-lab demonstration result

12.1 Step one - high temperature tests using standard optical

Several high temperature tests were performed on P-91 pipes with type-II FO-NDE elements and a metallic adhesive. As we have observed in these high temperature tests, the acoustic signatures suffered irregular changes after the temperature was raised above 200ºC. The temperature dependent acoustic attenuation and coupling efficiency were firstly considered to be the main causes for this phenomenon. Later, we discovered that after being heated to high temperature, the fiber had significant light leakage from the fiber sections that surrounded the acoustic generation point. We started to believe that this type of light leakage was the cause for the observed problem. To verify this, we coated the acoustic generation fiber with a thin layer of silver in the attempt to absorb the cladding mode light and block the leakage. During the following high temperature tests, the acoustic signatures became more predictable compared to the previous high temperature tests. However, the coating started to degrade above 300ºC and the irregular acoustic signature changes started to appear again.

12.1.1 High temperature tests with standard 105/125μm fiber

A typical sample is shown in Figure 12-1. During these tests, we found the acoustic signatures were not consistent when heated above 200ºC. In several cases, the position of the first pulse in the acoustic signature moved forward in the time domain when temperature increased, which is against our prediction because the speeds of elastic waves generally decrease when the temperature rises. A typical result of the acoustic signature evolution is shown in Figure 12-2.

Figure 12-1 P-91 sample with type-II FO-NDE elements

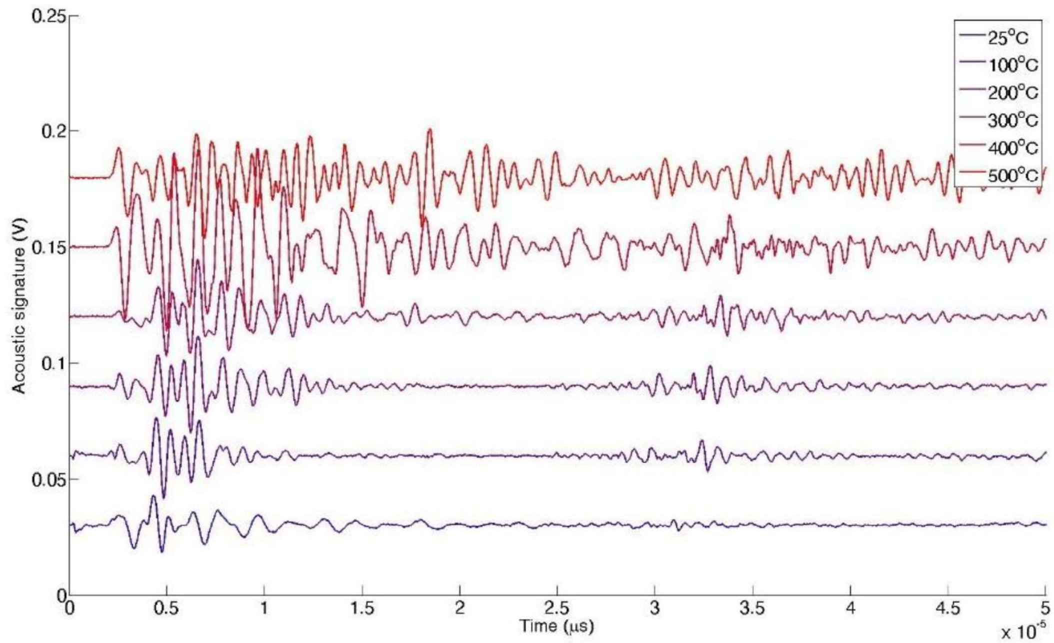

Figure 12-2 Acoustic signature evolution in high temperature environment

By examining the samples after the high temperature tests, we discovered that the acoustic generation fiber developed severe light leakage around the acoustic excitation point during the tests. This phenomenon is shown in Figure 12-3. Due to these unwanted light leakage, the properties of the acoustic source were significantly changed in high temperature environment, which rendered the acoustic signature un-predictable.

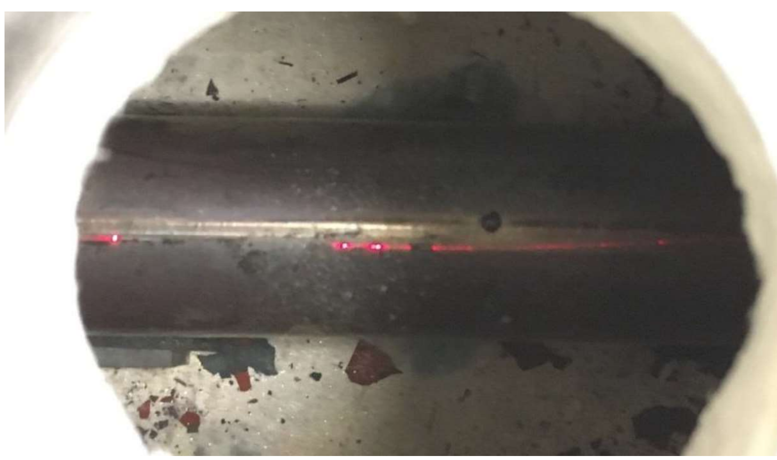

Figure 12-3 Fiber light leakage after a high temperature test

12.1.2 Silver coated 105/125 μm fiber fabrication process

To solve the light leakage problem, we tried to fabricate silver coated multimode fiber and use it as the acoustic excitation fiber. The design is to coat the standard 105/125 μm multimode fiber with a thin layer of silver by a sputtering machine. After the fiber is coated, about 3 mm of the coating will be removed acoustic generation unit inscription. Then the acoustic generation unit will be surface-attached to the P-91 pipe as before. The sputter setup for the silver coating is shown in Figure 12-4. In this process, the fiber was rotated 120 degrees twice to ensure that the fiber is fully covered by silver.

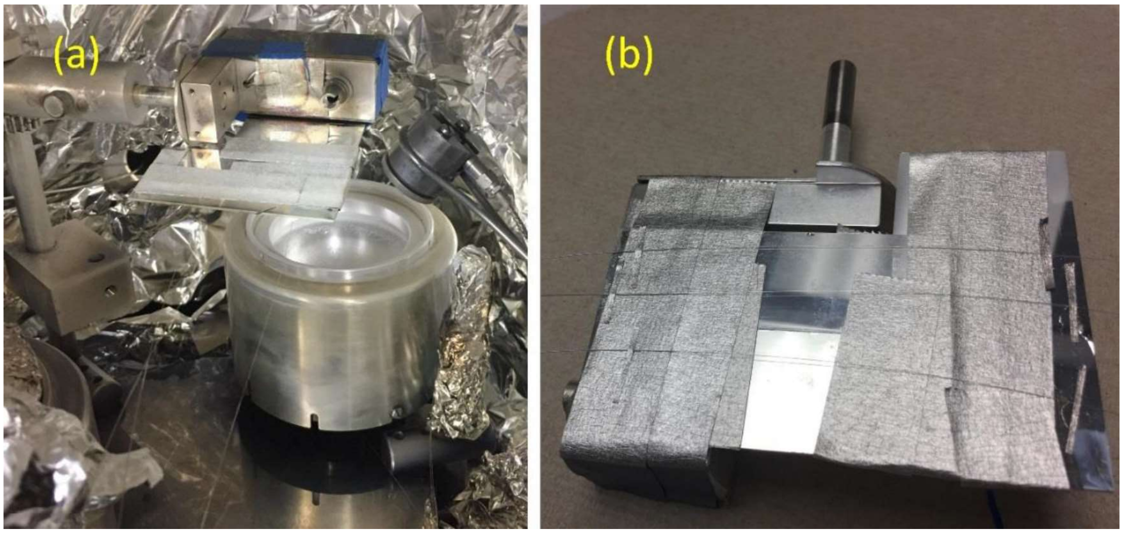

Figure 12-4 Silver coating fiber sputter setup

After the fiber was coated with the silver coating, a fiber section slightly longer than the type-II voids section was de-coated, and this section was used for the acoustic generation unit inscription. The product of this process is shown in Figure 12-5. The thickness of the silver coating is about 1 um and the length of the type-II voids section is 2 mm.

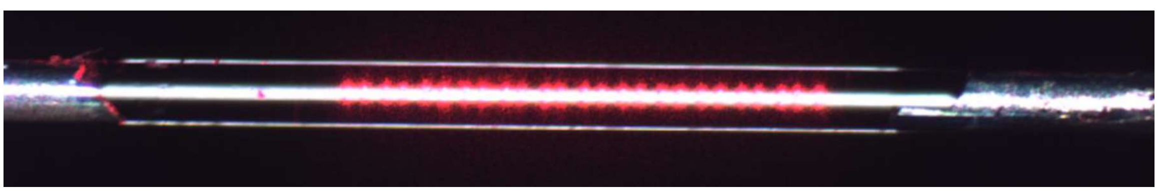

Figure 12-5 Acoustic generation unit on silver coated fiber

12.1.3 High temperature tests with silver coated 105/125µm fiber

With the silver coating fiber, several FO-NDE elements were fabricated and put through high temperature tests. During these tests, it was found that the coating started to delaminate at around 300ºC. As shown in Figure 12-6, the scattering light started to appear at 300ºC and became very strong at 600ºC. The quality and the thickness of the coating may be the cause for this phenomenon. However, we were still able to confirm that the acoustic signature became more predictable below 400ºC comparing to the experiment results acquired with non-coating fiber. As shown in Figure 12-7, the acoustic signature maintains its own shape well up to 300ºC and shows some trailing pulses after the main envelope. A zoom-in view of the main envelope as in Figure 12-8 shows that the first several pulses in the acoustic signature shifts monotonically in the whole process, which should be caused by the temperature induced acoustic velocity change.

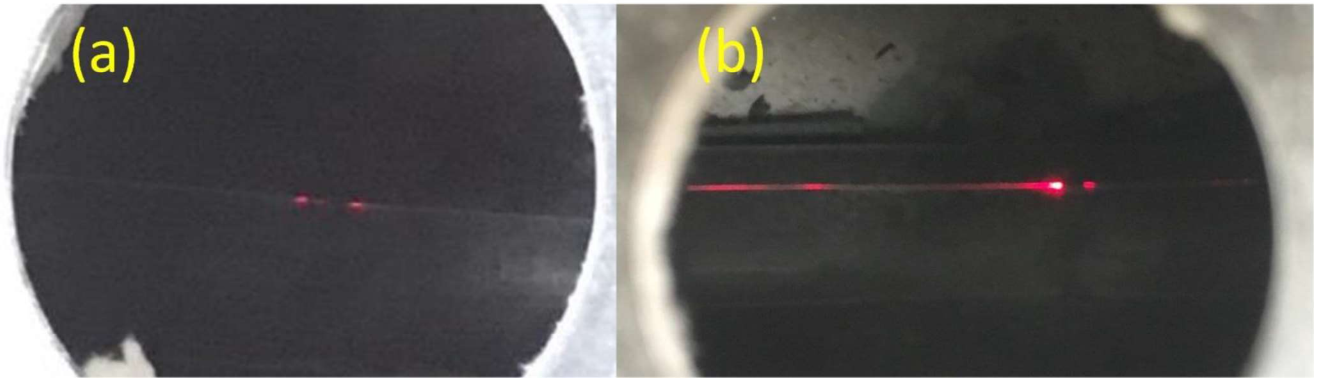

Figure 12-6 (a) Light leakage at 300°C; (b) Light leakage at 600°C.

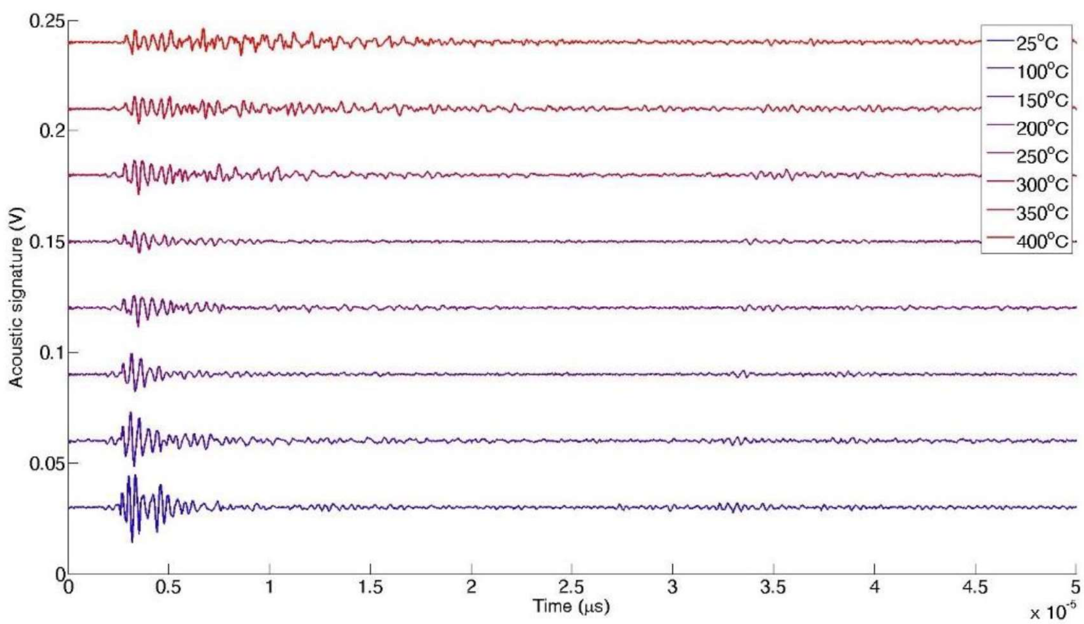

Figure 12-7 Overall view of the acoustic signature evolution with silver coated fiber

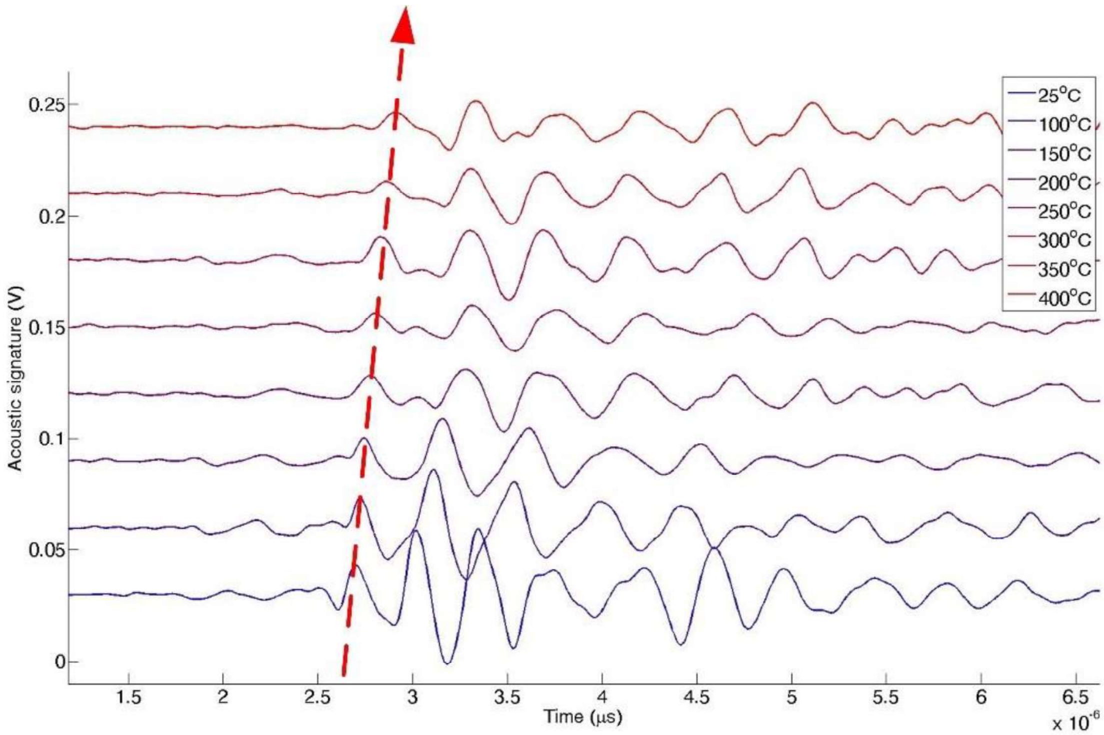

Figure 12-8 Zoom-in view of the front section of the acoustic signature evolution

12.1.4 Chapter summary

Based on this result, we believe that solving the light leakage problem will bring significant improvement to the readability of the acoustic signature in high temperature environment. And it is a necessary step to achieve the goal of measuring environmental parameters for high temperature applications. To achieve this, we acquired some commercial gold coated multimode fiber and fabricated the acoustic generation unit on this fiber. Because the coating quality of the commercial gold coated fiber is higher and the fiber is rated up to 700ºC, the result was substantially improved as discussed in the next chapter.

12.2 Step two - high temperature tests using gold coated optical fiber

After confirming the importance of eliminating unwanted light leakage from the acoustic generation fiber, we searched the market and purchased a gold coated 105/125 µm step index multimode fiber. The thickness of the gold coating is 15 um, which makes the overall fiber diameter 155 um. This fiber is rated up to 700ºC which is sufficient for our application. Several tests were performed with this fiber replacing the standard 105/125 µm fiber we used before. To fabricate the acoustic generation unit (AGU) on this fiber, a portion of the fiber slightly longer than the AGU was de-coated. Figure 12-9(d) shows the AGU after the type-II voids were inscribed. The AGU was then attached to a P-91 pipe with a metallic adhesive as shown in Figure 12-9(e). To prevent unwanted light leakage, the metallic adhesive was slightly longer than the de-coating area and contacted both ends of the gold coating. A completed P-91 sample is shown in Figure 12-9(a). Four ceramic tubes were used to secure the fiber on the pipe, which allowed fiber sliding and prevented fiber bending during the high temperature test. After heating to 600ºC and cooling down to room temperature, the FO-NDE element and the gold coating fibers were intact under visual observation as shown in Figure 12-9(c).

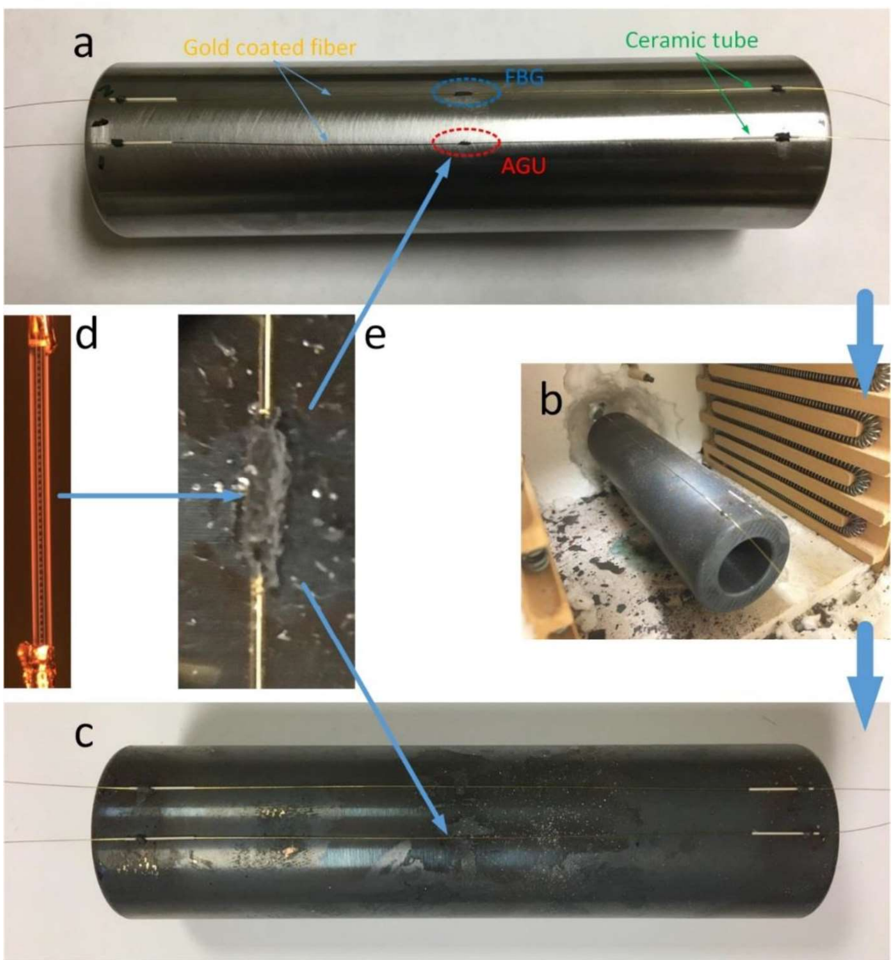

Figure 12-9 (a) P-91 high temperature test sample with gold coated fiber FO-NDE element attached; (b) Sample in the furnace; (c) FO-NDE element remains in good shape after heating; (d) Acoustic generation unit on a gold coated fiber; (d) Acoustic generation unit attachment on the P-91 pipe.

During the high temperature tests, we injected a red laser beam into the FO-NDE elements and observed the sample from a hole on the top of the furnace. During several tests performed with the gold coated fibers, no unwanted light leakage was observed. The acoustic signature evolution in one of these tests is shown in Figure 12-10. The temperature induced peak shifts can be clearly observed on both the direct surface Rayleigh waves and the surface waves that travel a full round on the pipe. The result also shows that the acoustic signature is more stable after passing 200ºC. This should be due to the fact that the final curing of the adhesive happens at this temperature.

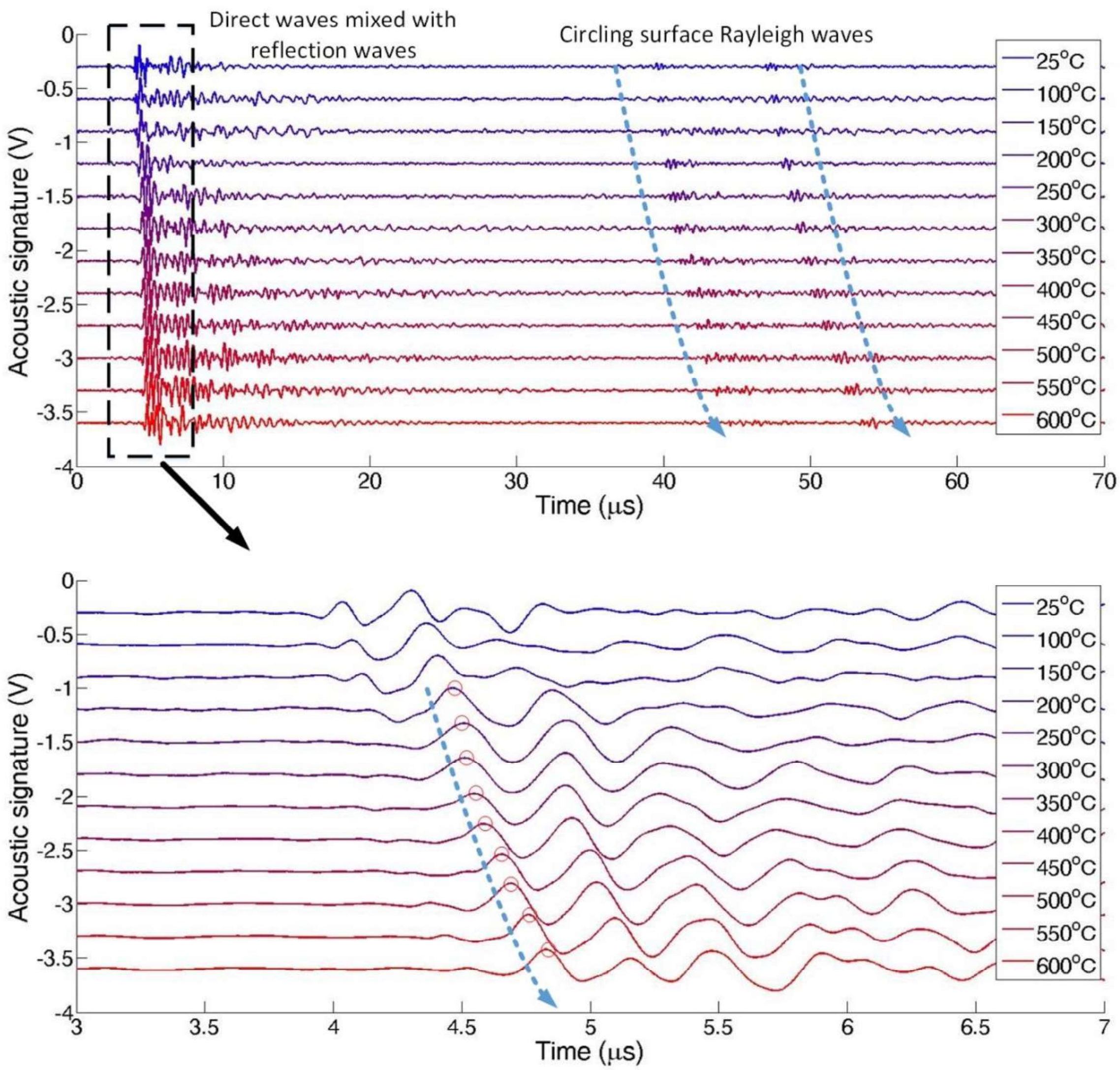

Figure 12-10 Acoustic signature evolution during the high temperature test.

During these tests, another issue was revealed during the repeated heating/cooling process. Although the FBG could maintain its shape relatively well during the first temperature rising process, which agrees with what we have observed during the previous experiment, it performed poorly during the cooling down process. One typical result is shown in Figure 12-11(a). During the cooling down process, the FBG spectrum shows irregular changes and decrease in the peak reflectance. In addition, the FBG center wavelength is not repeatable by comparison between the heating and the cooling processes. This can be observed in Figure 12-11(b, c).

We suspect that the cause for this issue is the weak bonding between the metallic adhesive and the silica fiber. During the heating up process, the fiber may slip inside the metallic adhesive due to the CTE mismatch and the low bonding strength. In the cooling down process, the adhesive may shrink rapidly and exert non-uniform stresses on the FBG and make the spectrum distorted. Although the occurrence of this issue was somewhat random, we decided that this should be solved for the preparation of the long term high temperature tests. In the next chapter, we will present an innovative upgrade to the current FBG sensing structure which ensures long term stability and repeatability.

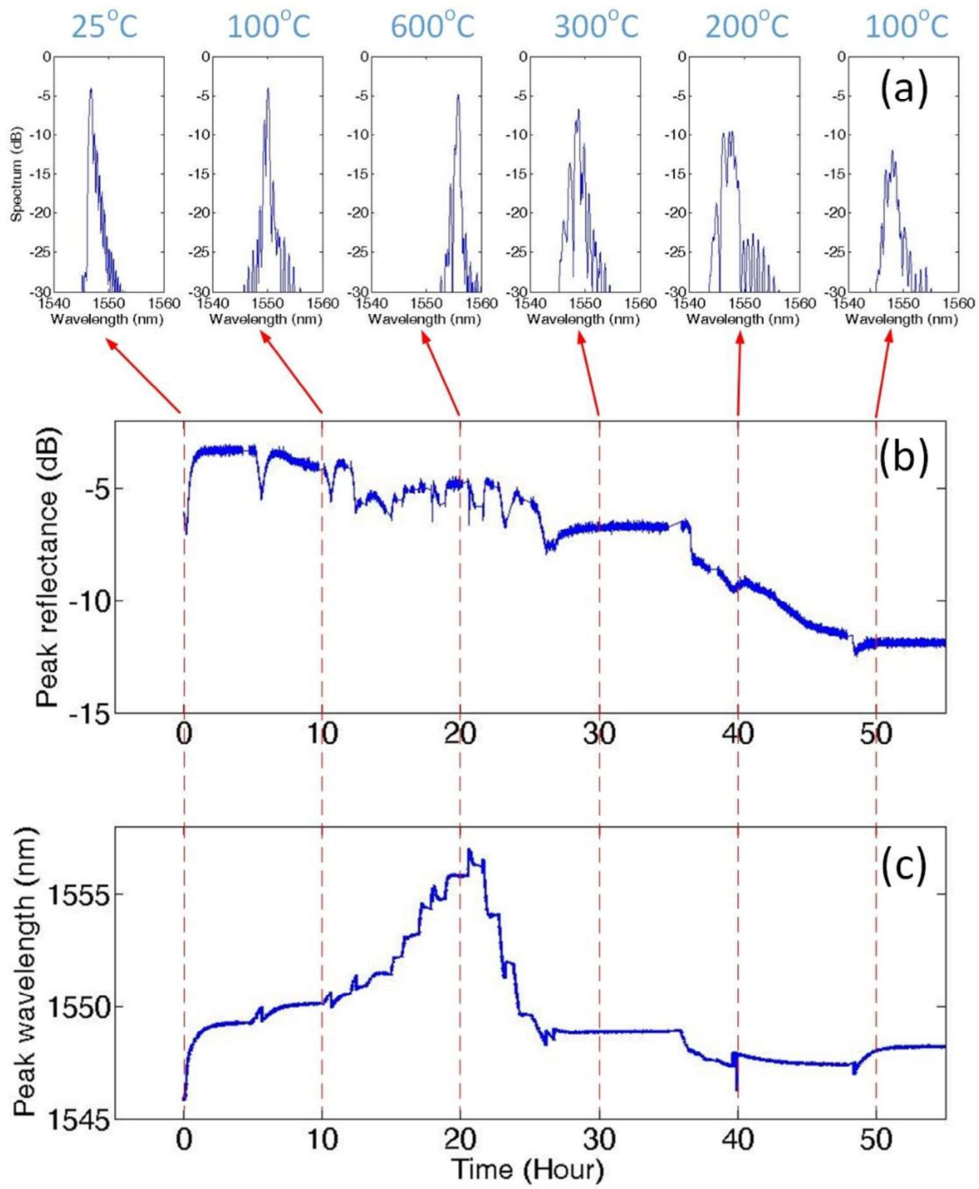

Figure 12-11 (a) FBG spectrums during a high temperature test; (b) FBG peak reflectance evolution; (c) FBG peak wavelength evolution.

12.3 Step three - high temperature tests using FP-FBG sensing structure

12.3.1 Principle of FP-FBG

In this chapter, we replaced the type-II FBG with a type-II FP-FBG to eliminate the FBG spectrum distortion experienced during the repeated temperature changing process. An FP-FBG is constructed with two in-line FBGs separated by a certain gap distance, which determines the free spectral range (FSR) of the FP cavity. Using a relatively large gap distance, such as 2 cm, an FSR around 50pm can be obtained, which is much smaller than the FWHM of a traditional FBG. Because the FSR of an FP-FBG is smaller, the acoustic detection sensitivity can be higher than an FBG. However, the most significant advantage of using an FP-FBG for high temperature acoustic sensing is that the adhesive doesn't need to be applied directly onto the FBG. Instead, the adhesive can be applied anywhere between the two FBGs. This leaves the FBGs free standing, which eliminates any possible thermal stress in the FBGs even at high temperatures. A schematic of this design is shown in Figure 12-12 together with a simulated spectrum and an actual spectrum acquired in the following experiments. Assuming the probe light enters the FP-FBG from the left, the length of the FBG on the right is designed to be longer than the FBG on the left. This is due to the consideration of type-II FBG transmission losses. If the lengths of the two FBGs are the same, due to type-II FBG losses, the reflection from the right FBG will be significantly weaker than the left FBG, which will result in a low FP fringe contrast. During the experiment, we did several tests and found that a (0.5 mm FBG +2 cm gap +1.5mm FBG) type-II FP-FBG could give a good fringe contrast (> 50%). The experimental result shown in Figure 12-12 actually has around 50% fringe contrast. The fringe contrast seems lower than 50% only due to the limited CTS spectral resolution. Figure 12-13 shows a P-91 sample with the FP-FBG implemented for acoustic sensing. The adhesive between the FBGs is about 2mm long.

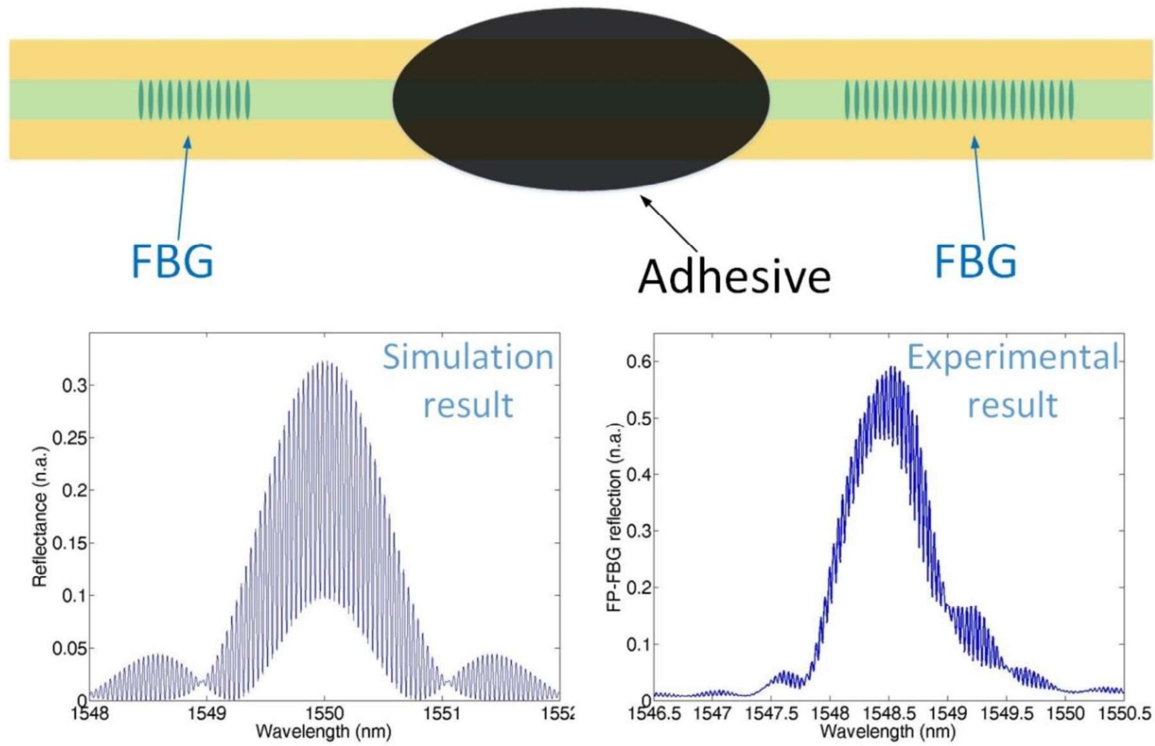

Figure 12-12 Principle of the FP-FBG acoustic sensing

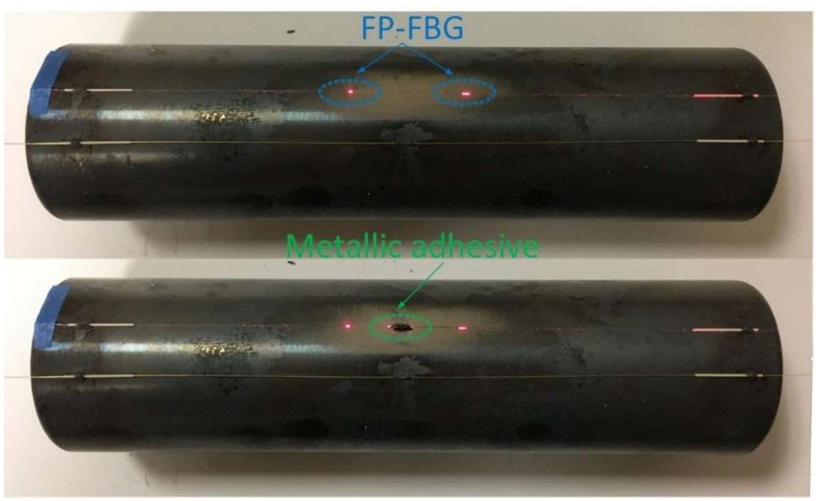

Figure 12-13 P-91 test sample prepared with FP-FBG for acoustic sensing

12.3.2 High temperature test results

Figure 12-14 shows the spectrum evolution of the FP-FBG during one of the high temperature tests we performed. It can be seen that the spectrum maintains its shape very well during the process and is highly repeatable. The variance of the peak reflectance is less than 0.5 dB during the whole process. The peak wavelength is recorded by filtering the spectrum and then using a centroid algorithm. The repeatability of the peak wavelength is within 50 pm.

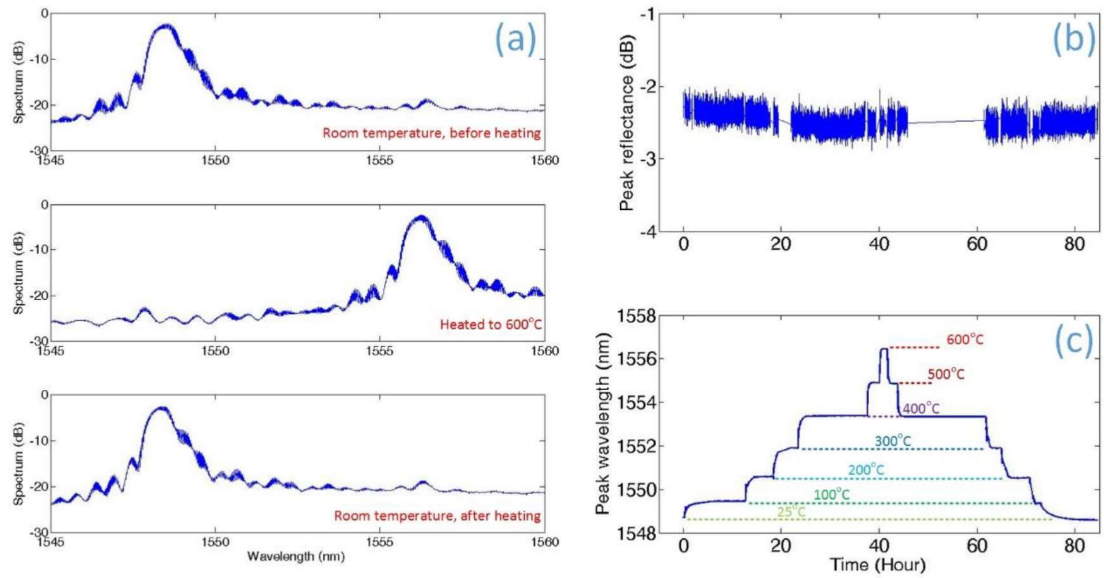

Figure 12-14 (a) FP-FBG spectrum evolution during a high temperature test; (b) Peak reflectance evolution; (c) Peak wavelength evolution.

An acoustic signature evolution was also recorded and is shown in Figure 12-15. This result is similar to what we have shown in the previous chapter. The surface waves traveling one round of the pipe show good temperature dependent shifts in the time domain. The direct waves show good temperature dependent shifts beyond 200°C.

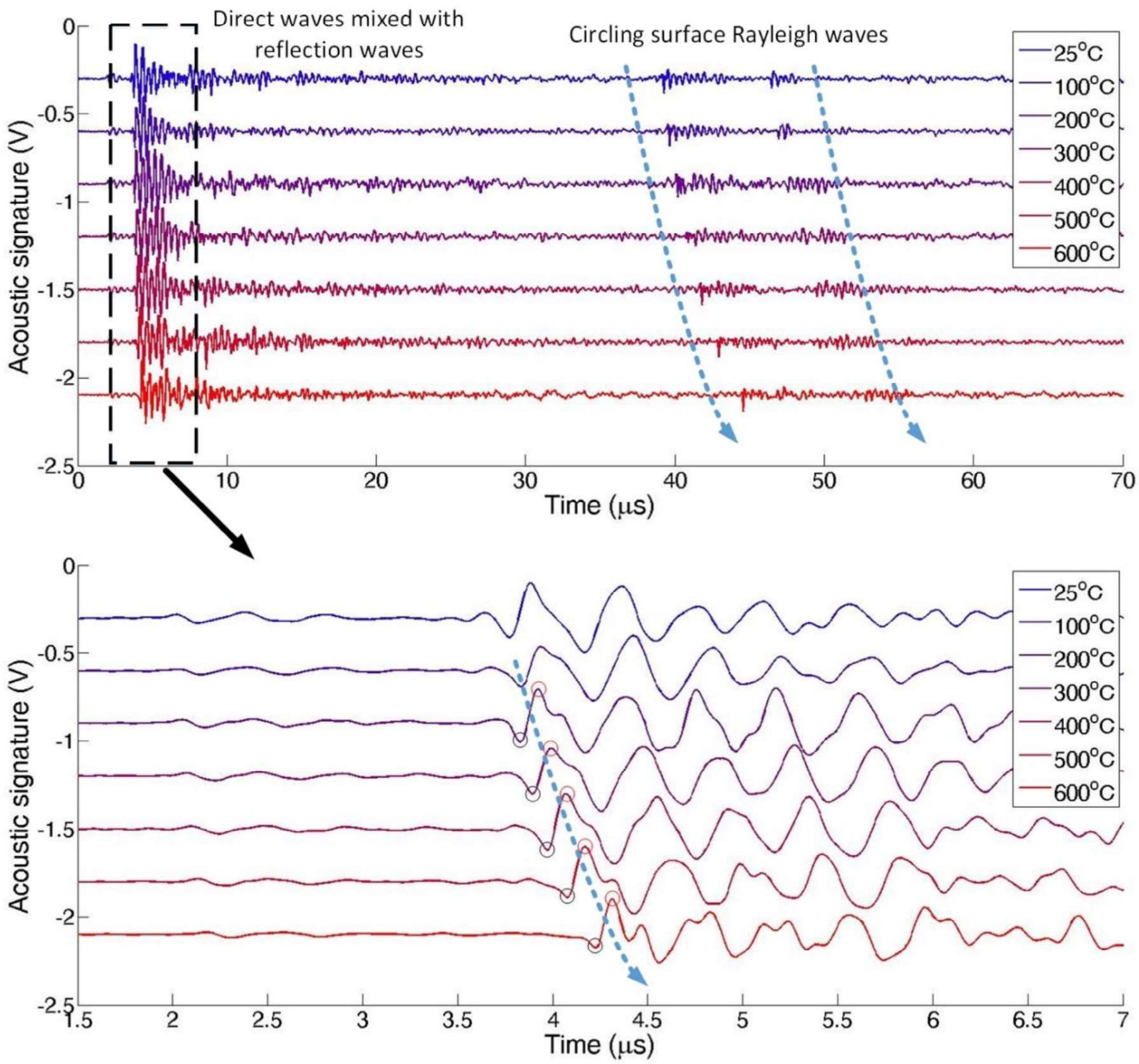

Figure 12-15 Acoustic signature evolution during a high temperature test

12.3.3 Chapter summary

We have demonstrated the operation of an innovative FO-NDE element at temperatures up to 600ºC. The spectrum is stable and repeatable which can be used to measure temperature. The acoustic signature is stable in the high temperature environment, which also shows good and predictable temperature dependent shifts in the time domain.

12.4 Corrosion, strain and crack tests

In this chapter, we will demonstrate the corrosion, strain and crack tests on a P-91 pipe in the room temperature with the finalized FO-NDE structure described in the previous chapter.

12.4.1 Corrosion test

We used an electro-etching process to simulate the chemical corrosion that may happen inside a P-91 pipe as shown in Figure 12-16(a). Before the process, the inside of the pipe was roughly polished to remove the protection paint inside the pipe, which will prevent the corrosion from happening if not removed. After the rough polishing, the inner surface was still very coarse and has many small dents on it. The chemical used for the etching was a NaCl solution. The anode was connected to the pipe through a thin copper sheet, and a metal rod was inserted into the pipe as the cathode. The current used for the etching was set at 1.98 A. The solution was cycled after every few minutes to maintain the etching speed and remove the debris. Due to the heat generated during the etching process, the acoustic signatures were each taken after a long time cooling process. This brought the temperature of the sample back to the room temperature for each acoustic signature measurement.

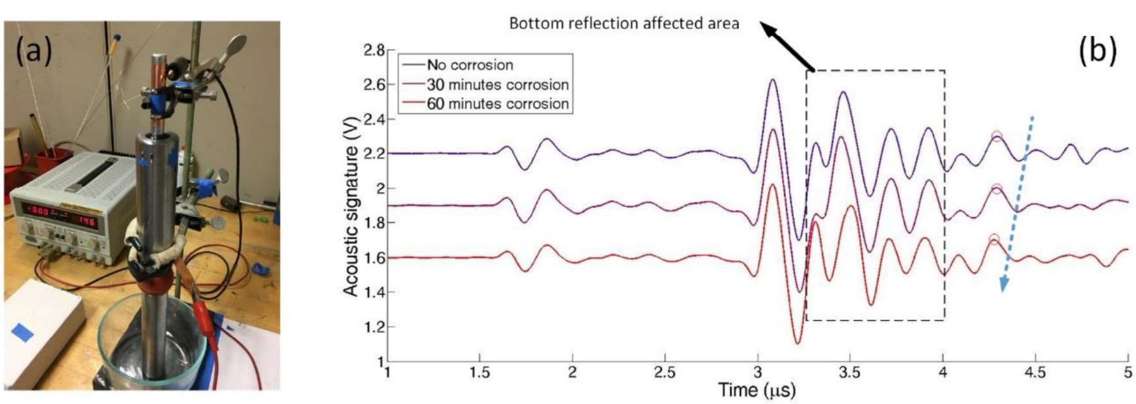

Figure 12-16 (a) Pipe inner surface electro-etching setup; (b) Acoustic signature evolution during the corrosion process

The result is shown in Figure 12-16(b). Due to the roughness of the etched surface and the mixing of bottom reflections and direct waves, the peak shifts in the "bottom reflection affected area" is irregular and not monotonic. On the right of this area, where there should only be bottom reflections, a peak around 4.5 μs is found to show monotonic shift to the left. The calculated wall thickness change is about 1.25%.

This test demonstrated that the occurrence and severity of corrosion can be indicated by the changes in the acoustic signature. To achieve better result in the future, such as a major peak shifting monotonically with corrosion thickness, longer acoustic pulse width may be used to reduce the negative effect of a poor inner surface quality.

12.4.2 Strain test

In the strain test, we used a hydraulic pump jack to exert compressional force on the sample. The setup of this test is shown in Figure 12-17. An OMEGA strain foil gauge was attached on the sample to provide a strain reference in the axial direction.

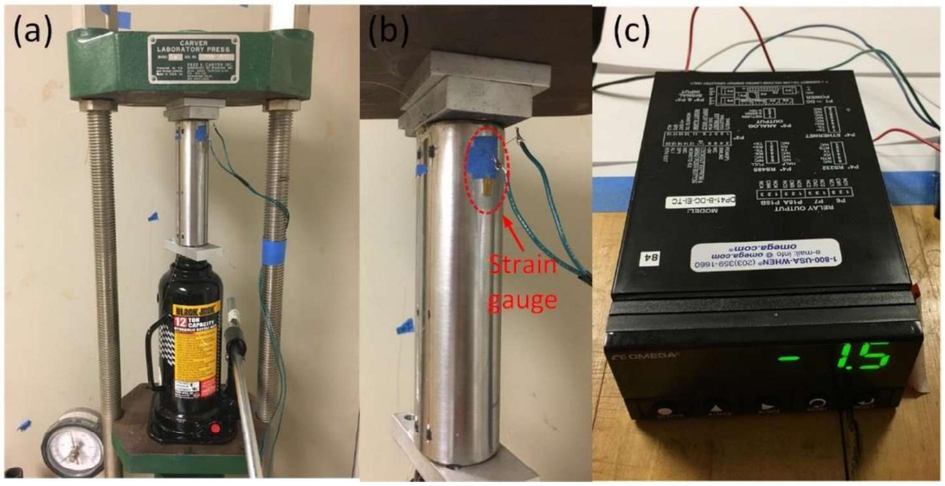

Figure 12-17 Strain test setup

During this test, we measured the peak shift of a surface Rayleigh wave that travels two rounds on the pipe. The location of this peak is around 83 μs. As shown in Figure 12-18, this peak shifts monotonically with the applied strain on the sample. The less-than-ideal linearity may be due to the fact that the strain gauge is attached close to the end of the sample and the strain distribution near the end is non-uniform and irregular.

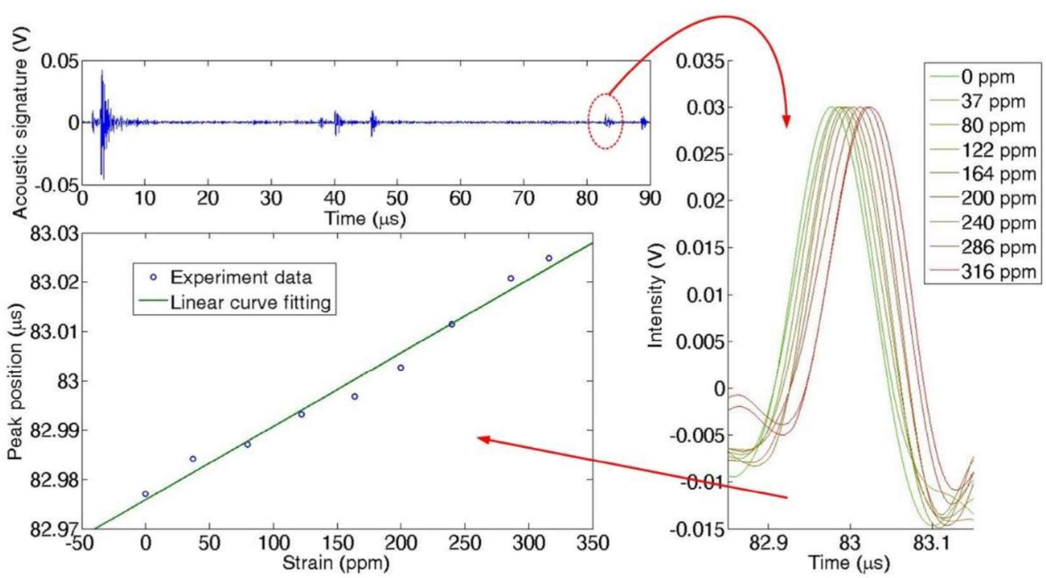

Figure 12-18 Strain test results

12.4.3 Crack test

In the crack test, we explored two methods. The first one is the industrial standard PLB test which only used the AGU portion of the FO-NDE element. In this test, the acoustic detection was set to be triggered by itself. A pencil lead was broken around 1 cm from the FO-NDE element and the recorded PLB signal is shown in Figure 12-19.

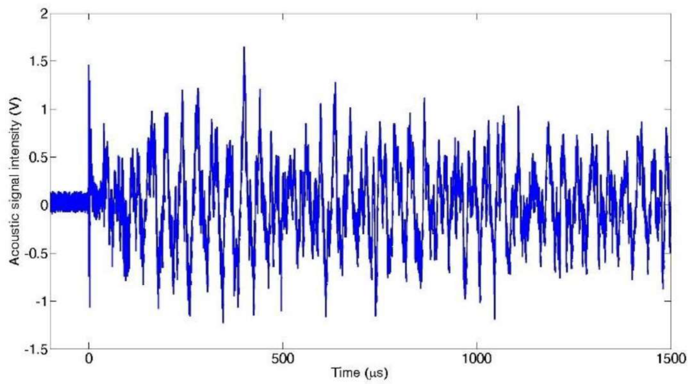

Figure 12-19 PLB signal

The second test was the active crack detection which used the whole FO-NDE element. A dremel tool with 0.5mm thickness was used to cut surface slits on the sample near the FO-NDE element. In this test, two cracks were cut and they were located on the two different sides of the FO-NDE element. One of them was parallel with the axial of the sample, the other one formed a 45 degree angle to the axial direction.

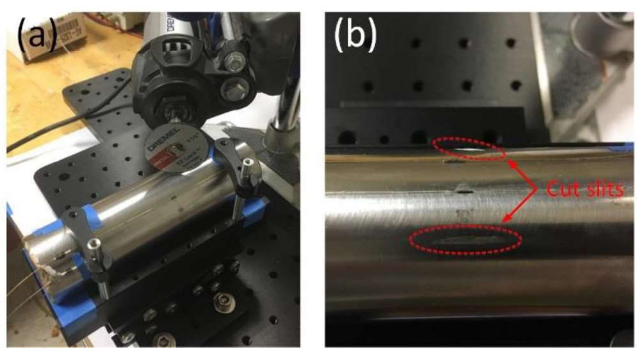

Figure 12-20 Crack simulation setup and cut sample

The test result is shown in Figure 12-21. By calculating the difference between the acoustic signatures before and after the slits cutting, we observed several new peaks. It should be noted that the peaks in the shaded area are not generated by the cracks. Instead, they are due to a slight temperature difference between these two sets of acoustic signatures.

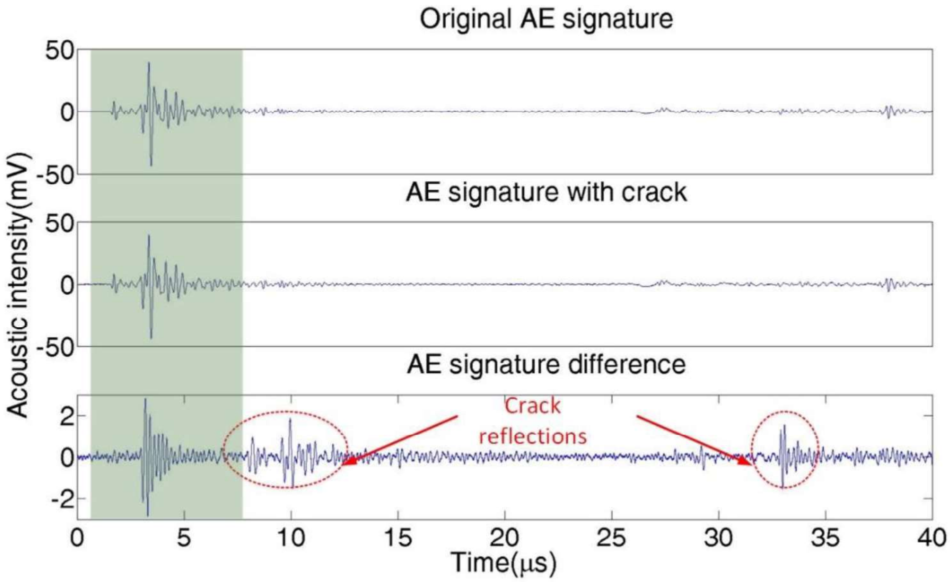

Figure 12-21 Crack test results

13 **Conclusions**

In this project, we have proposed and demonstrated a surface attached active fiber optic sensing network that can be used for structural health monitoring at high temperatures up to 600ºC. Several optical fiber based acoustic generation mechanisms were investigated and compared. The LIP based method has the highest photo-acoustic conversion efficiency, but is mechanically weak when it is used in a fiber optics structure and is not able to perform stably in a long term. The EDF based method is the most elegant design which uses only one fiber, but has the lowest photo-acoustic conversion efficiency thus is not a good choice for this project. The method we chose over the two is the scattering light based thermal expansion method, which has both good photo-acoustic conversion efficiency and long term stability. A complete bench-top sensing system based on this acoustic generation mechanism and the FBG acoustic detection was designed, built and tested. Both quantitative multi-parameter monitoring and system multiplexing were successfully demonstrated. Significant efforts were then devoted to applying this system on a P-91 pipe placed in a high temperature environment. The challenges mainly arise from the unwanted light leakage and the CTE mismatch between the fiber, the adhesive and the P-91 material. To eliminate the unwanted light leakage from the acoustic generation fiber, which often made the acoustic signature highly distorted, different types of metal coated fibers were tested. We finally chose the commercial grade gold coated fiber because it offers stable operation even at high temperatures beyond 600ºC. The CTE mismatch between the materials generated issues such as fiber breakage and FBG spectrum irregular distortion during the repeated temperature changes. To solve these issues, different types of high temperature adhesive were tested and we finally chose a Cotronics metallic based adhesive, which has relatively low CTE and low Young's modulus. In addition, we have changed the acoustic sensing mechanism from the standard FBG acoustic sensing to an FP-FBG acoustic detection, which avoids the physical contact between the FBGs and the adhesive. This provides a very stable and repeatable high temperature sensing performance. Finally, the implemented fiber optic, sensor system was demonstrated for the measurement of temperature, strain, cracks and corrosion. Based on our best knowledge, this demonstrated method is the first technology of a kind that permits multi-parameter measurement at temperatures up to 600 ^{o}C.

Reference:

1. P. Castello, V. Guttmann, N. Farr, and G. Smith, "Laboratory ‐ simulated fuel ‐ ash corrosion of superheater tubes in coal ‐ fired ultra ‐ supercritical ‐ boilers," Materials and Corrosion **51**, 786-790 (2000).
2. B. Chorpening, D. Tucker, and S. Maley, "Sensors applications in 21st century fossil-fuel based power generation," in *Sensors, 2004. Proceedings of IEEE*(IEEE, 2004), pp. 1153-1156.
3. S. M. Maley, and R. R. Romanosky, "Stakeholder Workshop. Advanced Process Control for Next Generation Power Plants. Summary Report," Internet Citation,[Online] Jul **1**, 78pp (2007).
4. V. Nagarkar, J. Gordon, S. Vasile, P. Gothoskar, and F. Hopkins, "High resolution X-ray sensor for non-destructive evaluation," IEEE Trans. Nucl. Sci. **43**, 1559-1563 (1996).
5. K. R. Leonard, E. V. Malyarenko, and M. K. Hinders, "Ultrasonic Lamb wave tomography," Inverse problems **18**, 1795 (2002).
6. H. Yan, H. Ning, Y. Kan, P. Wang, and M. J. Reece, "Piezoelectric Ceramics with Super ‐ High Curie Points," J. Am. Ceram. Soc. **92**, 2270-2275 (2009).
7. D. Van den Ende, W. Groen, and S. Van der Zwaag, "Development of temperature stable charge based piezoelectric composite quasi-static pressure sensors," Sensors and Actuators A: Physical **163**, 25-31 (2010).
8. R. Turner, P. A. Fuierer, R. Newnham, and T. Shrout, "Materials for high temperature acoustic and vibration sensors: a review," Applied acoustics **41**, 299-324 (1994).
9. H. Ning, H. Yan, and M. J. Reece, "Piezoelectric Strontium Niobate and Calcium Niobate Ceramics with Super ‐ High Curie Points," J. Am. Ceram. Soc. **93**, 1409-1413 (2010).
10. D. Dillon, R. Panesar, R. Wall, R. Allam, V. White, J. Gibbins, and M. Haines, "Oxy-combustion processes for CO2 capture from advanced supercritical PF and NGCC power plant," in *7 th International Conference on Greenhouse Gas Technologies, Vancouver, Canada*(2004).
11. Y. Yanzhi, X. Haichuan, L. Junxian, C. Duoggang, D. Gongjun, S. Bo, and L. Sheng, "600 MW Supercritical Boiler's Main Steam Temperature Control Analysis," in *Information Engineering (ICIE), 2010 WASE International Conference on*(IEEE, 2010), pp. 301-304.
12. W. P. Mason, *Physical Acoustics. Principles and methods. vol. 1, part A.* (Elsevier Science, 1964).
13. B. A. Auld, *Acoustic fields and waves in solids* (RE Krieger, 1990).
14. T. N. Bittencourt, P. A. Wawrzynek, A. R. Ingraffea, and J. L. Sousa, "Quasi-automatic simulation of crack propagation for 2D LEFM problems," Engineering Fracture Mechanics **55**, 321-334 (1996).
15. Z. Kala, "Sensitivity analysis of fatigue behaviour of steel structure under in-plane bending," Nonlinear Anal. Model. Control **11**, 33-45 (2006).
16. R. L. Roderick, and R. Truell, "The Measurement of Ultrasonic Attenuation in Solids by the Pulse Technique and Some Results in Steel," J. Appl. Phys. **23**, 267-279 (1952).
17. E. P. Papadakis, "Ultrasonic Attenuation and Velocity in Three Transformation Products in Steel," J. Appl. Phys. **35**, 1474-1482 (1964).
18. A.-D. ANCAS, "Theoretical Models in the Study of Temperature Effect on Steel Mechanical Properties."
19. C. EN, "1-2, Eurocode 3: design of steel structures, part 1.2: general rules—structural fire design," London: British Standards Institution (2005).
20. J. Skaar, "Modelling fiber bragg gratings," Cours de Institutt for elektronikk og telekommunikasjon (2008).
21. A. C. Tam, "Applications of photoacoustic sensing techniques," Rev. Mod. Phys. **58**, 381-431 (1986).
22. V. Teslenko, "Investigation of photoacoustic and photohydrodynamic parameters of laser breakdown in liquids," Soviet Journal of Quantum Electronics **7**, 981 (1977).

23. X. Wu, Z. Duan, H. Song, Y. Wei, X. Wang, and C. Huang, "Shock pressure induced by glass-confined laser shock peening: Experiments, modeling and simulation," J. Appl. Phys. **110**, 053112-053112-053117 (2011).
24. D. Devaux, R. Fabbro, L. Tollier, and E. Bartnicki, "Generation of shock waves by laser-induced plasma in confined geometry," J. Appl. Phys. **74**, 2268-2273 (1993).
25. F. Anabitarte, A. Cobo, and J. M. Lopez-Higuera, "Laser-induced breakdown spectroscopy: fundamentals, applications, and challenges," ISRN Spectroscopy **2012** (2012).
26. M. D. Feit, and J. J. A. Fleck, "Light propagation in graded-index optical fibers," Appl. Opt. **17**, 3990-3998 (1978).
27. W. Emkey, and C. Jack, "Analysis and evaluation of graded-index fiber lenses," Lightwave Technology, Journal of **5**, 1156-1164 (1987).
28. P. M. Becker, A. A. Olsson, and J. R. Simpson, *Erbium-doped fiber amplifiers: fundamentals and technology* (Academic press, 1999).
29. I. Pal, S. Sanghi, A. Agarwal, and M. Aggarwal, "Spectroscopic and structural investigations of Er< sup> 3+</sup> doped zinc bismuth borate glasses," Materials Chemistry and Physics **133**, 151-158 (2012).
30. C. R. Giles, and E. Desurvire, "Modeling erbium-doped fiber amplifiers," Lightwave Technology, Journal of **9**, 271-283 (1991).
31. E. Desurvire, and J. R. Simpson, "Amplification of spontaneous emission in erbium-doped single-mode fibers," Lightwave Technology, Journal of **7**, 835-845 (1989).
32. S. J. Mihailov, D. Grobnic, C. W. Smelser, P. Lu, R. B. Walker, and H. Ding, "Induced Bragg Gratings in Optical Fibers and Waveguides Using an Ultrafast Infrared Laser and a Phase Mask," Laser Chemistry **2008**, 1-20 (2008).
33. D. Grobnic, C. W. Smelser, S. J. Mihailov, and R. B. Walker, "Long-term thermal stability tests at 1000 °C of silica fibre Bragg gratings made with ultrafast laser radiation," Measurement Science and Technology **17**, 1009 (2006).
34. A. D. McKie, J. W. Wagner, J. B. Spicer, and J. B. Deaton, "Dual-beam interferometer for the accurate determination of surface-wave velocity," Appl. Opt. **30**, 4034-4039 (1991).
35. G. Wild, and S. Hinckley, "Acousto-ultrasonic optical fiber sensors: Overview and state-of-the-art," IEEE Sens. J. **8**, 1184-1193 (2008).
36. K. Vedam, "The elastic and photoelastic constants of fused quartz," Phys. Rev. **78**, 472-473 (1950).
37. S.-C. Her, and C.-Y. Huang, "The effects of adhesive and bonding length on the strain transfer of optical fiber sensors," Appl. Sci. **6**, 13 (2016).
38. M. Weik, *Fiber optics standard dictionary* (Springer Science & Business Media, 2012).
39. M. V. Brook, *Ultrasonic Inspection Technology Development and Search Unit Design: Examples of Pratical Applications* (John Wiley & Sons, 2012).